The effect of density on the near field of a naturally occurring oscillating jet

Grant England

Ph.D. thesis

30th June 2009

Turbulence, Energy and Combustion Group
School of Mechanical Engineering
Faculty of Engineering, Mathematical and Computer Science
The University of Adelaide, Australia

Preface

This document is the culmination of many years of study, and is the thesis submitted for the award of Doctoral of Philosophy. The topic of research is the effect that the density ratio has on the near field flow emitted from a nozzle that produces a naturally occurring oscillation. The nozzle investigated know as the Triangular Oscillating Jet (TOJ) is derived from the Fluidic Precessing Jet (FPJ). The FPJ nozzle has shown significant combustion benefits, namely reduced emissions and improved efficiency, when used in cement and lime kilns, particularly with gaseous fuels. Work on the TOJ is helping to extend the same benefits to solid fuel situations. With global climate change increasingly at the forefront of every ones mind it is important to continue to develop highly efficient, low polluting combustion systems. The work presented in this thesis uses a lab scale nozzle under cold flow conditions to examine the effect of varying density ratio, simulating different kiln air temperatures. The intention of this work is to further the understanding of the flow from the TOJ nozzle leading to improved design for combustion systems.

Declarations

This work contains no material which has been accepted for the award of any other degree or diploma in any university or other tertiary institution and, to the best of my knowledge and belief, contains no material previously published or written by another person, except where due reference has been made in the text.

I give consent to this copy of my thesis when deposited in the University Library, being made available for loan and photocopying, subject to the provisions of the Copyright Act 1968.

Grant England

Acknowledgements

It is not possible to personally acknowledge the contribution of everyone who has in some way helped me to complete this thesis. However there are some who I feel it would be remiss not to mention here due to their assistance with both my research and professional growth. Therefore a big thankyou goes to my supervisors A/Prof. Gus Nathan, Dr Peter Kalt and A/Prof. Richard Kelso who always made time to discuss any issues that I may have had.

I would also like to thank all the postgrads who over the time have helped me. In particular special thanks goes to Mike Brauer, Adam Langman, Paul Medwell, Eyad Hassan, Cris Birzer and Mike Riese who all helped not only with work related problems, but with keeping me sane via off topic conversations and mutual frustration venting sessions.

It is also important to mention the departmental support staff, whether it be the ladies in the office or the guys in the workshops, prompt assistance was always given when requested and is greatly appreciated.

Finally I would like to thank my family who provided me with the much needed moral support to continue the hard slog at times when I found the going tough.

Abstract

A major component of the world's ever increasing energy demand is supplied by combustion. Despite concerns of the enhanced greenhouse effect, primarily due to the emission of CO_2, fossil fuels will remain a major energy source for the foreseeable future. One approach to help to combat the enhanced greenhouse effects of combustion is to design highly efficient burners that achieve low levels of pollution. The fluidic precessing jet (FPJ) and the related triangular oscillating jet (TOJ) burners have shown such benefits when used in the cement and lime industry. As a result, they have been studied at the University of Adelaide for many years. Despite these investigations there are still significant gaps in the understanding of how they work. Addressing these gaps will allow their design to be improved. This work focuses on improving the understanding of the TOJ, and also provides insight into the understanding of the FPJ.

The benefits that can be provided by the FPJ and TOJ nozzles include fuel savings of up to 10% and NO_x reduction between 40-70%. This is due to the flows they produce. These flows are unsteady, creating large scale unique eddies that alter the mixing of the fuel and air, and hence the combustion. Many nozzle parameters, such as the nozzle expansion ratio and chamber length to diameter ratio, influence the nature of these unsteady flows. The influence of such parameters is well understood when the density ratio between the nozzle fluid and the ambient is unity. However, no previous investigations of the effect of density ratio on FPJ or TOJ flows have been performed. Density ratio has been previously shown to alter mixing in simple jets, and will therefore also affect the mixing of an unsteady flow. Therefore an understanding of how the jet-to-ambient fluid density ratio affects the flow from the TOJ is required to further our knowledge and improve its design.

To gain an understanding of the effects of density ratio, the TOJ nozzle has been investigated under cold flow conditions over a broad range of density ratios. Particle image velocimetry (PIV) and oscillation frequency data have been collected to assess any density ratio effects on the near field of the flow emerging from the TOJ nozzle. Along with the oscillation frequency, key flow parameters measured were the mean jet spread, the mean jet decay and the instantaneous jet deflection

angle.

The role of density ratio (jet fluid/ambient fluid), and its relative influence is assessed with the nozzle chamber length fixed. The effect of density ratio is also investigated with the chamber length as a variable and in a more industrially relevant configuration, in which a co-annular flow surrounds the TOJ flow.

Although the sensitivity to density ratio is less significant when the density ratio is greater than unity, it was found that increasing the density ratio leads to an increase in the mean spread, decay rate and the instantaneous jet deflection angle, and a decrease in the frequency of oscillation. At any given density ratio, increasing the nozzle chamber length within the investigated range resulted in an increase in the mean spread, decay rate and instantaneous jet deflection angle as well as an increase in the frequency of oscillation. While no measurements of the flow were taken within the nozzle chamber, frequency measurements suggest a decrease in the density ratio is analogous to an increase in the chamber length with respect to the influence on the internal flow.

The results from this study shed new light on the flow in the near field region of the TOJ nozzle. The knowledge gained will allow future designs for industrial use to be better tailored to use in rotary kilns, and contribute to improved efficiency and reduced emissions.

Contents

List of Figures

List of Tables

Notation

Latin

d_0	Nozzle diameter [m]
d_2	Exit lip diameter [m]
d_{e1}	Orifice equivalent diameter [m]
d_p	Particle diameter [m]
D	Chamber diameter [m]
D_j	Jet diameter [m]
f	Frequency response of particles [Hz]
f_{osc}	Frequency of oscillation [Hz]
FPJ	Fluidic precessing jet
Fr	Froude number
g	Acceleration due to gravity [ms^{-2}]
L	Chamber length [m]
M	Momentum [kgms^{-1}]
PIV	Particle image velocimetry
r	Radial distance [m]
$r_{1/2}$	Half width [m]
$\bar{r_{1/2}}$	Mean half width [m]
Re	Reynold's number
S	Density ratio between the jet and ambient
Sk	Stokes number
St_{osc}	Strouhal number of oscillation
TOJ	Triangular oscillating jet
u	Axial velocity [ms^{-1}]
$\bar{U_1}$	Bulk mean velocity [ms^{-1}]
U_c	Mean centreline velocity [ms^{-1}]
x	Axial distance [m]

Greek

Δ	Difference
λ	Wavelength [nm]
ρ	Density [kgm^{-3}]
μ	Dynamic viscosity [kgm^{-1}s^{-1}]
ν	Kinematic viscosity [m^{2}s^{-1}]
σ	Particle to fluid density ratio
θ	Instantaneous jet deflection angle [$^{\circ}$]
τ_p	Particle aerodynamic response time
τ_r	Representative flow time scale

Subscripts

a	Ambient
$c-a$	Co-annular flow
j	Jet
TOJ	Triangular oscillating flow
x	Axial
ϕ	Angular

Chapter 1

Introduction

Combustion is widely used in industry, for applications such as power and steam generation, as a thermal energy source for drying product and as a method of heating materials/products to a suitable reaction temperature. Industrial combustion primarily uses fossil fuels which are a finite resource. Fossil fuels can be used to generate flames for a wide range of industrial purposes, such as those described above, with heat transfer characteristics that are favorable to the application (Fulkerson et al, 1990). This, and the fact that fossil fuels are relatively cheap, means that they will continue to be an important source of industrial energy until competitive alternatives can be found. In fact, in 2004-05 95% of Australia's energy was provided by fossil fuels (41% coal, 34% oil and 20% gas) with the rest coming from renewables, and it is predicted that by 2030 the energy breakdown will be 94% from fossil fuels (36% coal, 33% oil and 25% gas) and 6% from renewables (Cuevas-Cubria and Riwoe, 2006). Projections of the Intergovernmental Panel on Climate Change (IPCC) also predict that fossil fuels will maintain their dominant position in the global energy mix to 2030 and beyond (IPCC, 2007).

The combustion of fuels has many advantages over other sources of energy. However the production of gaseous emissions, that adversely affect the environment, also occurs as a consequence of this combustion. In fact Prathner and Logan (1994) conclude that combustion is responsible for most of the enhanced greenhouse forcing to date. Some of the gases that cause the enhanced greenhouse

effect are oxides of nitrogen (NO_x), oxides of sulphur (SO_x) and carbon dioxide. NO_x and SO_x are also significant air pollutants which lead to photochemical smog, acid rain and the destruction of the ozone layer (Bowman, 1992). Bowman (1992) concludes that anthropogenic NO_x contributes 25-30% of the acidity of rain. The combustion of fossil fuels, especially coal, accounts for more than 80% of the SO_x and most of the NO_x injected into the atmosphere by human activity (Fulkerson et al, 1990). Therefore, government authorities are increasingly placing limits on the amount of these gases that may be released into the atmosphere each year. As a consequence, industry is driving the need for research into the area of reducing emissions from the combustion of fossil fuels. Research is also required to improve combustion efficiency so that industries can reduce their fuel costs and reduce carbon dioxide emissions, which are now coming under greater scrutiny as governments are beginning to introduce carbon credit/penalty schemes.

The scale and geometric design is different for each industrial plant where combustion is used, and therefore the design of a burner to produce optimal flame performance will be different for each case. The emissions from a flame are integrally related to the furnace or kiln in which it is confined and the process it serves (Nathan and Manias, 1995). Therefore, burner design is critical and must be tailored to each application. The primary focus of this research is on burners for use in the cement industry. The majority of cement kilns ($\sim$ 90%) operate on pulverised fuel, predominantly coal (Manias and Nathan, 1993; Megalos et al, 2001; Smart and Van de Kamp, 1999) and therefore designs of efficient, low emission burners that operate on coal are highly sought after.

While cement kilns account for less than 2% of the worlds energy consumption, their contribution to atmospheric pollution in the form of dust, CO_2 and NO_x is significantly higher than this (Mullinger, 1994). Bowman (1992) and McQueen et al (1995) show that, due to the detrimental effects of NO_x, it's reduction is a high priority. Techniques used to control emissions are broken into two categories; combustion modification and post combustion clean up (Bowman, 1992). Post combustion clean up is expensive (McQueen et al, 1995). Therefore combustion modification via improved burner design is an area of high interest.

Modification to the burner near field aerodynamics can have a great impact on

the production of NO_x (Mullinger, 1994). However it can result in the undesired side effect of increased emissions of carbon monoxide and unburnt hydrocarbons, reduced product quality and reduced refractory life (Mullinger, 1994; McQueen et al, 1995). The fluidic precessing jet (FPJ) burner is a burner that significantly alters the mixing in the near field region of the burner via the precession of the jet about its axis. This burner, when firing natural gas, has had great success in reducing NO_x emissions ($\sim$ 50%) while improving product quality (Manias and Nathan, 1993). With 90% of the world's kilns operating on pulverised fuels, work has also been carried out to develop systems suitable for firing solid fuels. Results from the pulverised fuel FPJ have shown promising results (Nathan and Hill, 2002). The main drawback for the FPJ firing pulverised fuels is the high pressure loss in the nozzle chamber required to generate the jet precession.

Due to a high pressure loss being undesirable, a low pressure drop version of the nozzle has been designed. This thesis investigates the flow in the near field of this low pressure drop burner, known as the triangular oscillating jet (TOJ) burner. The aim of the work is to further the understanding of the flow in the near field region of the burner with a view to contributing to the capacity to optimise the burner for efficient use in cement kilns with reduced emissions of NO_x. Rotary kilns are discussed further in chapter 2. However it is important to note here that they operate over a broad range of secondary air temperatures, and hence burner fluid to secondary air density ratios. This work therefore focuses on improving the understanding of the flow from the TOJ under variable density conditions.

The remainder of the thesis is structured as follows. Chapter 2 outlines some of the technical background relevant to this study. Chapter 3 details the experimental techniques, experimental setup and data analysis methods used to conduct the study. Chapters 4, 5, 6 and 7 present the experimental results and discuss the findings. Chapter 8 ties the work together with the study's conclusions.

Chapter 2

Background

2.1 Rotary Kilns

Rotary kilns are widely employed in the minerals and materials industry to convert raw materials into useful product materials (Boateng, 2008), although they often only conduct one part of the overall process. Processes commonly carried out in rotary kilns are the production of cement and lime, reduction of oxide ore (eg. alumina, nickel and zinc), calcination of petroleum coke and hazardous waste reclamation. In most applications the objective is to drive specific reactions in the materials, which, for either kinetic or thermodynamic reasons, often require the materials to reach high temperatures (Boateng, 2008). For example material temperatures in a cement kiln may approach 2000K, with this high material temperature then driving the chemical reactions that transform the raw materials into product. High radiant heat transfer rates, and hence high flame temperatures are necessary to ensure high material temperatures are reached. The use of rotary kilns is a relatively efficient means to achieve high radiant heat transfer in a continuous process, and are therefore an effective way of processing said materials. However the high flame temperatures typically lead to significant NO_x production via the thermal NO_x mechanism, an issue which is discussed more in section 2.2.1.

Figure 2.1 shows a schematic diagram of a typical rotary kiln as used for cement production. Kilns typically have lengths ranging from 30 to 230m and diameters

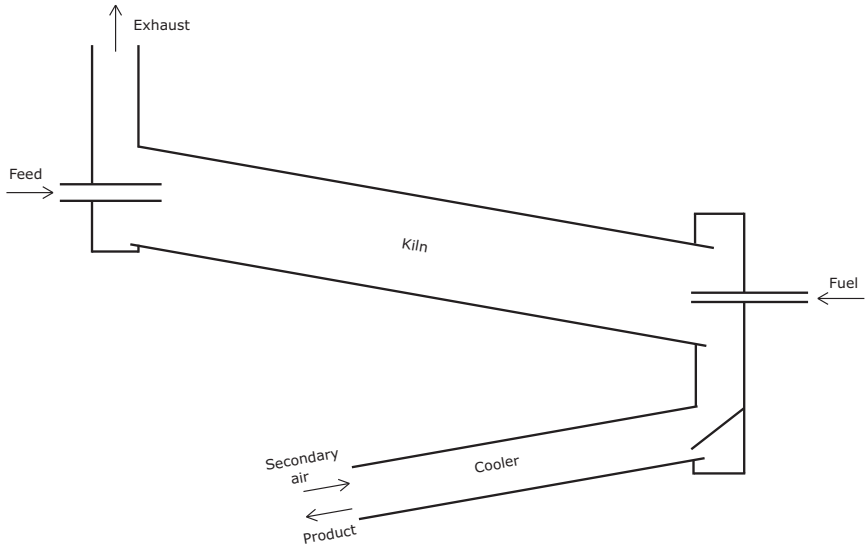

Figure 2.1: Schematic diagram of a rotary kiln.

ranging from 2 to 8m. The kiln itself is set at a slight angle ($\sim 2°$) so that the feed will move along its length as the kiln rotates. Typical rotation rates are of the order of one revolution per minute.

Fundamentally a rotary kiln is a heat exchanger in which energy from a hot gas phase is extracted by the bed material (Boateng, 2008). Most commonly kilns are run counter-current. As such the fuel and primary combustion air is introduced via the burner at the lower end of the kiln, which is the opposite to that where the feed is introduced. Therefore as the feed, which forms the bed material, passes along the length of the kiln it is heated by the hot gases from the flame that are moving in the opposite direction. Along the length of the kiln the bed material undergoes various heat exchange processes, which may include drying, heating and chemical reactions covering a broad range of temperatures (Boateng, 2008). More than one chemical reaction may take place within the kiln. For example in cement production the bed first undergoes a calcination reaction which is followed by a clinkering reaction. At the lower end of the kiln the bed material, now product, falls out of the kiln into a cooler.

The cooler has two purposes that are achieved simultaneously. They are to rapidly cool the product and to preheat the secondary combustion air. Depending on design, efficiency and throughput the temperature to which the secondary combustion air is preheated can be anywhere from 400 to 1200°C. Consequently the density of this air will range from 0.52 to 0.24 kgm^3. The ratio between the density of the fluid entering via the burner and the secondary air will influence the mixing patterns, and therefore the flame. As such, an understanding of how this density ratio affects the mixing is important for efficient burner design.

2.2 Emission Control

Increasing CO_2 and other greenhouse gas concentrations in the earth's atmosphere are enhancing the natural greenhouse effect, leading to climate change (Davison et al, 2001). Therefore it is generally accepted that limits need to be placed on the amounts of such gases that may be emitted into the atmosphere. To drive effective technology development, innovation and deployment to aid in emission reduction, government support is required via financial contributions, tax credits, standard setting and market creation (IPCC, 2007). Increasingly government policies are driving such approaches. Therefore there is increased pressure on industry and increased incentives for industry to reduce their emissions. As a result much work is being done to develop methods of emission control. The focus of this work is to reduce emissions of NO_x and CO_2 in the cement industry. These are discussed separately in sections 2.2.1 and 2.2.2.

2.2.1 NO_x

The methods that can be employed for NO_x control are combustion modifications and post combustion clean up (McQueen et al, 1995; Bowman, 1992). However before these are discussed it is necessary to describe NO_x and the mechanisms of its formation. Nitrogen oxides, commonly referred to as NO_x, consist primarily of NO and NO_2. Oxides of nitrogen are an important pollutant as they can be formed even with the combustion of "clean gases". This is since formation can occur anywhere nitrogen and oxygen exist together at high temperature (Wünning

and Wünning, 1997).

The investigation of nitric oxide (NO) is one of the top priorities in combustion research, since this is the most prevalent form of NO_x around the combustion region. However away from the combustion zone, the NO can lead to the formation of nitrogen dioxide, NO_2. Nitric oxide, NO, may be formed by three main mechanisms;

- Thermal (or Zeldovich) mechanism — dominates, especially where high temperatures are present
- Prompt (or Fenimore) mechanism — important in fuel rich environments
- Fuel bound mechanism — results from oxidation of nitrogen containing compounds in the fuel

The rate of formation of NO is highly dependent on temperature, time and stoichiometry (Borman and Ragland, 1998). For thermal NO_x formation, the reactants only need to remain at 1600°C for a few seconds and above 2000°C for a few milliseconds (Wünning and Wünning, 1997).

2.2.1.1 Combustion Modification

Combustion processes can be modified in a number of ways. The main ways that lead to reduced NO_x are burner operation, burner design and the staging of combustion fuel and/or air. Owing to the high flame temperatures ($\sim$ 2000°C) inside a cement kiln the dominant mechanism for NO_x production is the thermal NO_x route (Mullinger, 1994; Deussner, 1995). Emissions of NO_x are strongly dependent on the operation of the burner due to the dependence of NO_x production on the local flame temperature and oxygen availability (Mullinger, 1994). Techniques to reduce NO_x try to cut peak temperatures, keep the residence time at high temperatures low and avoid high O_2 concentration in these areas (Wünning and Wünning, 1997).

Reduction of the temperature in the combustion zone leads to reduced NO_x if all other conditions are unchanged (Bauer, 1990; Bowman, 1992). This can be

achieved by operating the burner in a manner that results in "poorer" fuel/air mixing meaning the combustion is initially fuel rich. However, while this results in reduced NO_x, there can be significant negative side effects of doing this, including increased emissions of CO and hydrocarbons due to incomplete combustion, reduced product quality due to inadequate heat flux and flame impingement on the refractory causing product loss and reduced refractory life (Mullinger, 1994; McQueen et al, 1995).

Staging of the combustion air can be effectively used to reduce the emissions of NO_x (Bowman, 1992) as it generates a reducing atmosphere which tends to destroy NO_x (Dusome, 1995). Staged combustion is essentially the gradual oxidation of fuel due to a local deficiency of combustion air (Dusome, 1995). It works by operating the primary combustion zone with an overall rich fuel/air ratio. By operating fuel rich there is less oxygen present to react with nitrogen and a reducing atmosphere is generated. The remaining air required for complete combustion is then injected downstream. Staging in multi-burner furnaces such as a boiler can be applied quite simply by operating the lower burners fuel rich and introducing burnout air higher up in the furnace. However staging of the combustion air in a rotary kiln is impractical as it requires the use of air lances (Nathan and Luxton, 1991). Similarly flue gas recirculation can be used as a means to reduce NO_x (Nathan et al, 1992) as this also creates a fuel rich combustion zone. However, it is also impractical for application to a cement kiln.

As seen with air staging, modifying combustion in the primary combustion zone can lead to reductions in NO_x. In modification of the primary combustion zone the near field aerodynamics of the flame are of high importance as this determines the oxygen concentration in the primary combustion zone (Mullinger, 1994). The aerodynamics are determined by both the burner design and operation. Therefore burner design is a crucial factor in reducing NO_x emissions. Fine scale mixing leads to increased local temperatures. Nathan et al (1993) have shown that by modifying the turbulence with jet precession, fine scale mixing can be suppressed and large scale mixing enhanced. With enhanced large scale mixing much of the combustion is deduced to occur under local fuel rich conditions (Nathan and Manias, 1995). This leads to increased global residence times, lower flame temperatures and increased radiant heat fraction with an overall result of a reduction

in NO_x (Nathan et al, 1993, 1996). However, since the emissions from a flame are integrally related to the furnace or kiln in which it is confined, and to the process it serves, the greatest reduction in NO_x is likely to occur by simultaneously optimising the heat release profile to suit the process requirements (Nathan and Manias, 1995).

2.2.1.2 Post Combustion Clean Up

Post combustion clean up can be by either catalytic or non-catalytic methods (Dusome, 1995). Catalytic methods require the use of purpose built scrubbers, which are used to remove emissions by means of chemical reactions. Such methods are expensive and often require frequent replacement of the scrubbers (McQueen et al, 1995). Non-catalytic methods involve creating a reducing atmosphere at the exit of the kiln which acts to destroy NO_x (Dusome, 1995). This is a technique which can be applied to more modern plants which run a pre-calciner which is operated fuel rich, creating the desired reducing atmosphere. It can be argued that this is a combustion modification method of NO_x reduction since the reducing atmosphere is created via a fuel rich flame. However considering the pre-calciner to be a separate unit process from the kiln, this is a post combustion clean up method for the NO_x created in the kiln. While this can effectively reduce NO_x emissions in plants with pre-calciners, further advantage can be gained by reducing the amount of NO_x that exits the kiln via combustion modification. Therefore, to reduce the emissions of NO_x from the cement industry, attention must be directed to improvements in burner technology and operation.

2.2.2 CO_2

Fossil fuels are carbon based. Therefore carbon dioxide will always be a product of fossil fuel combustion. Due to the significant contribution CO_2 plays in enhancing the greenhouse effect, it is important to reduce CO_2 emissions. The main ways that CO_2 levels can be reduced are to:

- Reduce energy consumption

- Improve process efficiency
- Use lower carbon fuels - eg. natural gas
- Enhance sinks eg. forrests
- Switch to renewable or nuclear energy sources
- Use biomass or waste fuels
- Capture and storage of CO_2 emissions

The extent to which these techniques can reduce CO_2 depends on many factors including emission reduction targets, costs, availability of alternate energy sources and social factors (Davison et al, 2001). As an example, switching to renewable or nuclear energy sources is not suitable for all energy applications as well as the social stigma associated with nuclear energy.

The use of alternate fuels such as biomass and waste fuels (eg. shredded tyres) reduces the reliance on fossil fuels. While the use of such fuels still results in CO_2 emissions, the use of such fuels is largely considered to be carbon neutral. This is because, in the case of biomass, carbon from the atmosphere is fixed into the biomass as it is grown. Therefore the same carbon is released back to the atmosphere when it is burnt to produce energy. Of course there is an extra carbon cost associated with the energy required to harvest and shred the biomass into a form that can easily be used in an industrial combustor. While the use of such fuels may reduce the amount of "new" CO_2 released to the atmosphere other compounds found within these fuels can also lead to increases in other undesirable pollutants.

Much work is being done on post combustion capture and storage due to its potential. With air used as the oxidant, 80% of the flue gas is nitrogen. To capture and store this along with the CO_2 is unnecessary and would significantly increase the costs. Therefore CO_2 in the exhaust must be separated from the other gases. Amine based solvents are effective at stripping CO_2 from the exhaust. However, the regeneration of the solvents which, simultaneously separates the CO_2 for storage and prepares the solvents for re-use, requires a large energy cost which can be up to 80% of the total process energy (Wall, 2006). There is also

the additional cost of compressing and transporting the CO_2 to a suitable storage location. These significant costs are a major detractor for the implementation of carbon capture and storage.

While capture reduces the amount of CO_2 released to the atmosphere it should be considered as a secondary step to other CO_2 reduction methods, in particular reducing energy consumption and improving process efficiency. Therefore, as is also the case for NO_x reduction, to reduce CO_2 emissions, even if only moderate reductions are achieved, attention must be directed towards improving burner technology and operation, specifically efficiency.

2.3 Two Phase Flows

With approximately 90% of the world's cement kilns operating on solid fuels (Manias and Nathan, 1993; Megalos et al, 2001; Smart and Van de Kamp, 1999) it is vitally important to design burners that will operate effectively on such fuels. Transportation of fuel to the furnace is done by conveying the fuel, in particulate form, to the furnace in a fluid. Therefore the fuel/air mixture forms a two phase flow. Flow dynamics and particle dispersion is typically controlled by large scale coherent structures (Aggarwal, 1994). In two phase flows it has been shown that the gas phase disperses much more rapidly than the particles, and that particle dispersion decreases with increasing particle size (Fan et al, 1996a). Also particle dispersion is governed by convection due to large scale turbulence structures and not diffusion (Longmire and Eaton, 1992). As such a method of describing how a particle will be influenced by the fluid flow is defined by its Stokes number. The Stokes number is defined as $Sk \equiv \frac{\tau_p}{\tau_f}$ where τ_p is the particle aerodynamic response time and τ_f is some representative time scale in the flow (Fessler et al, 1994). Stokes number and particle loading ratio are the basic parameters that govern two phase flows (Di Giancinto et al, 1982).

Particles with small Stokes numbers simply follow the flow as tracers, so, if the fluid is well mixed by turbulence the particles should also be distributed uniformly throughout the flow. Large Stokes number particles do not have sufficient response time to respond to fluctuations in the fluid velocity and therefore simply

pass unaffected through any turbulence structure (ie. vortex or eddy). Particles with a Stokes number of the order one will respond somewhat to the turbulent motions but cannot follow tightly curved streamlines, therefore the instantaneous concentration field may be modified in the vicinity of turbulent eddies (Fessler et al, 1994; Eaton and Fessler, 1994). However the selection of a suitable flow time for the Stokes number is somewhat ambiguous because there are a wide range of scales of vortex motion in a flow (Aggarwal, 1994).

Large particles cannot follow the instantaneous fluid flow streamlines so an individual particle does not necessarily remain with a given fluid element (Eaton and Fessler, 1994; Fan et al, 1996a). Fan et al (1996a) and Fan et al (1990) showed that the mean particle size at the edge of the jet is 15-20% smaller than that at the jet centreline. This is due to the smaller particles being influenced by the flow more than the larger particles, so that the latter tend to concentrate on the jet centreline.

Increasing the amount of particles in the flow (loading ratio) typically acts to decrease the rate of dispersion of both the fluid and the particles (Fan et al, 1996a, 1990). This suggests that the turbulence intensity is reduced when particle loading is increased. Kulik et al (1994) showed that the turbulence intensity was attenuated by the addition of particles, but that the degree to which it was attenuated was increased, not only by the particle mass loading, but also by the particle Stokes number. They also showed that the turbulence intensity in the transverse direction was affected more than that in the streamwise direction, due primarily to the inability of the particles to respond well to the higher frequency turbulent fluctuations in the transverse direction. Higher particle loading also typically reduces the rate of decay of the fluid mean centreline velocity (Fan et al, 1996b).

Dilute particle laden flows with a Stokes number of order one show a phenomenon known as preferential concentration. This is effectively the accumulation of dense particles within specific regions of the instantaneous turbulence field (Eaton and Fessler, 1994). In such preferentially concentrated flows, the instantaneous concentration field is correlated with the turbulent motions. Eaton and Fessler (1994) have shown that the mechanisms that drive preferential concentration (clustering) are the centrifuging of particles away from vortex cores and the accumulation

of particles in convergence zones. Therefore, within the flow vortex cores are regions of low particle concentration while regions of high strain have high particle concentrations (Eaton and Fessler, 1994; Fessler et al, 1994). Local concentrations can be as high as 30 times the mean concentration. Fessler et al (1994) show that the spacing between clusters is more indicative of the size of the flow structures causing the cluster than the size of the cluster. By enhancing large scale turbulence at the expense of fine scale turbulence, clustering of particles can be enhanced (Nathan et al, 2000). A particle which is in a cluster may burn in a fuel rich environment even though the time averaged stoichiometry may be quite lean (Eaton and Fessler, 1994). As previously discussed in section 2.2.1.1 local fuel rich combustion leads to reduced emissions of NO_x. Nathan et al (2000) have shown that in cement kilns clustering not only reduces NO_x but can also reduce the flame ignition distance and improve the heat transfer profile.

As discussed clustering occurs when the Stokes number is of order one. The Stokes number as defined above is the ratio between the particle aerodynamic response time and a representative flow time scale. This means that changing either of these properties will result in a change in the Stokes number away from one and hence reducing the likelihood of particle clustering. Changing the nozzle to ambient fluid density ratio changes the resulting mixing. As a consequence of changed mixing one or both of the Stokes parameters will most likely be changed. This means that while clustering may be observed at certain secondary air temperatures, at other secondary air temperatures the formation of clusters may be reduced or non-existent. Therefore it is important to understand how a change in the nozzle to ambient fluid density ratio affects the flow and resulting mixing to ensure optimal burner design for use in two-phase burner systems.

2.4 Variable Density

The operation of a cement kiln is complex and is affected by the process design. Generally, product leaves the kiln and enters a cooler. Air is used to cool the product, which causes the air temperature to increase. The air used to cool the product is then drawn into the kiln as secondary air. However depending on the

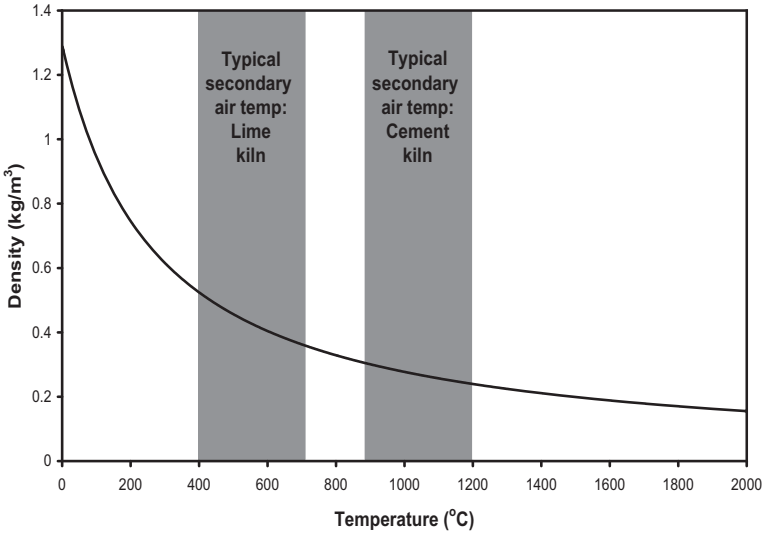

Figure 2.2: Density of air with respect to temperature.

cooler design and efficiency and the air throughput, the temperature of this air can vary significantly from kiln to kiln. Varying air temperature implies variations in density, and hence the ratio of the density of jet fluid to the surrounding fluid is also going to vary from kiln to kiln. Figure 2.2 shows how the density of air varies with temperature. The performance characteristics of a jet can be significantly altered by varying this density ratio.

The effect of density is most significant in the near field of the flow. This is because, in the far field, the ratio between the density of the jet and its surrounds approaches unity due to entrainment (Sautet and Stepowski, 1998; Richards and Pitts, 1993; Brown and Roshko, 1974). In addition the effects of buoyancy may be important in flows with non-unity density ratios (Pitts, 1991). The rate of buoyancy is typically determined by the Froude number, which is defined as $Fr = \frac{u_j^2 \rho_j}{\Delta \rho g D_j}$ where u_j is the jet velocity, ρ_j is the jet density, $\Delta\rho$ is the difference in density between the jet fluid and the surrounding fluid, g is the acceleration due to gravity and D_j is the initial jet diameter (Larson and Jonsson, 1995). However Sautet and Stepowski (1998) have shown that the effects of buoyancy are negligible up to a distance x_m defined by $x_m = Fr^{1/2} R_p^{1/4} d_0/2$ where Fr is the Froude number at injection, R_p is the density ratio of the jet fluid to the ambient fluid and d_0 is the jet nozzle diameter.

Many investigations have been carried out on simple jets with variable density ratios (Era and Saima, 1977; Sreenivasan et al, 1989; Richards and Pitts, 1993; Pietri et al, 1998; Stepowski and Sautet, 2003). Era and Saima (1977), Sreenivasan et al (1989) and Richards and Pitts (1993) all show that when the density ratio is smaller the rate of spread is increased. Pietri et al (1998) and Stepowski and Sautet (2003) show that axial decay is increased when the density ratio is lower. These findings are consistent and indicate that the initial density ratio is an important parameter.

2.5 Unsteady Mixing

In a non-premixed system, mixing of the fuel and air is a key step in the combustion process. Some mixture ratios, on ignition, may promote reactions that cause the formation of pollutants such as NO_x, whilst others will hinder such reactions. Mixture ratios that promote the formation of NO_x are highly undesirable. Non-steady effects can considerably modify the process of fuel and air mixing. Kato et al (1987) suggest that non-steady jet flows can be used to alter the fuel/air mixing such that the undesirable mixture ratios resulting from the nozzle would be minimised.

Unsteadiness in turbulent jet flows can be amplified or enhanced by mechanical, acoustical or fluidic excitation. The use of mechanical components can lead to increased maintenance costs particularly in dusty environments, and using acoustic components can lead to excessive noise, both of which are undesirable. This means that mechanical and acoustic excitation are not preferable for most industrial applications. Raman and Cornelius (1994) suggest that, for use in industry, an excitation device should have minimal power requirements, no moving parts and should produce excitation that is controllable in frequency, amplitude and phase.

Viets (1975) developed the Flip-Flop nozzle, as shown in figure 2.3, that provides a time-dependent flow at the nozzle exit and does no contain any mechanical or acoustic parts. The nozzle configuration requires a rectangular jet to be expanded through one (transverse) dimension. The fluid flow entering the expansion is bi-

Figure 2.3: Schematic diagram of the flip-flop nozzle (Raman and Cornelius, 1994).

stable and, due to the Coanda effect, attaches itself to one of the walls in the transverse direction. This attachment causes pressure waves to travel through a pipe which connects the two walls in the transverse direction. Pressure waves in the pipe create a so called feedback system between the walls which causes the flow to switch periodically between these two walls. Therefore a time dependent oscillation in the transverse direction is created at the nozzle exit (Viets, 1975). By making the expanded section of the nozzle divergent, the angle at which the flow is ejected into the surrounding fluid can be controlled. The combination of jet oscillation and the exit angle has been shown to increase significantly the initial rate of mixing between the jet fluid and the surrounding ambient fluid (Viets, 1975; Morris et al, 1992).

Since Viets, many researchers have investigated the flow properties of the flip-flop nozzle (Raman et al, 1993, 1994; Raman and Cornelius, 1994; Morris et al, 1992; Mi and Nathan, 2001). Of particular note here are the studies by Morris et al (1992) who introduced particles into the flow, and Mi and Nathan (2001) who managed to sustain oscillation without the interconnected control ports.

In the study by Morris et al (1992) a diverging section was used following the expansion. Increasing the angle of divergence was found to increase decay in the axial jet velocity and also to increase the transverse velocity due to the large jet deflection. With this decreased axial velocity and increased transverse velocity, it was shown that the particles seeded into the flow were dispersed widely by the nozzle. It was found that the particles seeded into the flow maintained higher axial velocities than the conveying air, even at large transverse displacements, due to their high inertia.

Mi and Nathan (2001), developed a variation of the flip-flop nozzle to generate the oscillation without the need for the external feedback system, as shown in figure 2.4. They found that oscillation could be generated by what they termed an internal feedback process that was triggered by natural instabilities created by specific geometric configurations. The nozzle configuration was such that the inlet jet protruded a length L_2 into the expansion chamber. The protrusion into the chamber creates a space over which a feedback system can be established, enabling communication between the upper and lower sides of the inlet jet. The length L_2 is a controlling parameter for jet oscillation. Creating large scale oscillations in jet flow without the need for a feedback pipe reduces the nozzle complexity and minimises possible blockage to such a pipe.

The flip-flop nozzle has been shown to be capable of creating large-scale oscillations that could significantly alter the mixing of combustion fuel and air. The rectangular geometry of the flip-flop nozzle is not suited to many industrial applications, particularly the cement industry, where axisymetric burners are preferred. Another nozzle has been developed to produce large-scale oscillations from a nozzle with a circular cross-section and is known as the fluidic precessing jet (FPJ).

Figure 2.4: Schematic of the modified flip-flop nozzle (Mi and Nathan, 2001).

2.6 Precessing Jet Nozzle

2.6.1 Cold Flow

2.6.1.1 Flow Characteristics

The fluidic precessing jet nozzle consists of a circular orifice through which fluid enters into an axisymmetric chamber that has a lip at the exit. Precession of the fluid at the nozzle exit is caused by a rotating pressure field within the nozzle rather than by acoustical or mechanical excitation. Figure 2.5 shows the FPJ nozzle and its flow in simplified form. As seen in figure 2.5 the jet enters the nozzle chamber from an orifice. Inside the chamber the jet reattaches asymmetrically to the chamber wall. The axial distance to the point of reattachment, when normalised by the step height, decreases with increasing expansion ratio (Nathan et al, 1998). The reattachment provides positive feedback since any azimuthal movement of the reattachment point will necessarily establish an azimuthal pressure field (Nathan et al, 1998). This induces a rotating effect causing the self sustaining low frequency precessing motion to occur. Near to the the exit region of the chamber a strong recirculation is observed (Hill et al, 1992). Also, surrounding fluid from outside the nozzle is continually drawn upstream and into the nozzle chamber through the exit (Nathan, 1988). Wong et al (2001) found that the speed of the reverse flow, which is the combination of recirculated fluid and induced ambient fluid, can be as high as 30% of the forward speed. This

Figure 2.5: Simplified flow from a fluidic precessing jet (Wong et al, 2002).

reverse flow generates a strong swirling motion at the upstream end of the nozzle chamber, opposite in direction to that of the precession.

On exiting the nozzle, the precessing jet is deflected across the nozzle axis (Hill et al, 1992). This results in the mean flow spreading more rapidly than a standard axial jet (Nathan et al, 1998), and hence the jet decay rate is also increased (Mi et al, 1998). The combination of the rapid spread and the precessional motion causes enhancement of the large scale mixing between the jet and its surroundings (Hill et al, 1992; Nathan et al, 1998; Mi et al, 1998). There is also a suppression of the fine scale mixing (Mi et al, 1998). Smith and Nathan (2001) showed that rapid spreading without the low frequency precession does not result in enhanced large scale mixing. They did this by comparing the flow from a simple deflected jet (corresponding to precession frequency = 0) and a conical jet (corresponding to precession frequency = ∞) both deflected at 45° to the nozzle axis. It was shown that only the FPJ flow increased the size of the large scale mixing. It is this enhancement of the large scale mixing that leads to the benefits that can be achieved by the FPJ nozzle in some applications (Newbold, 1998).

2.6.1.2 Precession Probability

It has been noted that the basic FPJ nozzle configuration shown in figure 2.5 results in a tendency to switch between two modes, these being the precessing flow mode and a largely axial flow mode (Hill et al, 1992, 1995). This switch,

when it occurs, is rapid and no intermediate state is apparent (Hill et al, 1992). Mode switching is undesirable since a change in the flow results in a change in the flame characteristics and hence system performance. In an extreme case, mode switching could cause a plant to become unstable. Therefore it is important to ensure that the nozzle operates in only one mode, the precessing mode.

Changes to the nozzle configuration can lead to increases in the regularity and reliability of precession. Hill et al (1995) showed that, by simply increasing the expansion ratio, the precessing flow mode becomes more probable. The nozzle inlet is circular in shape, but a similar result can be achieved using an orifice plate, a pipe or a smooth contraction. Wong et al (2002) showed that precession is most favoured when a sharp edged orifice plate is used at the nozzle inlet and least favoured when a smooth contraction was used at the nozzle inlet. This is deduced to be due to the asymmetric shedding of the initial boundary layer from the orifice plate. A suitable partial obstruction (centre-body) placed near to the exit of the nozzle also improves the probability of precession by forcing the jet to reattach to the chamber walls (Wong et al, 2001). However the cost of increasing the probability of precession by these methods is an increased pressure drop through the nozzle.

Jet precession can also be made more probable by changing the initial flow conditions. Introducing swirl upstream from the orifice stabilises the jet precession (Hill et al, 1992; Nathan, 1988). Hallet and Gunther (1984) and Dellenback et al (1988) showed that, by imparting swirl to the flow upstream from the inlet, precession can be achieved with an expansion ratio as small as two. Hallet and Gunther (1984) showed that precession is strongest and most regular at low rates of swirl. As the swirl number was increased, precession was found to become more irregular. Once the swirl intensity exceeds a critical value, the flow exhibits a break down in the precession. This is due to the internal jet spreading faster at higher swirl rates, and therefore filling the cross-section more quickly (Hallet and Gunther, 1984). Dellenback et al (1988) also showed that as the swirl intensity is increased, the point where the jet reattaches moves upstream. Therefore adding swirl, at low intensity, upstream from the inlet orifice increases the probability of precession.

2.6.2 Reacting Flow

2.6.2.1 Gaseous Combustion

The FPJ burner utilises a large expansion ratio to increase the probability of precession. Therefore a large pressure drop occurs through the nozzle. When natural gas is used as the fuel this is not usually a problem since gas is supplied to most industrial plants at high pressure. It has been shown that the FPJ firing natural gas can reduce NO_x emissions by up to 50% (Manias and Nathan, 1993). Fuel savings of up to 5% are also typically achieved. The flame produced by the FPJ is short and highly luminous (Manias and Nathan, 1993). This leads to a shift in the peak heat flux towards the burner (Parham et al, 2000). In a cement kiln this shift in heat flux is beneficial as a higher quality clinker is produced (Manias and Nathan, 1993). The benefits achieved are due to the flow patterns created by the nozzle. The flow from the nozzle reduces the global strain rate and increases the residence time in a flame (Newbold, 1998). The reduced strain rate and increased residence time leads to increased sooting within the flame. Higher levels of soot in the flame lead to an increase in the radiant fraction of heat transfer and a reduction in the flame temperature. By reducing the flame temperature the levels of NO_x are also reduced (Newbold, 1998; Newbold and Nathan, 1999).

2.6.2.2 Solid Fuel Combustion

Due to the high pressure drop the FPJ nozzle becomes less suitable when a solid fuel such as pulverised coal is to be used. If the pulverised fuel were to be introduced directly through the nozzle, the nozzle erosion/wear is expected to become a problem at the high velocities required to pneumatically convey the coal through the nozzle and achieve the desired pressure drop for precession to occur. Therefore it is preferable for the coal to be introduced via a co-flow at a much lower velocity. The flow through the FPJ is then a fluid containing no particles. The FPJ flow can still be a fuel such as natural gas, however other fluids such as air or steam may also be used. Since natural gas is not necessarily available and is often more expensive than coal, and steam is not usually available in cement

kilns, air becomes the logical choice for this fluid. However for the air flowing through the chamber to cause precession, it must be compressed significantly due to the associated high pressure drop through the nozzle. Compressing air to the levels required, which could be as high as 320 kPa (Nathan and Hill, 2002), would be expensive both due to the capital costs and ongoing operational costs of compressors.

Nathan and Hill (2002) conducted tests with such a configuration in a cement kiln and showed a 27% reduction in NO while achieving a fuel reduction of 4% when compared with a conventional high momentum jet burner. When using the FPJ there is also a reduction in the flame ignition distance, an increase in the peak heat flux and a translation of the heat flux profile towards the burner (Smith et al, 2002). Smith et al (1998a) showed a factor of three reduction in the ignition distance, which is caused by the precessing flow interacting with the surrounding annular flow and increasing the scale of the turbulent flow structures causing increased residence times in the pre-ignition region (Smith et al, 1998b). It is however noted that, for the reduction in ignition distance to occur, the fuel must contain sufficient volatile matter (Smith et al, 1998a). As seen in section 2.3 the effect of the larger scale turbulent structures on the fuel particles is to enhance the formation of particle clusters. These particle clusters are proposed to contribute to the reduced NO_x production by creating local instantaneous fuel rich combustion environments (Smith et al, 1998b). Smith et al (1998a) showed that the nozzle achieved the greatest reduction in NO_x when the air supplied through the FPJ nozzle was between 5 to 7% of the total air required for combustion.

2.7 Triangular Oscillating Jet

The high pressure drop through the FPJ is a significant drawback in its application to pulverised fuels. Therefore a low pressure drop alternative would provide substantial benefits. A variant of the precessing jet nozzle known as the triangular oscillating jet (TOJ) nozzle has been designed by changing the inlet orifice from circular to a triangle. This nozzle has also been shown to produce large scale oscillations in the emerging jet, but with a smaller expansion ratio and therefore

a lower pressure drop than is required for the FPJ (Lee et al, 2003). However the oscillation from this nozzle is significantly different from the precession produced by the circular orifice. One of these differences is that the oscillation is not azimuthally symmetrical but rather has three preferred azimuthal directions aligned with the corners of the triangular orifice (Lee et al, 2003). This is due to the azimuthal variation in the length scale of the velocity fluctuations immediately downstream from the orifice. Differences in the exit angle and frequency of oscillation also occur due to the different geometrical configuration of the nozzle. The maximum spreading angle and maximum velocity decay rate increase with an increase in the nozzle expansion ratio (Lee et al, 2003) at the cost of greater pressure loss. The emission benefits of the FPJ are caused by the large spread angle and decay rate. Hence the TOJ is likely to have a trade off between pressure loss and emission performance.

2.8 Research Aims

The TOJ nozzle has been developed to achieve a lower pressure drop than the FPJ nozzle. Therefore it has some operational advantages over the FPJ when firing pulverised fuels such as coal. The aim of the present research is to further the understanding of the flow in the near field region of the TOJ nozzle with a view to provide capacity to optimise the nozzle for efficient use in cement kilns with reduced emissions of NO_x. More specifically this research focuses on one key area, the effect of fluid density variations on the flow through the nozzle.

No two cement kilns are identical in all details of design and operation and therefore the temperature of the secondary air will vary on a case by case basis. Variance in the secondary air temperature implies variation in the density ratio between the fluid leaving the nozzle and the surrounding fluid in the kiln. While it is known how density ratio affects simple jet flow (section 2.4), no previous work has assessed the influence of density ratio on the near field flow from the TOJ nozzle or other related configurations. Changing the flow characteristics of a jet can significantly alter the resulting combustion and therefore it is important to understand how density ratio affects the flow from the TOJ nozzle. This study aims to meet this need. First, it aims to establish the relationship between density

ratio and mean spread, centreline decay, instantaneous jet deflection angle and the oscillation Strouhal number. Second, it aims to determine the relationship between these parameters and the nozzle chamber length at several density ratios. Third, it aims to isolate the influence on the flow due to a change in the density ratio without a simultaneous change in the viscosity ratio. Fourth, it aims to assess the effectiveness of a practical configuration of an industrial burner. For the configuration it aims to assess the influence of a co-annular flow surrounding the TOJ flow, at various momentum ratios, on the mean spread, centreline decay and oscillation Strouhal number.

Chapter 3

Experimental Apparatus and Techniques

3.1 Experimental Methodology

The current work examines the effect of variable density ratio between the jet and ambient fluid spanning the range 0.2 - 5.0 on the flow field emerging from a TOJ nozzle. To achieve this the density of the jet fluid only is varied by mixing various percentages of either helium (0.169 kg/m^3) or sulphur hexafluoride (6.27 kg/m^3) with air as shown in figure 3.1. For the investigation to be meaningful, the effect of variable density ratio must be investigated using a constant basis, the most sensible being either constant Reynolds number or constant momentum flux.

Previous work on variable density jets has shown that the flow development of a simple jet issuing into a lower density gas is more rapid than that of a denser gas with either the same momentum flux or the same Reynolds number (Amielh et al, 1996). It was also shown that the turbulence structure of a jet with variable density is similar to that of a unity density ratio case when compared at similar momentum flux, but was quite different when compared for the same Reynolds number (Ruffin et al, 1994). Entrainment into the flow is also related to the jet's momentum flux (Ricou and Spalding, 1961). This all indicates that momentum flux is an important parameter for the investigation of variable density jets. In

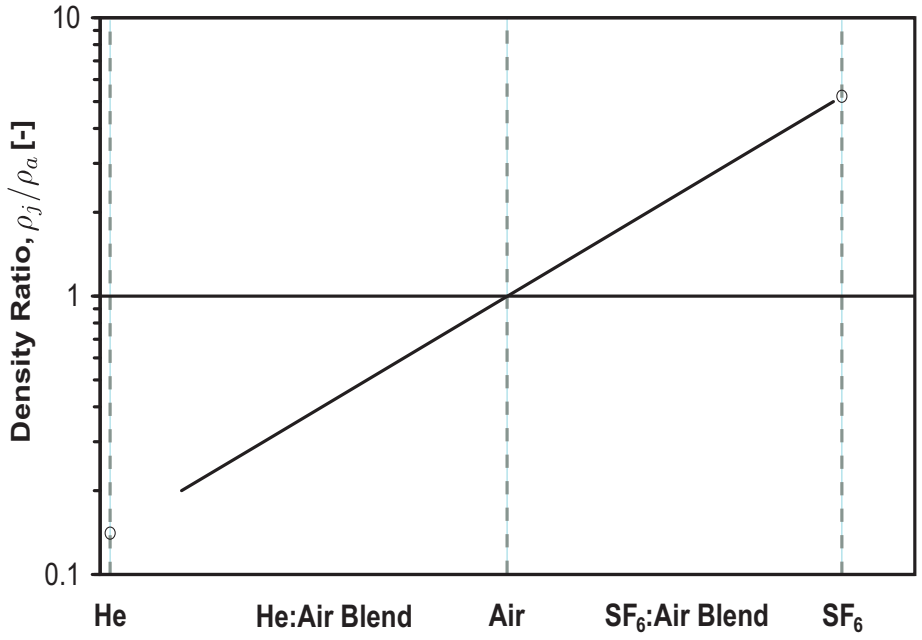

Figure 3.1: Graph showing density ratio's achieved in this work

fact, Ruffin et al (1994) claim that momentum flux is the most relevant parameter for comparing variable density jets. Therefore in this investigation variable density jets are compared at constant momentum flux rather than constant Reynold's number.

When examining flows with variable density the effects of buoyancy may be important (Pitts, 1991). However, in their extension to the review paper of Chen and Rodi (1980), Sautet and Stepowski (1998) have shown that the effects of buoyancy are negligible up to a distance x_m as defined by equation 3.1.

$$x_m = \mathrm{Fr}^{1/2} S^{1/4} d_0/2 \tag{3.1}$$

$$\mathrm{Fr} = \frac{U_0^2}{g d_0(\rho_a - \rho_0)/\rho_0} \tag{3.2}$$

In equation 3.1 Fr is the Froude number (equation 3.2) at the point of injection, S is the density ratio of the jet fluid to the ambient fluid (ρ_j/ρ_a) and d_0 is the jet

nozzle diameter. Using the Froude number calculated at the jet throat (d_{e1}) in equation 3.1, experimental conditions were set such that the effects of buoyancy are negligible over a minimum of 10 chamber diameters from the nozzle exit. This is a sufficient distance downstream to be able to neglect buoyancy over the region of the flow considered.

3.2 Experimental Jet Nozzle

The Triangular Oscillating Jet (TOJ) nozzle studied in the present investigation is similar to that used by Lee et al (2003). It utilises a triangular orifice expanding into an axisymmetric chamber with a small lip at the nozzle exit, as shown in figure 3.2. The chamber diameter, D, is 26.5 mm and the exit lip diameter, d_2, is 21.8 mm. The triangular orifice, which is equilateral in shape, is denoted by the diameter of a circular orifice with equivalent cross-sectional area, d_{e1}. In this study d_{e1} is set such that the ratio of expansion between the orifice and chamber diameters, D/d_{e1}, is equal to 3.5. The length of the nozzle chamber, L, more commonly expressed as the ratio, L/D, is variable over the range $2.02 \leq L/D \leq 2.96$ in increments of $L/D = 0.094$.

3.3 Flow Visualisation

3.3.1 Particle Image Velocimetry

Particle image velocimetry (PIV) is a technique used to measure fluid velocity by the displacement of tracer particles seeded into the flow. The tracer particles are illuminated at least twice within a short period of time by a light source, typically a laser. Images of the scattered light are recorded and compared by statistical methods to determine particle displacements. From knowledge of the particle displacement and the time separation, a velocity can be calculated. Therefore the velocity is measured indirectly as a displacement of the tracer particles in a finite time interval (Westerweel, 1997). Unlike probes such as hotwires, PIV is a “non-intrusive” way to measure velocity, allowing the velocity to be measured

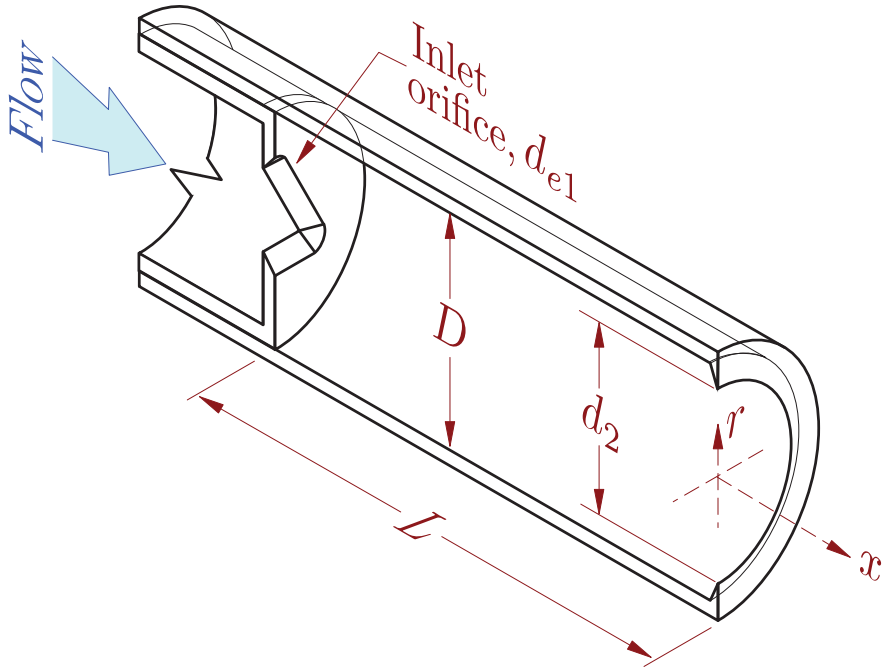

Figure 3.2: A schematic diagram of the TOJ nozzle showing notation.

without changing the flow, and is a "whole field technique", meaning that the velocity can be determined at each point within the plane of the light source from one measurement. Figure 3.3 shows a typical PIV setup.

In its simplest arrangement, PIV measures two components of velocity at each point in a 2-D plane at one instant in time (Adrian, 1997). As shown in figure 3.3 a typical PIV system consists of a pulsed light sheet, which is scattered by the particles in the fluid, a photographic lens, usually aligned at right angles to the light sheet, and an optical recording medium (Adrian, 1997; Raffel et al, 1998). The light sheet is pulsed two (or more) times to produce a series of images of the illuminated particles. Processing the data to determine velocities involves subsampling of sequential images in some particular area known as an interrogation window (Willert and Gharib, 1991). Within the interrogation window an average spatial shift of the particles may be observed from one image to the next, provided that a flow and sufficient particles were present in that region. This spatial shift can be described by a linear digital signal processing model where the sampled region of the first image is the input and the sampled region of the second image is the output at a time δt later.

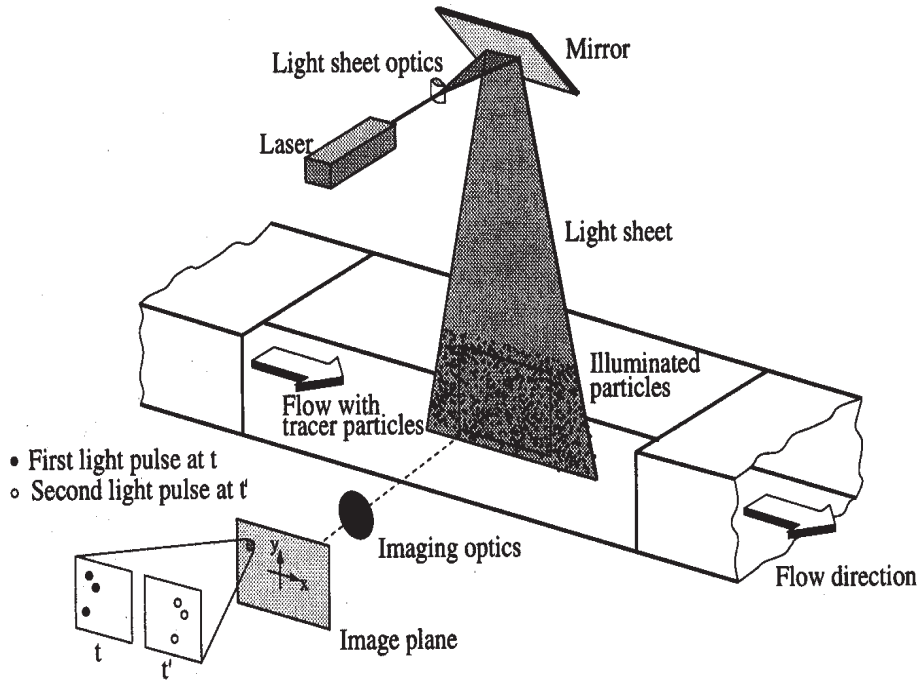

Figure 3.3: A Typical PIV setup (Raffel et al, 1998).

The system itself consists of two components, a spatial displacement function and an additive process (Willert and Gharib, 1991). This is shown schematically in figure 3.4. Measurement noise follows as a direct result of particles moving outside the boundaries of the sampling region and particles disappearing out of the light sheet through 3-D motions (Willert and Gharib, 1991). By calculating the spatial displacement function and knowing the the time interval between the successive images a velocity can be calculated for that interrogation window. As such the velocity measured at each location is averaged over the volume of the interrogation window (Westerweel et al, 1996; Adrian, 1997). The volume of the interrogation window defines the spatial resolution of the measurement. Spatial resolution is typically the biggest limitation of PIV. This is because, if the size of the interrogation window is too small compared with the displacement of the particles, the accuracy of the correlation between the images is reduced, producing erroneous vectors. However increasing the size of the interrogation window reduces spatial resolution, and hence the ability to detect smaller scale motions within the flow, and can lead to the RMS being underestimated.

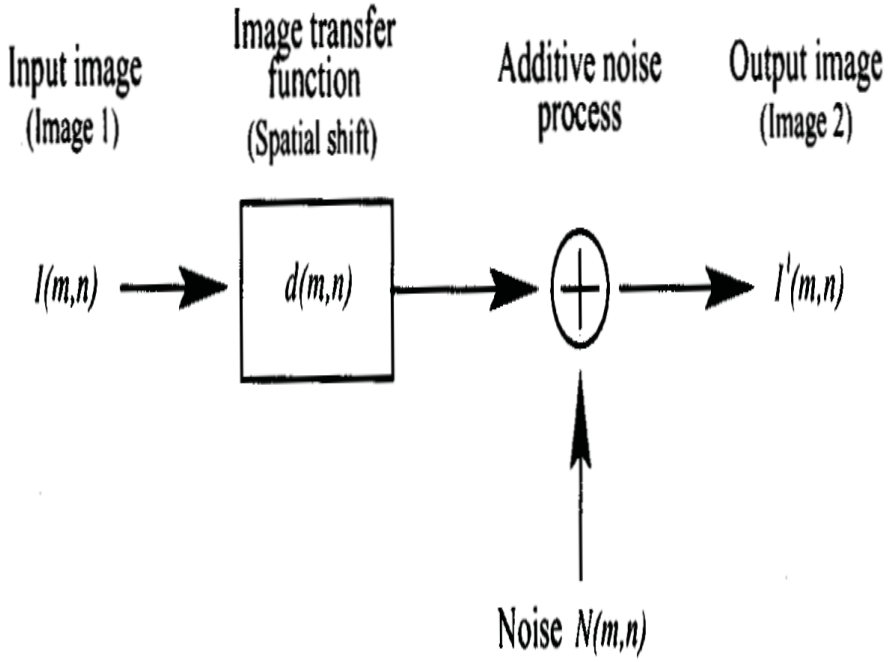

Figure 3.4: Digital signal processing model describing the functional relationship between two successive frames (Raffel et al, 1998).

Calculation of the spatial displacement function can be carried out manually by tracing individual particles. However this is time consuming. Therefore it becomes necessary to analyse the image field within each interrogation window statistically to determine the correct displacements in a flow field (Adrian, 1997). By taking advantage of the correlation theorem, which states that the cross correlation of two functions is equivalent to a complex conjugate multiplication of their Fourier transforms, the cross correlation of successive images is performed in the frequency domain (Raffel et al, 1998). Figure 3.5 shows the process of correlation schematically.

When processing PIV data statistically, erroneous velocity vectors, known as "outliers", are sometimes calculated. An "outlier" is a vector that results from a mismatch in the image patterns and will appear to be random in both direction and amplitude (Huang et al, 1997). The major factors responsible for outliers in a PIV vector field are that some interrogation windows contain insufficient particles for accurate correlation, the presence of strong velocity gradients, or a highly 3-D flow (Huang et al, 1997). Generally the number of outliers is small

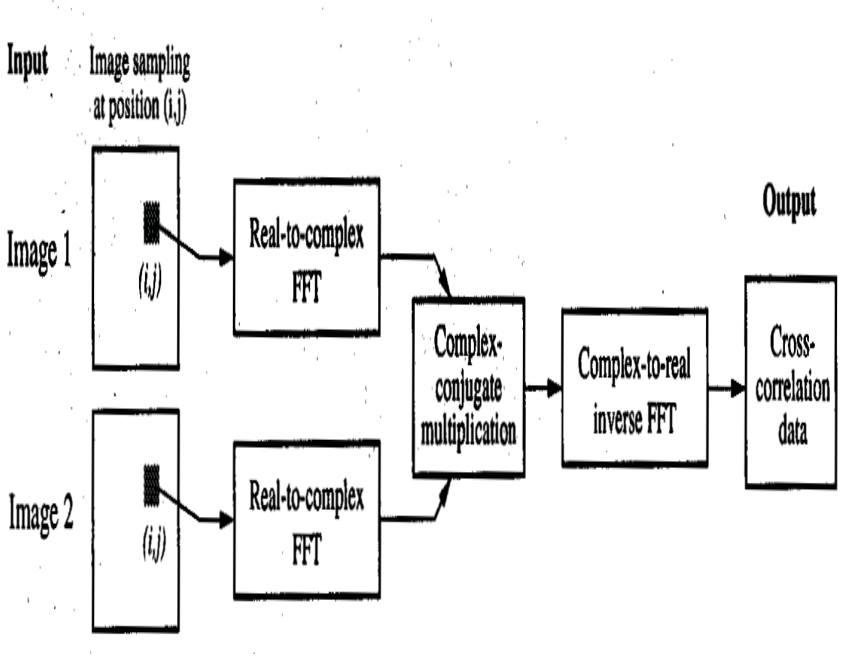

Figure 3.5: Implementation of cross correlation using fast Fourier transforms (Raffel et al, 1998).

(∼5%), however some will always be present as there is always a finite probability that an interrogation window will yield an outlier (Westerweel, 1994). Since outliers exhibit an unexpectedly large deviation with respect to other vectors nearby, comparison with these other vectors can be utilised to detect outliers. Three common ways to detect outliers is by comparison with the global mean, the local mean or the local median (Westerweel, 1994). Essentially, the local methods determine the validity of a vector by comparison with the eight vectors which surround it, whereas the global method checks validity by comparison with the whole flow field. Since the flow field may contain flow structures such as vorticies, the local mean method is usually much more reliable than the global mean method. However, it is also subject to larger errors in the detection of outliers since some of the surrounding vectors could also be outliers. The local median method uses the same information as the local mean method to detect outliers, however it is significantly more robust than the local mean method (Westerweel, 1994). This is because when calculating the local median, any outliers will have a large deviation from the expected value and will therefore lie

at either the beginning or the end of the rearranged sequence (the median being the nth element of a sequence containing $2n$ - 1 elements). Therefore should any outliers be present in the vectors surrounding a vector in question, an incorrect assessment of that vector's validity is much less likely.

The PIV technique relies on the use of tracer particles in the flow to scatter the light. Therefore for accurate PIV measurement, the tracer particles should accurately follow the flow to the required turbulent scale, not alter the fluid properties or flow, not interact with other particles, and be homogeneously distributed over the fluid in the region of interest (Westerweel et al, 1996; Westerweel, 1997). However the size of the particles must also be large enough to cause sufficient scattering of the light for detection by the recording media. Therefore a compromise is necessary between reducing the particle size to improve flow tracking and increasing the particle size to improve light scattering (Melling, 1997). Higher levels of seeding density reduce the level of uncertainty in the resulting velocity field, since more particle pairs are taken into account when correlating the interrogation window (Willert and Gharib, 1991). Increased particle density also reduces the occurrence of outliers (Westerweel, 1994). However increasing the seeding density too much can lead to the particles influencing the flow and can create issues with the images due to optical transparency in the light sheet (Westerweel, 1994). The tracer particles should be introduced into the flow in a sufficient and stable concentration, with a spatially uniform distribution well upstream from the region of interest in the flow. This ensures that seeding occurs everywhere in this region, allowing velocities to be resolved over the entire region (Melling, 1997).

3.3.2 Experimental Setup

Velocity measurements were taken using a digital cross-correlation particle image velocimetry (DPIV) system at the Turbulence, Energy and Combustion (TEC) laboratory of the University of Adelaide. The TOJ nozzle used in the experiments is described in Section 3.2. The working fluid was introduced through the nozzle into ambient air. The rate at which the fluid was introduced was set so that a constant throat momentum flux of 0.06 kgms^{-2} was maintained. The reason

for this is discussed in Section 3.1. Gas flow rates were measured using the appropriate Fischer & Porter tube and float combinations from the following list; 1/2-21-GSVT-45, 1/2-21-GUSVT-410, 1/4-10-SA, 1/4-25-SA. Gases were mixed together to form the correct density well upstream of the nozzle, then supplied to the nozzle via a straight pipe of development length 50 pipe diameters. No other flow conditioning was used.

Both the jet and an ambient co-flow of negligible (3.92×10^{-5} kgms^{-2}) momentum, were seeded with atomised olive oil with a nominal droplet diameter of 0.6 μm. With the criterion of *amplitude of particle oscillation / amplitude of fluid oscillation* > 0.99 equation 3.3 can be derived from expressions described by Melling (1997), where f is the frequency response of the particles, ν is the fluid kinematic viscosity, d_p is the particle diameter and σ is the particle to fluid density ratio. Substituting values from the experimental conditions into equation 3.3 predicts, in the worst case, a frequency response of 17.1 kHz. Therefore the particles are sufficiently small to be effective flow tracers even in high shear regions at the edge of the jet. The laser sheet (described in Section 3.3.3) was aligned with the nozzle centreline and configured to provide uniform intensity through the exit plane. The orientation of the triangular orifice with respect to the light sheet is shown in figure 3.6. The camera was aligned normal to the light sheet and positioned to image the emerging flow over the range $0 < x/D \leq 3$. The experimental arrangement is shown in figure 3.7.

$$f = \frac{0.408\nu}{d_p^2\sigma} \tag{3.3}$$

3.3.3 Laser and Optics

The tracer particles were illuminated by laser pulses from a Quantel Brilliant Twins double-cavity Nd:YAG laser. This laser is specifically designed for PIV applications, each of the laser heads being independently triggerable. The first harmonic output of the Nd:YAG ($\lambda = 1024$nm) is frequency doubled to produce an output beam in the visible wavelength range ($\lambda = 532$nm). These visible components from each of the laser heads are co-aligned and the fundamental

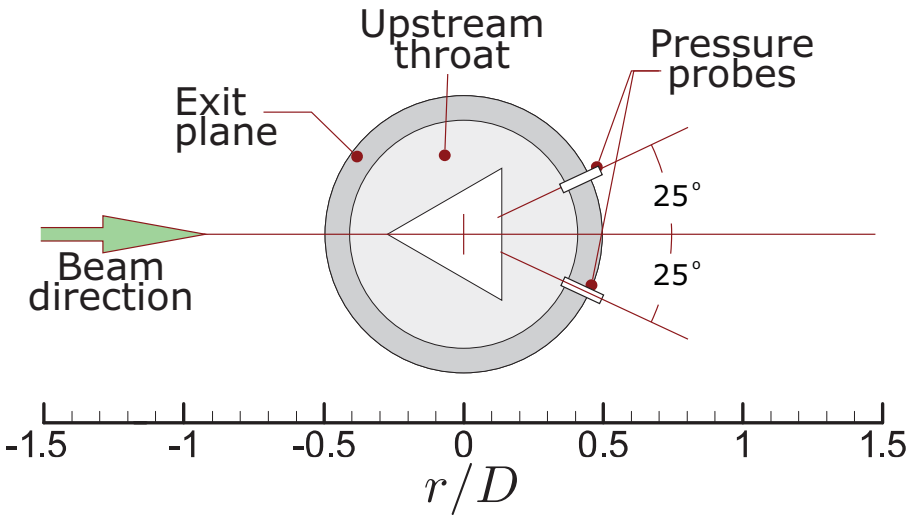

Figure 3.6: Orientation of the light sheet and position of pressure probes with respect to the orifice as seen from above the nozzle (View A).

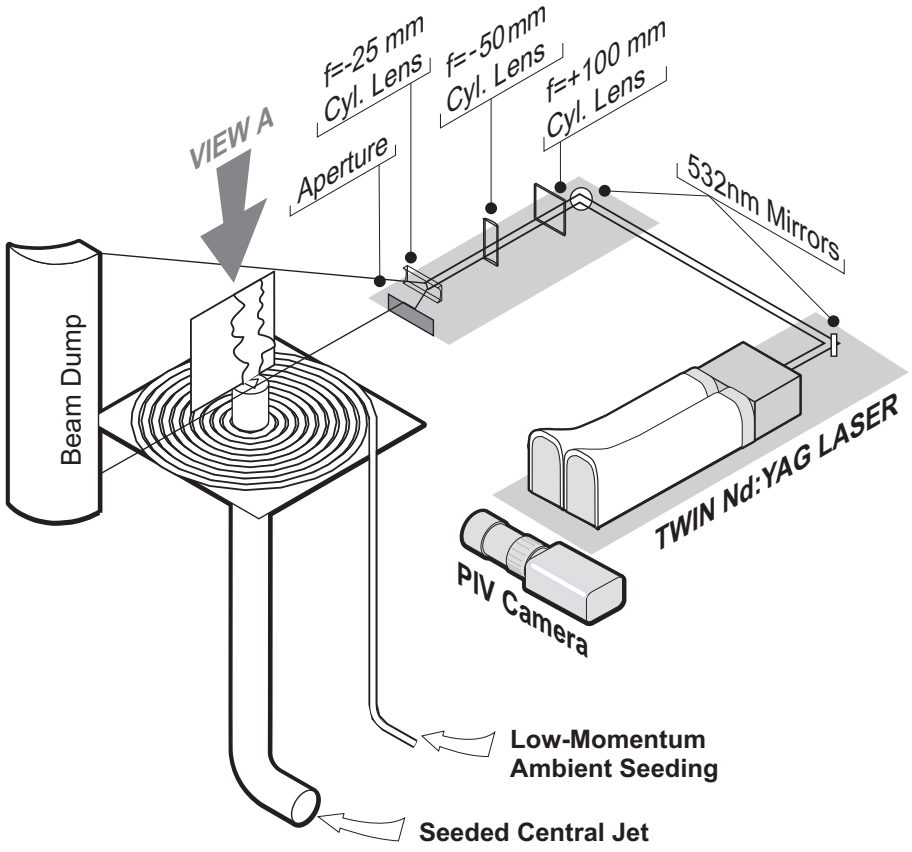

Figure 3.7: Schematic diagram of the nozzle and PIV arrangement.

infrared component is dumped. The output energy of each laser is ∼250 mJ per pulse at $\lambda = 532$ nm, although energies of up to 400 mJ per pulse are achievable.

The laser beams are directed towards the imaged area using two dichroic mirrors, and are formed into a light sheet of suitable dimensions. Initially, the horizontal thickness of the laser beam is reduced by passing it through a cylindrical plano-convex lens (f = 100mm). A second cylindrical lens (f = -50mm) is placed upbeam from the focal point. Adjusting the separation between these two lenses allows the thickness of the laser sheet in the imaging region to be controlled. This is an important consideration for oscillating jet flows in which the out-of-plane component of resolved velocities may be large. Finally, the laser beams are formed into a vertical sheet by a strong negative cylindrical lens (f = -25mm). The resulting laser sheet is approximately 2.0 mm thick in the imaged region. This thickness of laser sheet is necessary to avoid significant loss of useful image pairs due to the large out-of-plane motion in the unsteady flow. The light sheet thickness thus becomes a limiting dimension in the spatial resolution of the measurement.

To assess the suitability of the light sheet thickness, an oscillation frequency of 100 Hz is conservatively assumed. This is greater than any measured oscillation frequency as presented in chapters 4, 5, 6 and 7. Using the maximum temporal separation between the laser pulses, as described in section 3.3.5, the expected rotation between the laser pulses is 1.08°. By use of trigonometry this angular rotation corresponds to a tangential displacement (or out-of-plane displacement) of approximately 0.25mm, which is one eighth of the light sheet thickness. Although turbulent structures will affect the magnitude of the out-of-plane displacement, this estimate shows that the out-of-plane displacement is less than one third of the light sheet thickness, and therefore should not have a significant impact on the two captured displacement components. To actually determine the out-of-plane displacement, a technique such as stereoPIV could be used, allowing all three displacement components to be captured. However, stereoPIV is a more complex technique to setup, operate and process data than standard PIV. Since standard PIV is able to achieve the aims of this work it is used in preference to stereoPIV to avoid unnecessary experimental complexity.

3.3.4 Camera

The camera used for imaging was a Kodak MegaPlus ES1.0 operated in the triggered double exposure mode. The CCD in this camera is 1008 pixels wide by 1018 pixels high. The collection optics comprised a Nikon ED 70-300 mm telephoto lens (set to 110 mm) coupled to the camera C-mount with an adapter. The aperture was fully opened (f# = 4). The imaging region was 65 mm × 65 mm, corresponding to approximately 65 μm × 65 μm per pixel. Use of reference target shots showed that the imaging optics produced a true representation of the imaged region. Therefore image warping was not required prior to PIV processing. Imaging with the camera slightly out of focus increases the particle image size, and allows the resulting accuracy achieved for the determined velocities to be sub-pixel. Using a technique known as 'frame-straddling', it is possible to image the first laser pulse at the end of the first exposure and the second laser pulse at the beginning of the subsequent exposure. The temporal separation between the laser pulses can then be as little as 1 μs.

3.3.5 Timing

The output signal from the flashlamp (10 Hz TTL) of the primary laser was used to initiate the timing of data collection. The 10 Hz output was used to trigger both the camera, and a Stanford Research Systems DG535 pulse delay generator. The delay generator was then used to trigger the flashlamp of the secondary laser. The delay between the laser flashlamps and Q-switches was set by internal timing electronics, so that the delay between the laser pulses could be altered without adjusting the Q-switch delay. The temporal separation between laser pulses was adjusted from 4 to 30 μs, depending on the flow field. Data were collected from the camera at 20 Hz into a memory buffer on the data storage computer. At the end of each run, the entire data set of 440 PIV image pairs was saved to hard disk for subsequent processing.

3.3.6 Image Correction

The camera used for data collection had two defective pixels in the CCD array, which permanently record at maximum intensity. Both of these pixels resulted in some of the surrounding pixels recording at significantly higher intensity. When run through the PIV processing algorithm, these defects are detected as false peaks. As there is no shift in location between the successive images a value of zero is calculated for the velocity in that interrogation region. Figure 3.8a shows the effect such a defect would introduce to the mean of a data set taken using a relatively uniform flow field, if uncorrected.

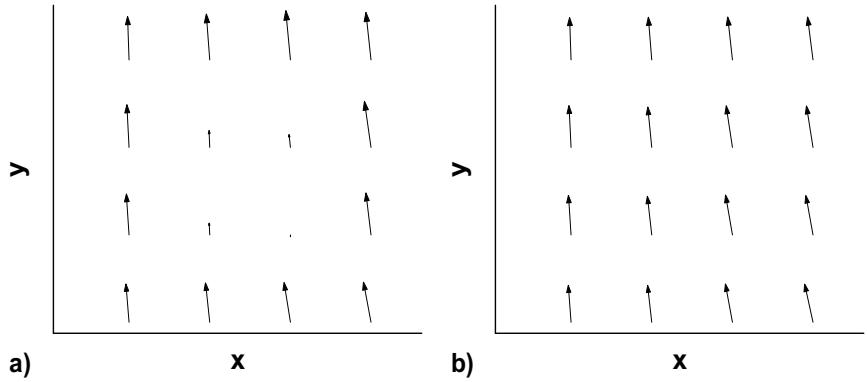

Figure 3.8: Effect of camera defects on the mean of a relatively uniform velocity field a) before image correction and b) after image correction.

Increased seeding density in the flow reduces the effect of these defects. This is in part due to a reduction in the level of uncertainty in the resulting velocity field since more particle pairs are included in the correlations. In addition, a higher seeding density acts to mask the effect of the defect as the probability of a particle genuinely being imaged by that region of the camera CCD is increased. However, whilst increasing the seeding density reduces the effect of the defect it can still be noticed easily in the mean of a data set. Therefore to ensure that the data output from the PIV processing is accurate, the defect resulting in the images from the faulty CCD was removed via an image correction. This method, described below, essentially removes the defect while still maintaining image integrity.

To determine the exact location of the faulty pixels and the associated effect on any of the surrounding pixels a “black” image was examined. Figure 3.9 is a

schematic diagram of a faulty pixel showing the adjacent pixels surrounding it that are also affected. The pixel location B2, shown in blue, is the location of the faulty pixel, which always has a value of maximum intensity. The pixels B3 and C2, shown in pink, were affected by "blooming" so that, for the black image, they had a value that was approximately half that of the maximum. Finally the pixel location C3, shown in yellow, had a value that was approximately a quarter of the maximum.

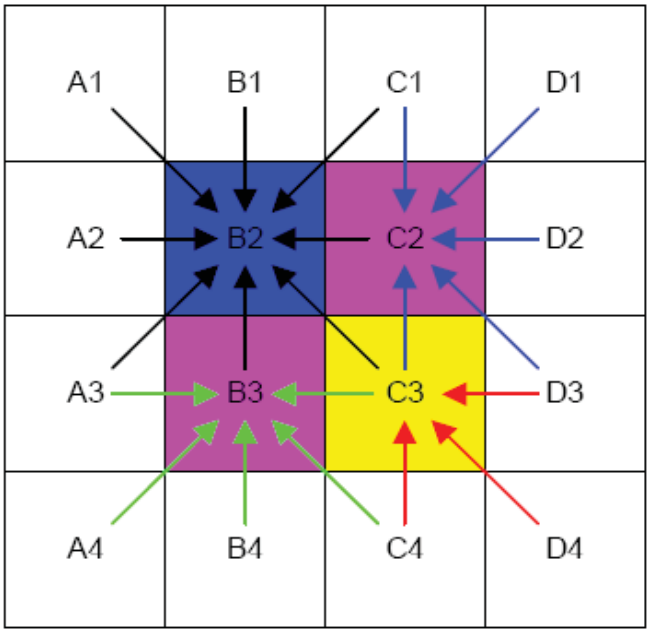

Figure 3.9: Schematic of image correction for faulty pixels.

To remove the effect of the faulty pixels an image correction algorithm was written (in MatLab) to replace the value of the faulty pixels with a weighted average of the pixels that surround it. The correction was also applied to the surrounding pixels affected by the camera defect, described above. The steps taken by the algorithm are:

- Pixel C3 is replaced by C3', a weighted average of pixels C4, D3 and D4 (as shown by the red arrows in figure 3.9)
- Pixel C2 is replaced by C2', a weighted average of pixels C1, C3', D1, D2 and D3 (as shown by the blue arrows in figure 3.9)

- Pixel B3 is replaced by B3', a weighted average of pixels A3, A4, B4, C3' and C4 (as shown by the green arrows in figure 3.9)
- Pixel B2 is replaced by B2', a weighted average of pixels A1, A2, A3, B1, B3', C1, C2' and C3' (as shown by the black arrows in figure 3.9)

PIV processing of the resulting corrected images gives a much more accurate representation of the mean flow field resulting from a relatively uniform flow. Figure 3.8b shows the same region of the flow shown in figure 3.8a after image correction has been applied. This shows that the image correction has removed the artefact created by the camera defect.

3.3.7 Data Processing

Processing of the PIV image pairs was performed using Pivtec's PivView (v 2.1) software. The time delay between the laser pulses was selected so that the final interrogation region could be set to 32 × 32 pixels, with 50% overlap. This results in an effective spatial resolution for the velocity measurements of 2.08 × 2.08 × 2.0 mm^3. The resulting vector field is comprised of 62 × 62 vectors. A 4-pass multi-grid correlation algorithm was used to correlate between the two image pairs. The initial interrogation region was 96 × 96 pixels. This was then refined to a 64 × 64 pixel region and then finally a 32 × 32 pixel region for the final two passes. The correlation image was scanned for peaks using a least squares Gaussian fit on a roaming 3 × 3 pixel mask.

Figure 3.10 shows some example PIV images. Figure 3.10a shows a raw particle field which was collected as half of a raw image pair, figure 3.10b shows the instantaneous vector field produced by applying PIV processing to that raw image pair and figure 3.10c shows the average vector field produced when that instantaneous image is averaged with the other 439 instantaneous fields that form an examined case. In figure 3.10 the arrows show the flow direction and the contours show the velocity magnitude.

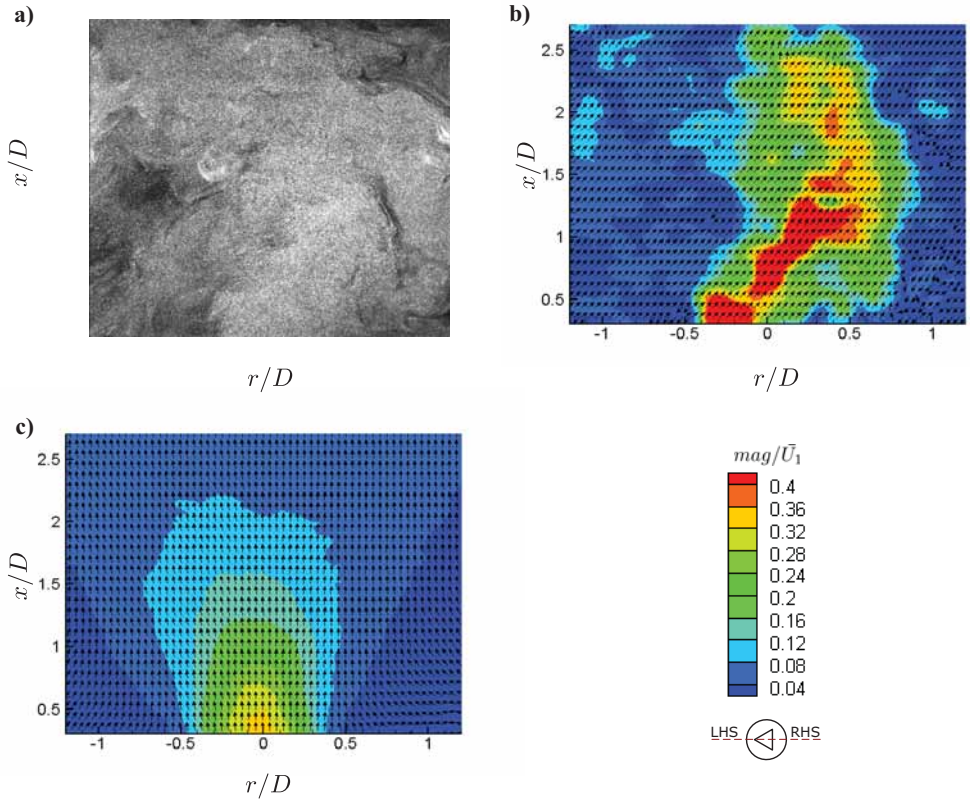

Figure 3.10: Example PIV images: a) Raw particle field, b) Instantaneous vector field and c) Average vector field.

3.3.8 Outlier Detection

Outliers (erroneous vectors) were detected in a two stage process. The first stage was done using the "universal" outlier detection method as described by Westerweel and Scarano (2005). This method is an adaptation of the median test in which the median residual is normalised with respect to a robust estimate of the local variation of the velocity. Westerweel and Scarano (2005) show that the normalised median test yields a more or less "universal" probability density function for the residual and that a single threshold value can be applied to effectively detect spurious vectors. A single detection threshold for the original median test will, in contrast, tend to reject part of the valid measurement data in turbulent regions of the flow and accept part of the spurious data in laminar regions of the flow (Westerweel and Scarano, 2005). A lower value of the detection threshold leads to more stringent detection, while a higher value results in a less stringent detection. Detection was carried out on a 3×3 grid with a threshold value of 2.5. This ensures that obviously erroneous vectors are removed while those that are fluctuations resulting from the 3-D nature of the flow are not detected as outliers.

The first stage of the process compared vectors against other vectors resulting from the same image. The second stage statistically compared vectors against the corresponding vectors that result from the other images that form the data set. To conduct the analysis the mean and standard deviation was calculated for each location in the data set. Each vector was then compared with its corresponding mean. If the difference between the vector and the mean was greater than three standard deviations, then the vector was deemed to be an outlier.

Outlier detection was carried out post-processing using a MatLab algorithm since PivView doesn't allow outlier detection via these methods. This means that any information stored by PivView relating to alternate correlation peaks determined during the PIV processing was therefore unable to be used as a suitable alternate vector in the event that an outlier was detected. As such, any outliers detected are only able to be dealt with either by removing them from the vector field or by replacing them with a vector equal to the weighted average of the surrounding non-erroneous vectors (interpolation). Cases for either method can be argued. For example, replacing vectors by interpolation effectively "creates" data and

therefore raises questions over the data's validity. However removing vectors may reduce the statistical convergence of the resulting data. Therefore an analysis on the sensitivity of removing vectors versus replacing vectors on the mean and RMS statistics was conducted.

To conduct the sensitivity analysis, all outliers detected were first replaced via interpolation. Then the mean and RMS derived from subsets of the data selected at random were compared with the mean and RMS derived from the complete data set. This is analogous to removing, at random, $(S_f - S_s)$ vectors from the complete data set, where S_f is the size of the complete data set and S_s is the size of the subset. The analysis was conducted over a range of subset sizes.

For each subset size the mean and RMS statistics derived from ten independently selected subsets was compared with the statistics derived from the complete data set. This was done using equation 3.4 where x_i is the value of the mean or RMS at a discrete location in one of the ten subsets and x_f is the value at the same location in the complete data set.

$$\text{MeanDifference} = (\frac{1}{10}\sum_{i=1}^{10}(x_i - x_f)^2)^{1/2} \tag{3.4}$$

Figure 3.11 shows the mean difference between the statistics derived from data subsets and those of the complete data set which contains 440 image pairs. The value shown in each case is an average based on twelve discrete locations in the flow field (Radial locations r/D -0.5, 0, 0.5. Axial locations x/D 0.5, 1.0, 1.5, 2.0.). Since the cases on which the analysis was conducted span the range of density ratios, ρ_j/ρ_a, investigated it can be concluded that this result is representative of all the experimental data.

While conducting outlier detection, the number of outliers detected at any discrete location in the resulting ensemble average is logged. Therefore the total number of vectors to be either replaced or removed is known. Examination of this showed that in the worst case the total number of outliers at any location was less than 10% of the size of the data set. Figure 3.11 shows that the difference in the result of the mean and RMS is at most 2% if outliers are removed rather than replaced by interpolation. Since the difference is within the overall experimental

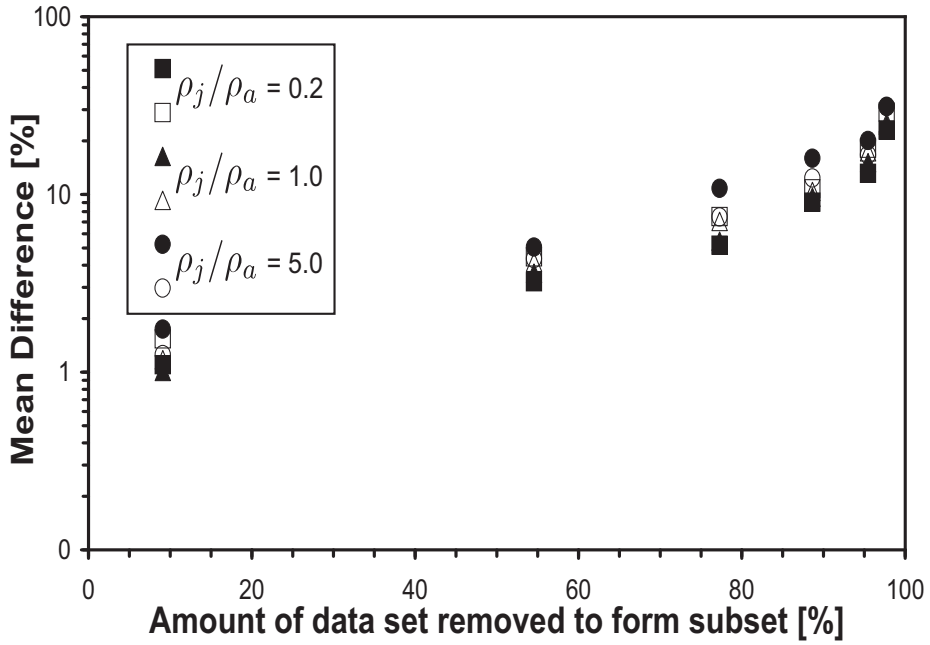

Figure 3.11: Mean difference between data subsets and the complete data set (Solid = mean, Hollow = RMS)

uncertainty it was deemed that outliers would be removed when examining the ensemble averaged flow field so as not to reduce the data's validity by "creating" data in the interpolation process.

3.3.9 Half Width Analysis

To assess the gradient of spread of the jet emerging from the TOJ nozzle, the half width, $r_{1/2}$, was used. The half widths were obtained from the ensemble averaged flow fields. Due to asymmetry associated with the triangular orifice $r_{1/2}$ is measured as the radius at which the mean velocity is half of the local maximum value, rather than the centreline value. The asymmetric nature of the flow also means that the mean spread, $\bar{r}_{1/2}$, was measured as the average of the jet half widths on either side of the jet centreline.

3.3.10 Instantaneous Jet Deflection Angle

3.3.10.1 Conditional Averaging

The jet that emerges from the nozzle at any instant in time is significantly different from the time averaged flow. Therefore, to assess the appearance of the instantaneous jet, the data were conditionally averaged. This was done by searching through each data set to find instances for which the emerging jet was deemed to be within the plane of the light sheet.

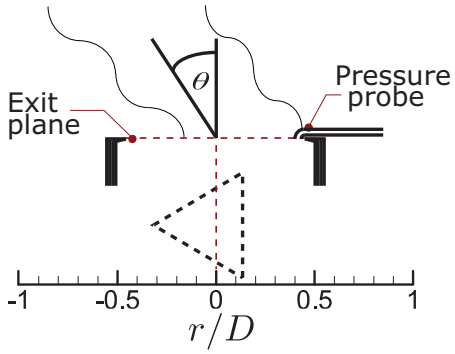

Figure 3.12: Schematic representation of instantaneous jet deflection angle, θ, and position of pressure probes with respect to the nozzle exit

Since the angle of the jet within the plane of the light sheet depends upon the phase, the images that show the greatest angles of deflection can be assumed to correspond to phase angles that are best aligned with the plane of the light sheet. On this basis, a representative, although not absolute, measure of the instantaneous deflected jet is taken as the average of the six images with the greatest angle of deflection, θ, in the $x - r$ plane, as shown in figure 3.12. These were selected by determining the slope of the linear line of best fit for the maximum velocity magnitude for each image over the range $x/D < 1.5$. As an additional condition, the line of best fit for selected images was required to have a correlation coefficient of greater than 0.8. This allows for some cycle-to-cycle variations, but ensures that selected images correspond to the jet being in the plane of the light sheet.

3.3.10.2 Probability Density Analysis

Due to the low sample size a quantitative measure of θ cannot be obtained by the use of conditional averaging of the data. Therefore to obtain a quantitative measure of θ a method was devised which is an adaptation of the streamer technique used by Lee et al (2003), where they anchored a silk-ribbon streamer to the centre of the nozzle exit and took long exposure photos of its motion. The visible extremes of the ribbon in the resulting image can then be considered to correspond to the instantaneous jet deflection, θ, although Lee et al (2003) incorrectly called this jet spreading.

A streamer in the flow will follow the maximum velocity magnitude. Therefore, adapting the streamer method to PIV data is done by searching for the radial location of the maximum velocity magnitude at each x/D value in each vector field. Then, summing the number of instances at each spatial location over the 440 vectors fields in each data set results in a probability density plot. Selecting a minimum threshold then determines an edge contour which can be considered as a measure of θ.

3.4 Frequency Analysis

To determine the frequency at which the jet oscillates, a series of pressure vs time traces were recorded. Two Pitot probes with a nominal diameter of 1 mm were placed at the edge of the nozzle exit lip facing upstream as shown in figure 3.12. They were located adjacent to one of the triangular orifice sides and were separated by 50 degrees, 25 degrees either side of the centreline, as shown in figure 3.6. The pitot probes were connected to an in-house differential pressure manometer and A/D converter, which was sampled at a rate of 1 kHz. Two independent data sets were recorded for each probe, each being 40 seconds in length, resulting in four pressure vs time traces suitable for frequency analysis.

Determination of the dominant frequency of oscillation, f_{osc}, was calculated using three separate methods. The first method determined the frequency spectrum using a simple 8192 point FFT on each of the four pressure traces, and then located the frequency at which the maximum power was recorded. The second

method used the Burg Maximum Entropy method, as described in Kay and Marple (1981), on each of the four pressure traces and then similarly located the frequency at which the maximum power was recorded. Using this method requires the input of a model order to determine the frequency spectrum. Due to significant noise in the signal, were the order to be automatically selected via either the Final Prediction Error or the Akaike Information Criterion, as described in Kay and Marple (1981), a sensible result would not be obtained. Landers and Lacoss (1977) suggest that when significant noise is present, a larger model order will produce a better spectrum, allowing the location and size of narrow band components to be determined. It is suggested that model orders of N/3 to N/2 work well for small data sets ($\sim$ N=100-500). As the data sets are two orders of magnitude larger, a smaller model order of N/40 was selected. This produces sensible results for the data.

The third method used to determine the dominant frequency, intended as a check, was a purpose written peak-detection algorithm used to "manually" count peaks in the data sets. To do this, a threshold value was set on the data traces and then any value above that threshold was deemed to be part of a peak, while any value lower than the threshold was not part of a peak. Once the data sets were converted into a string of "peak" or "not-peak" values, the mean peak separation time was calculated and then converted into a frequency. Due to the presence of high frequency noise a rectangular smoothing was first applied to the data to reduce the influence of the noise. The amount of smoothing applied was selected to make the resulting data set both non-skewed and uni-modal. In other words, the median peak separation and the mode peak separation were both within a small tolerance (corresponding to < 2Hz) of the mean peak separation. Since the mode is the value in the sequence which occurs the most frequently, determination of the mode for a sequence in which each value occurs only once is not directly possible. However, the Kernel Density Estimation (or Parzen Window method), which essentially blurs point samples to produce a continuous estimate of the probability density function, can be used to estimate the mode.

Chapter 4

TOJ under Variable Density Conditions

4.1 Introduction

The operating temperature of the co-flowing (secondary) combustion air in a rotary kiln is high, typically 600-1200^{o}C, depending on the process and the heat exchanger. However this temperature can vary from ambient during start up and during operation by several hundred degrees. The high temperature leads to a density difference between the jet fluid and the co-flow fluid. An understanding of the influence of this density difference is important for the purpose of nozzle optimisation. To meet this need, therefore, the aim of the present chapter is to investigate the effect of the density ratio between the jet and ambient fluids on the flow in the near field of the emerging flow from a TOJ nozzle.

The parameters used in the investigation are as follows. As described in section 3.3.2 the jet fluid is introduced through the nozzle with a momentum flux of 0.06 kgms^{-2}. The bulk mean velocity and Reynolds number for each case as a result of this momentum flux are shown in table 4.1. The nozzle chamber length parameter, L/D, is fixed at 2.49, with all other nozzle dimensions as described in section 3.2. The density ratio of the jet fluid to ambient fluid is varied on a Log_5 scale between 0.2 and 5.0 meaning the two extremes are separated by a factor of 25.

Gas mixture	ρ_j/ρ_a	$\bar{U}_1$ [ms^{-1}]	Re [$\times 10^3$]
He 93.1% - Air 6.9%	0.20	74.46	7.3
He 81.6% - Air 18.4%	0.30	60.89	9.0
He 64.3% - Air 35.7%	0.45	49.79	11.2
He 38.5% - Air 61.5%	0.67	40.72	14.1
Air 100%	1.00	33.30	17.9
SF_6 11.7% - Air 88.3%	1.50	27.23	22.3
SF_6 29.3% - Air 70.7%	2.24	22.27	28.1
SF_6 55.6% - Air 44.4%	3.34	18.21	35.9
SF_6 94.9% - Air 5.1%	5.00	14.89	47.2

Table 4.1: Operating conditions for variable density TOJ.

4.2 Results and Discussion

Figure 4.1 presents the axial velocity component of the ensemble averaged flow fields, $u/\bar{U}_1$, for all density ratios examined. Here the axial component, u, of the velocity is normalised by the bulk mean orifice velocity $\bar{U}_1$. In this figure it can be seen that, as ρ_j/ρ_a is increased, the contour envelope becomes shorter and broader, indicating a greater jet spread and faster mean jet decay. This is the opposite trend to that which occurs for a free jet (Era and Saima, 1977; Richards and Pitts, 1993).

It is also evident that the emerging flow is not axisymmetric, with the velocity being slightly higher on the side where r is positive than for that where r is negative as defined in figure 3.6. This is consistent with the finding of Lee et al (2003), that the jet is preferentially distributed in three "lobes" corresponding to the flat sides of the triangular orifice.

Figure 4.2a shows the normalised mean half widths, $\bar{r}_{1/2}/D$, and figure 4.2b shows the gradient of spread for the TOJ nozzle at each of the density ratios investigated. The gradient of spread, $\Delta\bar{r}_{1/2}/\Delta x$, was determined from the half widths over the range $x/D = 1.25$ - 2.0. Together they show that a decrease in ρ_j/ρ_a below unity results in a corresponding decrease in the jet spread. However an increase of ρ_j/ρ_a above unity has a much less significant impact on the jet spread, with the spread in this region becoming somewhat independent of changes in ρ_j/ρ_a. At first sight, this may appear to contradict the well known dependence

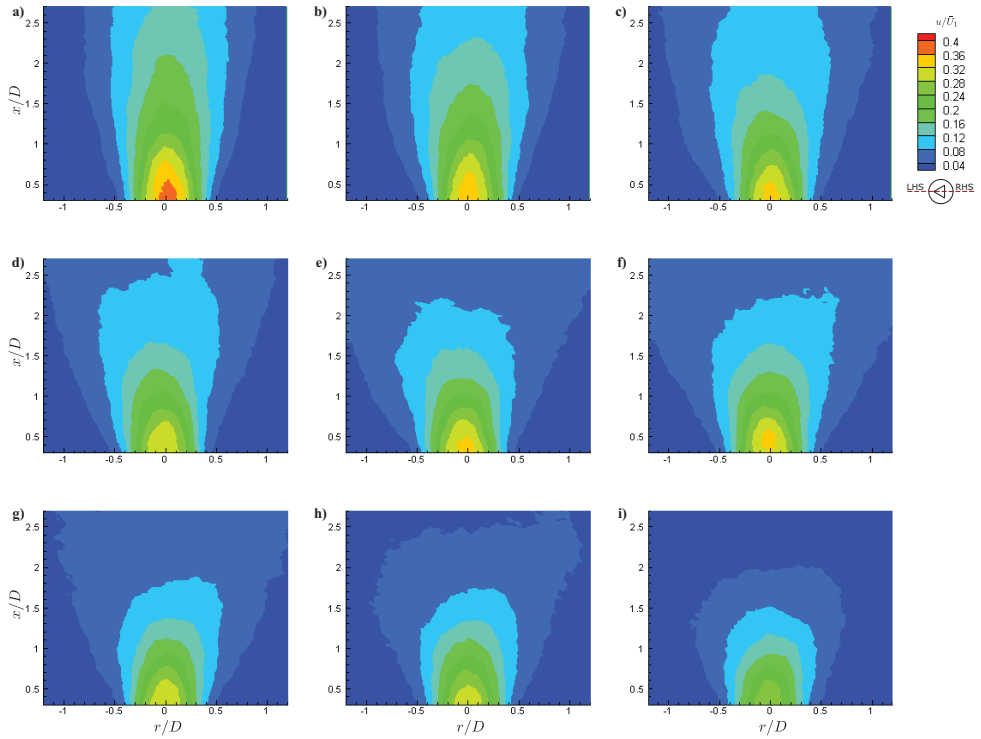

Figure 4.1: Axial velocity component of the ensemble averaged flow fields, $u/\bar{U}_1$, for density ratios ρ_j/ρ_a = a) 0.2, b) 0.3, c) 0.45, d) 0.67, e) 1.0, f) 1.5, g) 2.24, h) 3.34 and i) 5.0.

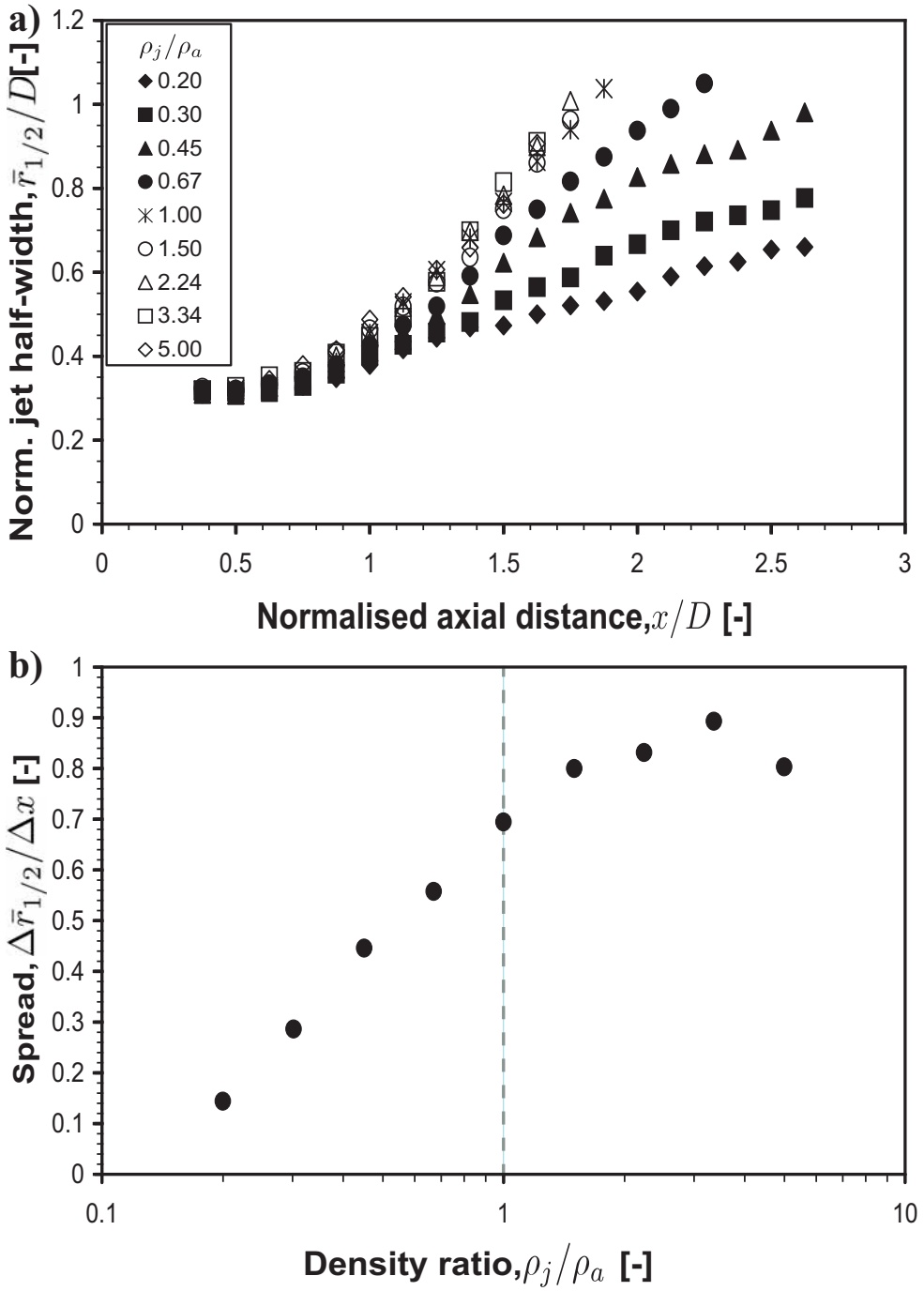

Figure 4.2: a) Mean half widths, and b) gradient of spread for the TOJ nozzle at various density ratios, ρ_j/ρ_a.

of the spreading angle for a free jet (Era and Saima, 1977; Richards and Pitts, 1993). That this is not the case for the TOJ (figures 4.1 & 4.2) is attributed to the partial confinement of this jet within the nozzle.

The flow upon entering the chamber re-attaches to the chamber wall. While the point of re-attachment oscillates, there is a preference for it to be aligned axially with one of the sides of the triangle (Lee et al, 2003). Lateral spreading of a jet following re-attachment to a wall has previously been established (Law and Herlina, 2002). The lateral spreading of a jet on a curved wall results in the jet having a cross-sectional shape resembling a kidney. Wong (2004) has shown this "kidney" shaped appearance in his investigation of a jet emerging from the nozzle exit of a FPJ (although the jet evolves toward a circular cross-section further downstream). As the TOJ flow is closely related to that of the FPJ this trend also can be expected to apply for the TOJ.

As the jet leaves the nozzle chamber it is influenced by the exit lip, and caused to deflect across the nozzle axis (Nathan et al, 1998). The angle at which the jet is deflected will influence the mean gradient of initial spread. It is expected that a larger deflection of the jet across the axis will lead to an increase in the mean initial jet spread and hence in $\bar{r}_{1/2}$. Therefore figure 4.2 implies that decreasing ρ_j/ρ_a below unity will lead to a decrease in the jet deflection while increasing ρ_j/ρ_a above unity will lead to only a small increase in the jet deflection.

Conditionally averaging the instantaneous velocity data allows the instantaneous deflection angle of the jet, θ, to be observed. The method used to conduct the conditional average is described in section 3.3.10.1. The results are shown in figure 4.3. Due to the small sample size used to produce the average, the resulting flow field is a representative measure of θ, albeit with large tolerance. Therefore, the contours in figure 4.3 should be treated with some caution. Nevertheless, they provide an interesting and indicative trend.

Figure 4.3 shows the normalised axial velocity component of the conditionally averaged flow fields for all density ratios investigated. As ρ_j/ρ_a is decreased below unity, θ can be seen to become smaller. Figure 4.3 also shows that at low ρ_j/ρ_a, the jet turns back to the nozzle axis beyond $x/D = 1.5$. The presence of jet curvature in the conditionally averaged images has two possible explanations. Firstly Mi and Nathan (2005) have previously observed the phenomenon of jet

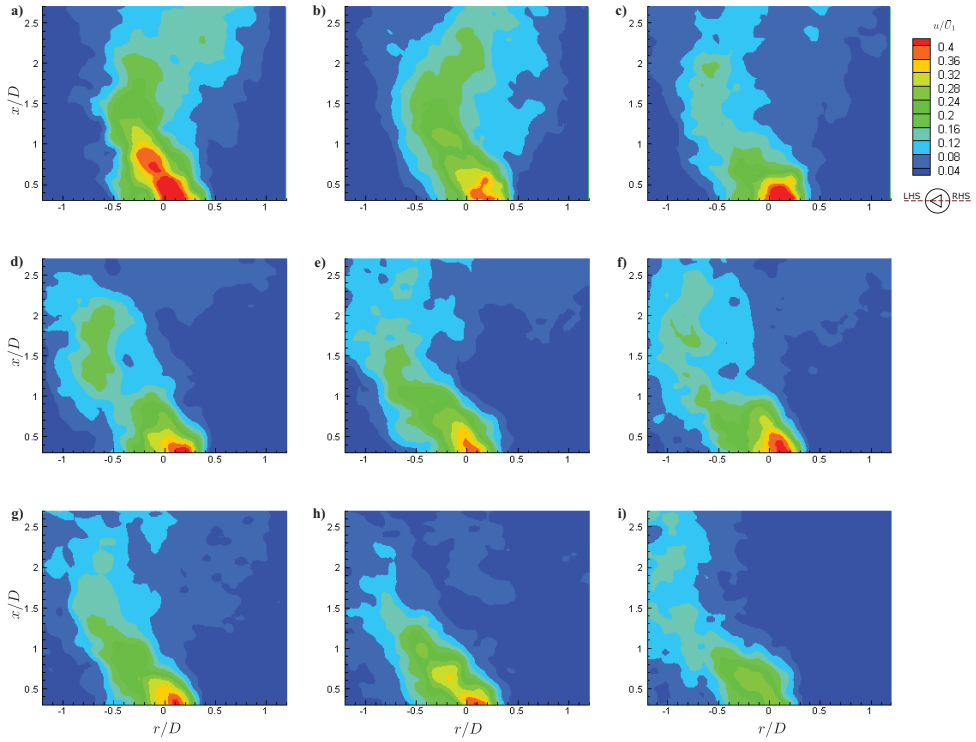

Figure 4.3: Axial velocity component of the conditionally averaged flow fields, $u/\bar{U}_1$, for density ratios, ρ_j/ρ_a = a) 0.2, b) 0.3, c) 0.45, d) 0.67, e) 1.0, f) 1.5, g) 2.24, h) 3.34 and i) 5.0.

curvature for a mechanically precessing jet. They also found that, as the Strouhal number of oscillation, St_{osc}, was increased, the curvature of the jet back to the nozzle axis was more pronounced. The Strouhal number of oscillation is defined in equation 4.1 where f_{osc} is the frequency of oscillation. The jet curvature was attributed to an increase in the strength of the low pressure core identified by Schneider et al (1993) and Schneider et al (1997) that precesses with the jet, and "pulls" it back towards the axis. The frequency of oscillation with respect to ρ_j/ρ_a is discussed later. Secondly the selection criterion for the conditional average is applied over the range $x/D < 1.5$, and, since the measurement is not directly conditioned on the phase of the oscillation, this may lead to greater variability in the location of the jet for $x/D > 1.5$.

$$St_{osc} = f_{osc} d_{e1} / \bar{U}_1 \tag{4.1}$$

To further assess the jet deflection, another approach was also adopted. This method, labelled the probability density analysis, is described in section 3.3.10.2. The result is shown in figure 4.4.

The angle θ determined from figure 4.4, as a function of ρ_j/ρ_a is shown in figure 4.5. This shows that the influence of ρ_j/ρ_a on θ can be separated into two distinct regions, $\rho_j/\rho_a < 1$ and $\rho_j/\rho_a > 1$. For $\rho_j/\rho_a < 1$, θ is found to depend strongly on ρ_j/ρ_a. This result is consistent with the half widths presented in figure 4.2 for this region. For $\rho_j/\rho_a > 1$, θ also exhibits a dependence on ρ_j/ρ_a but is much weaker. While the dependence of ρ_j/ρ_a on θ is weak in this region, it is still significant. It is also noted that the trends shown in figures 4.5 and 4.2b are similar in appearance, indicating that the initial jet spread is largely controlled by θ.

Figure 4.6a shows the axial variation in the jet mean centreline velocity, and 4.6b shows the mean velocity decay gradient for all ρ_j/ρ_a. Data are presented as an inverse velocity. The decay gradient, $\Delta(\bar{U}_1/U_c)/\Delta(x/D)$, is determined over the same range as the spread gradient (figure 4.2b). Comparison with figure 4.2 reveals a generally consistent trend for $\rho_j/\rho_a < 1$; that is, increasing spread corresponds to an increased decay gradient. However for $\rho_j/\rho_a > 1$ the gradient of decay continues to increase despite the gradient of spread shown in figure 4.2

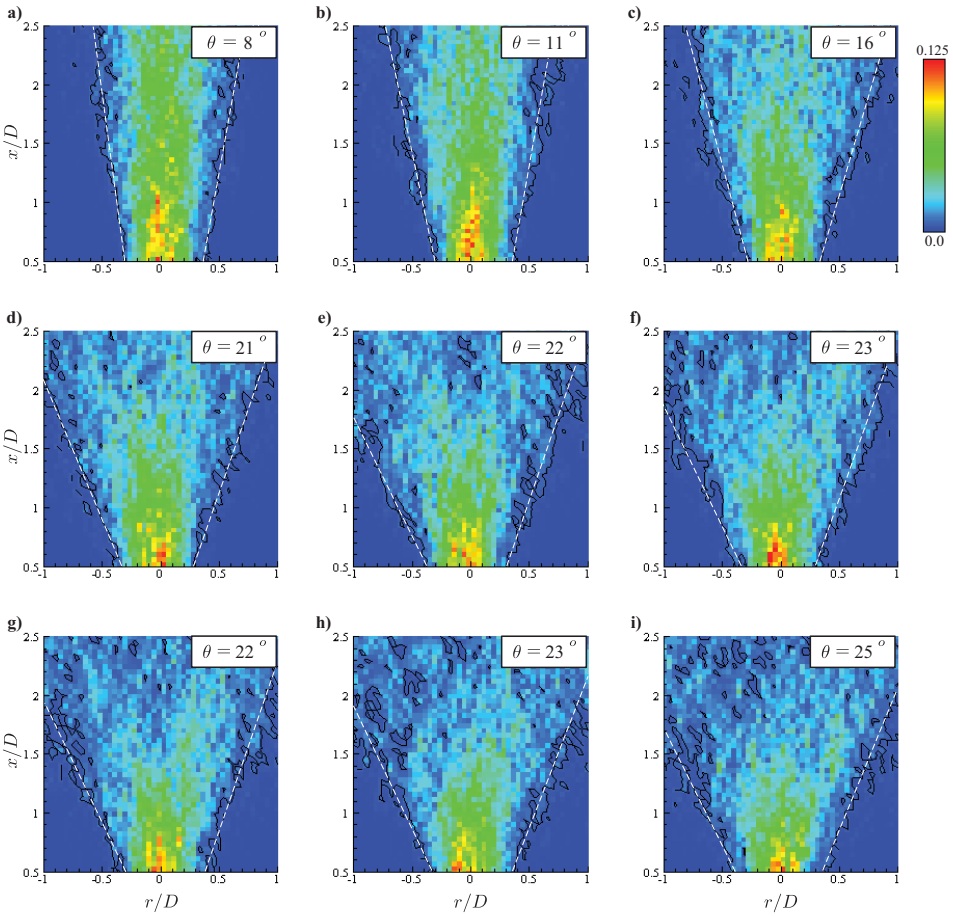

Figure 4.4: Probability density of maximum velocity magnitude for density ratios, ρ_j/ρ_a = a) 0.2, b) 0.3, c) 0.45, d) 0.67, e) 1.0, f) 1.5, g) 2.24, h) 3.34 and i) 5.0.

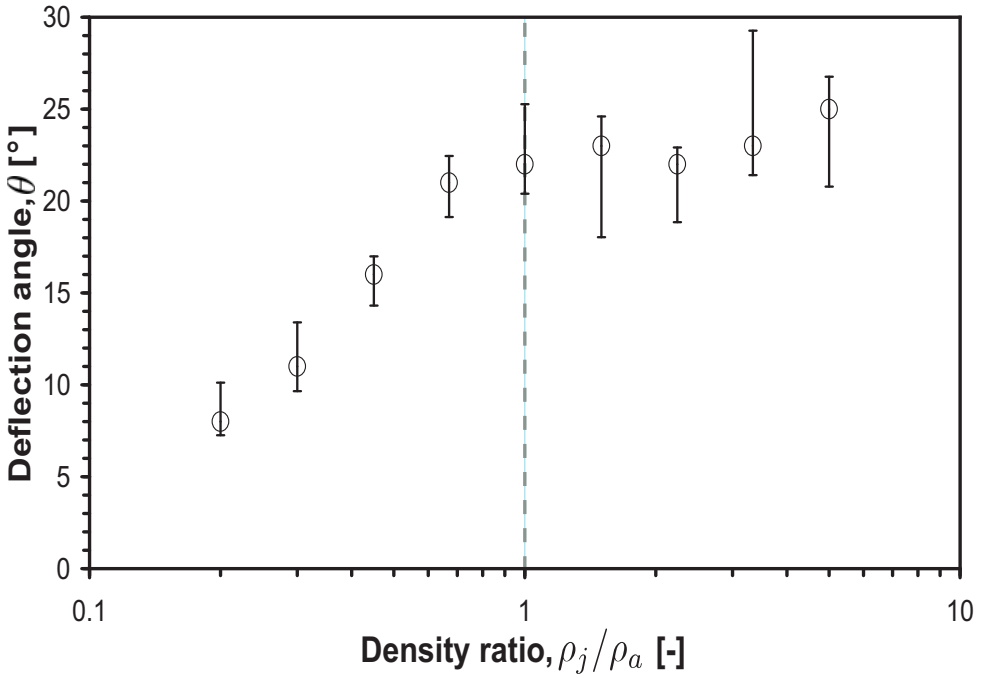

Figure 4.5: Deflection angle, θ of the instantaneous emerging jet as a function of density ratio, ρ_j/ρ_a, based on the pdf of maximum velocity magnitude (figure 4.4).

remaining relatively constant.

To understand this we will first consider the case where St_{osc} tends towards zero. Under this condition the jet emerges at a constant angle from one side of the nozzle and crosses the nozzle axis as a pseudo-steady jet. Without any force or pressure gradient to induce the jet back towards the nozzle axis, the jet's trajectory will continue to follow the initial deflection angle, θ. If then the jet is revolved around the nozzle axis, a focal point will result at the location where the jet crosses the nozzle axis. Downstream from this focal point the mean flow will appear to be conically divergent. The spread of the local jet will be affected by density gradients as described by Era and Saima (1977) and Richards and Pitts (1993). Increasing the angle of jet deflection and decreasing the gradient of the local jet spread will cause the focal point to occur closer to the nozzle exit and the conical divergence to become more pronounced. When the ρ_j/ρ_a is higher the gradient of spread for a steady deflected jet is lower. Combining this with the larger deflection angle shown for higher density ratios (Figure 4.5) indicates that conical divergence in the mean flow will occur sooner and be more significant

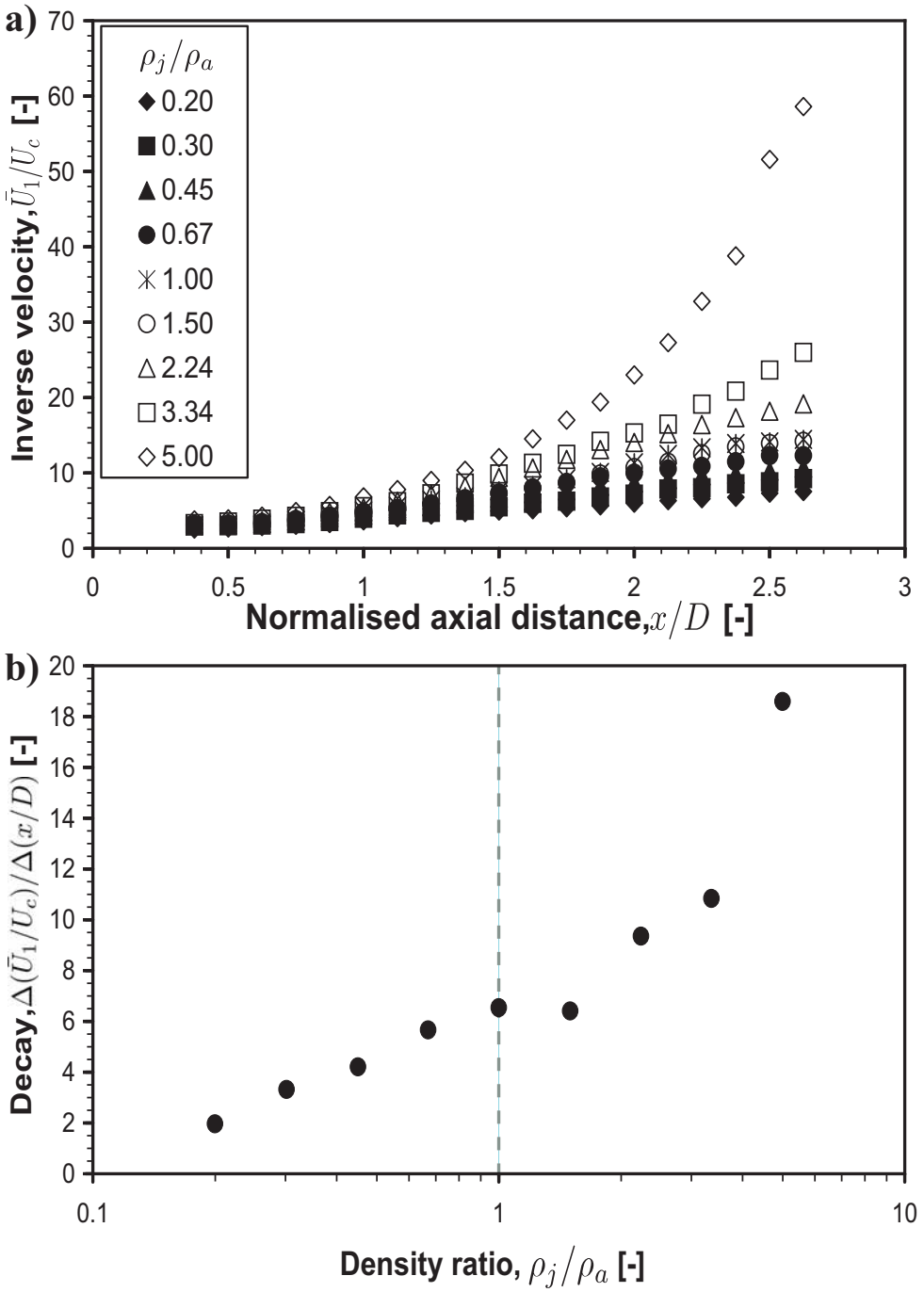

Figure 4.6: a) Centreline inverse velocity, and b) centreline decay gradient at various density ratios, ρ_j/ρ_a.

when ρ_j/ρ_a is higher.

Figure 4.7 shows for $\rho_j/\rho_a = 5$ the contour U_{70}, defined as the location where the local magnitude of velocity is greater than 70% of the maximum magnitude of velocity at that x/D. The appearance of a local maxima on either side of the nozzle axis can be clearly seen in figure 4.7, which is evidence of conical divergence in the mean flow. Further downstream from the initial point of the divergence the U_{70} contours move radially outwards, and will continue to do so unless there is a force acting to prevent this. This is consistent with a rapid increase in the velocity decay on the nozzle axis. The velocity decay along the nozzle axis can increase without a corresponding increase in mean spread, since the mean spread is controlled by the conical structure while the decay gradient is enhanced by an induced adverse pressure gradient along the nozzle axis. However the "conical" region on the nozzle axis downstream from the initial point of divergence induces a low pressure core as described above. The work of Mi and Nathan (2005) showed that once St_{osc} exceeds a critical value, the low pressure core acts to reduce the divergence of the mean flow.

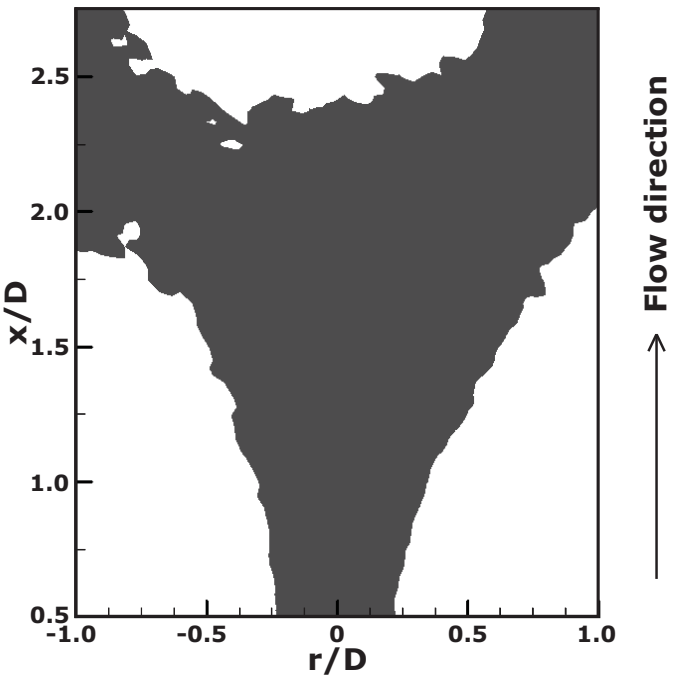

Figure 4.7: Bifurcation of the mean flow for $\rho_j/\rho_a = 5.0$

The value of St_{osc} was determined by measurement of the dominant frequency of oscillation, f_{osc}. Figure 4.8 shows the frequency power spectra for the TOJ at various ρ_j/ρ_a. This is the output from the first pressure vs time trace as determined using the Burg Maximum Entropy method. Although four pressure vs time traces were collected, there are no qualitative differences in the behaviour, and this result is typical of all four pressure traces. Figure 4.8 clearly shows that, as ρ_j/ρ_a is increased, f_{osc} decreases. The trend of decreased values of f_{osc} at increased values ρ_j/ρ_a is highlighted in figure 4.9, where f_{osc} is presented as a function of ρ_j/ρ_a.

Figure 4.10 presents St_{osc} as a function of ρ_j/ρ_a. This shows that for $\rho_j/\rho_a \leq 1.0$, St_{osc} is relatively insensitive to density ratio, with a value of approximately 0.005. Increasing ρ_j/ρ_a above unity results in a rapid drop in the value of St_{osc}. For $\rho_j/\rho_a \geq 2.24$ the St_{osc} is again relatively independent of density ratio with a value an order of magnitude lower. For the case $\rho_j/\rho_a \leq 1.0$ the Strouhal number is expected to be in the supercritical regime identified by Mi and Nathan (2005), i.e. to be in the regime where the low pressure core is significant. In contrast, for $\rho_j/\rho_a \geq 2.24$ the Strouhal number is expected to be subcritical, i.e. without a significant low pressure core.

From figure 4.8, it is also evident that there are usually several significant peaks in each spectrum. This indicates that, while the jet may oscillate with a dominant frequency, there is significant cycle-to-cycle variation in the oscillation period. Cycle-to-cycle variation has been observed previously for TOJ and Fluidic Precessing Jet flows (Lee et al, 2003; Hill et al, 1992; Wong et al, 2002) and is attributed to the amplification of small asymmetries in the instantaneous flow. For the TOJ flow, Lee et al (2003) found the internal jet to have three preferred locations of re-attachment inside the chamber that are aligned with the sides of the triangular orifice. The oscillation was also observed to be a 3-D "flapping motion" between these three azimuthal locations rather than a smooth precession (Lee et al, 2003). Three factors then can characterise variability in f_{osc}. The first is the variation in the time that the jet holds at one of the three preferred locations (H), the second is the variability in the time taken to move between two adjacent locations (M) and the third is the probability with which direction the oscillation moves with respect to the previous movement direction (P). The

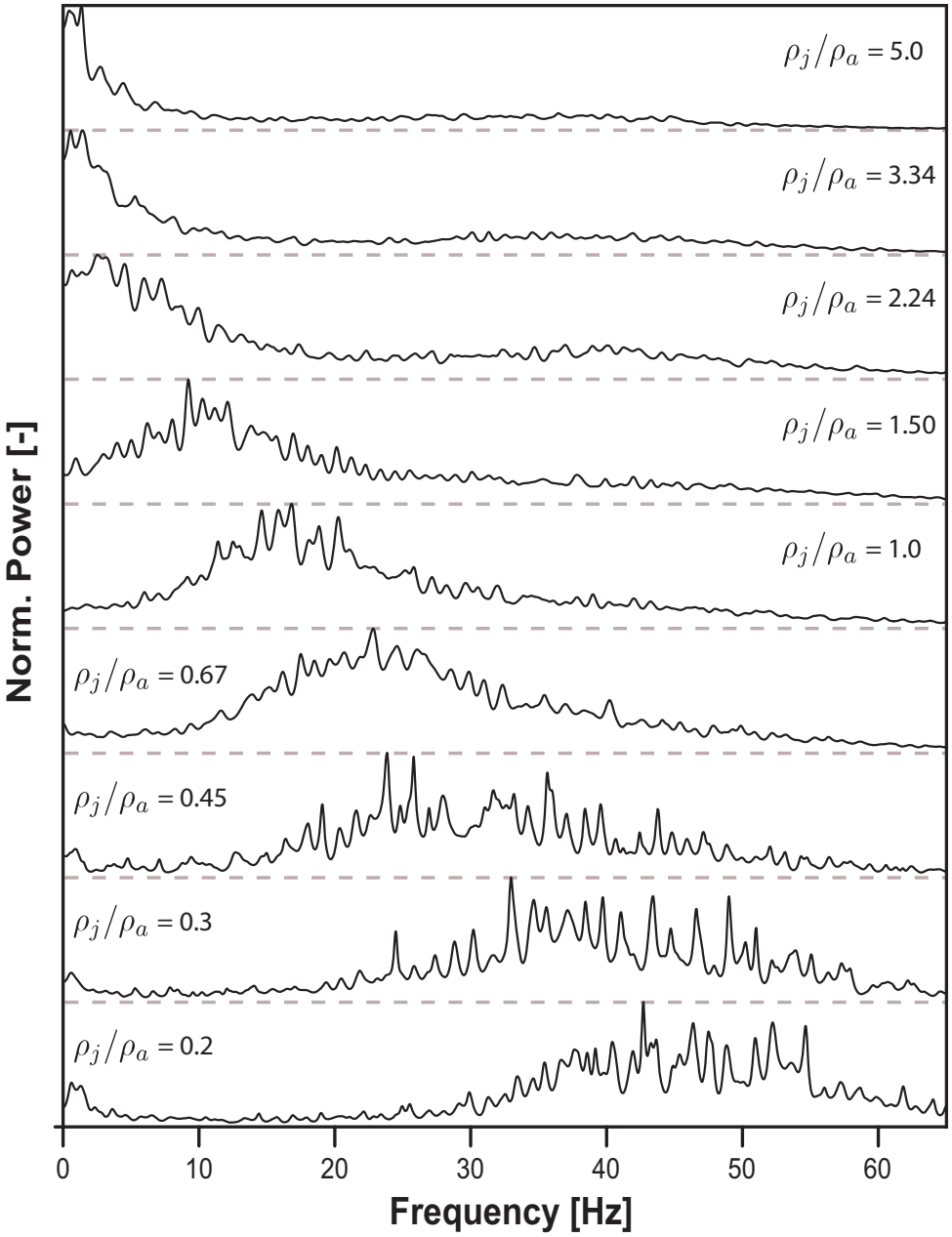

Figure 4.8: Frequency power spectra for all density ratios, ρ_j/ρ_a.

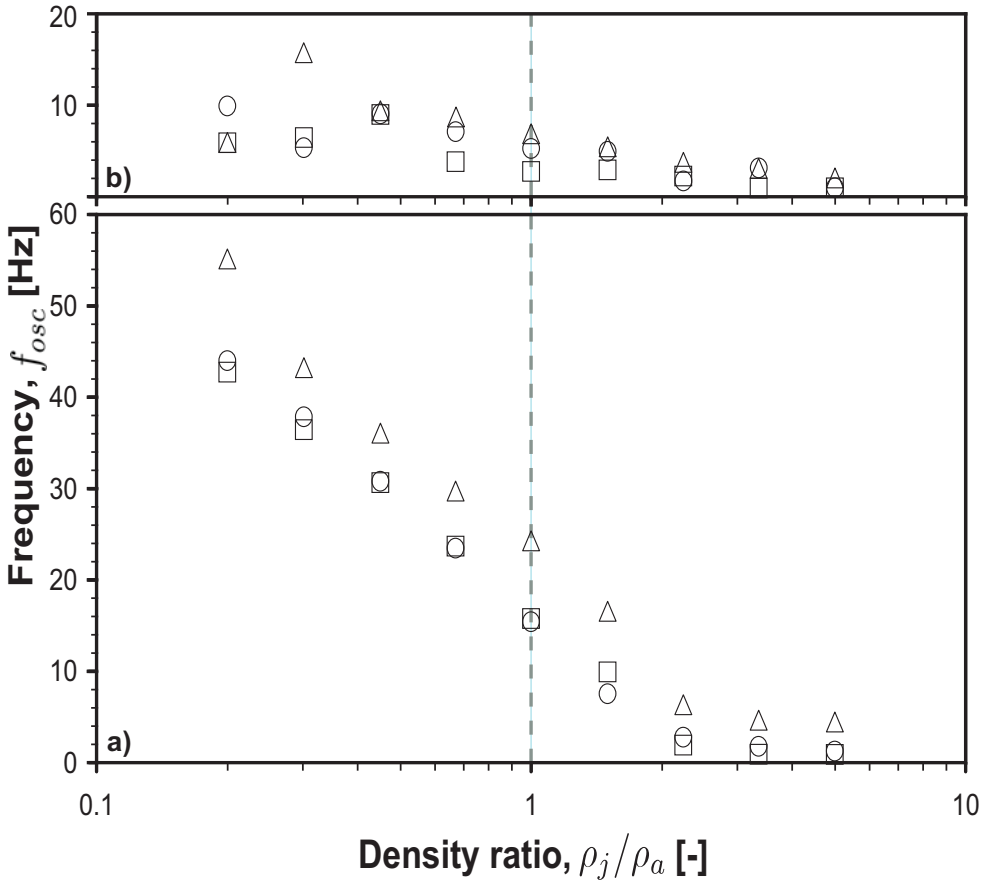

Figure 4.9: a) Oscillation frequency, f_{osc}, as a function of density ratio, ρ_j/ρ_a, b) Measurement uncertainty. (Circles = FFT, Squares = Burg-MEM, Triangles = Peak counting)

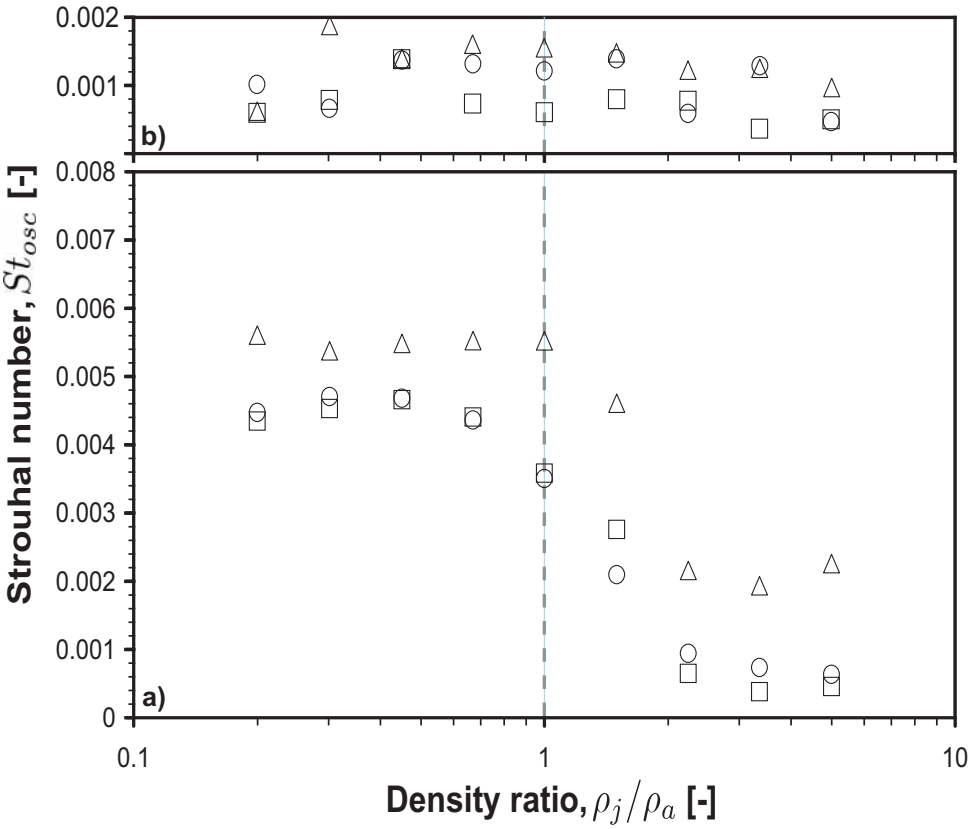

Figure 4.10: a) Jet Strouhal number, St_{osc}, as a function of density ratio, ρ_j/ρ_a, b) Measurement uncertainty. (Circles = FFT, Squares = Burg-MEM, Triangles = Peak counting)

period of oscillation can then be described by equation 4.2 where z is a function of P and has an integer value greater than or equal to 2.

$$Period = z(H + M); \quad z = f(P) \tag{4.2}$$

To give insight into the character of the oscillation, a probabilistic simulation based on equation 4.2 was conducted using an algorithm written in MatLab. Simulated data traces were produced based on systematic variations in H and M about likely values using a random number generator to determine the movement direction based on the value of P. The response as recorded by an equivalently placed probe was then simulated and a pseudo frequency spectrum calculated for a data set of 40,000 points. Results of the simulation are shown in figure 4.11. With the values used for the parameters H and M, and setting the time associated with each data point equal 1/1000th of a second, a frequency of 9.25 Hz should be expected.

Figure 4.11 compares six calculated spectra with one measured spectrum. It is reiterated that these are not an a-priori simulation of the flow, but rather illustrate that the real spectrum (4.11g) can be closely approximated by a series of random combinations of move and hold events with significant probability of oscillation direction changes (4.11e and f). The other cases shown in figure 4.11 are: a) true periodic oscillation with no direction changes (P=1) or variance, b) and c) increasing the probability of direction changes with zero variance, and d) no direction changes but variation in the hold time. In the examples shown M has been held constant. Allowing variance of this term has the same effect as variance of H. Therefore, figure 4.11 provides further evidence that the jet's azimuthal motion may be a random flapping between three preferred locations of attachment, with significant variation in either or both of the "move" and "hold" times of these motions.

If, as is suggested by figure 4.11, the jet's oscillation is characterised by a random flapping motion rather than a true precession, the formation of a strong low pressure core, even when the Strouhal number is high, is unlikely. This means that the suppression of flow divergence like that found by Mi and Nathan (2005) for a mechanically precessing jet will be small. Therefore the initial location of

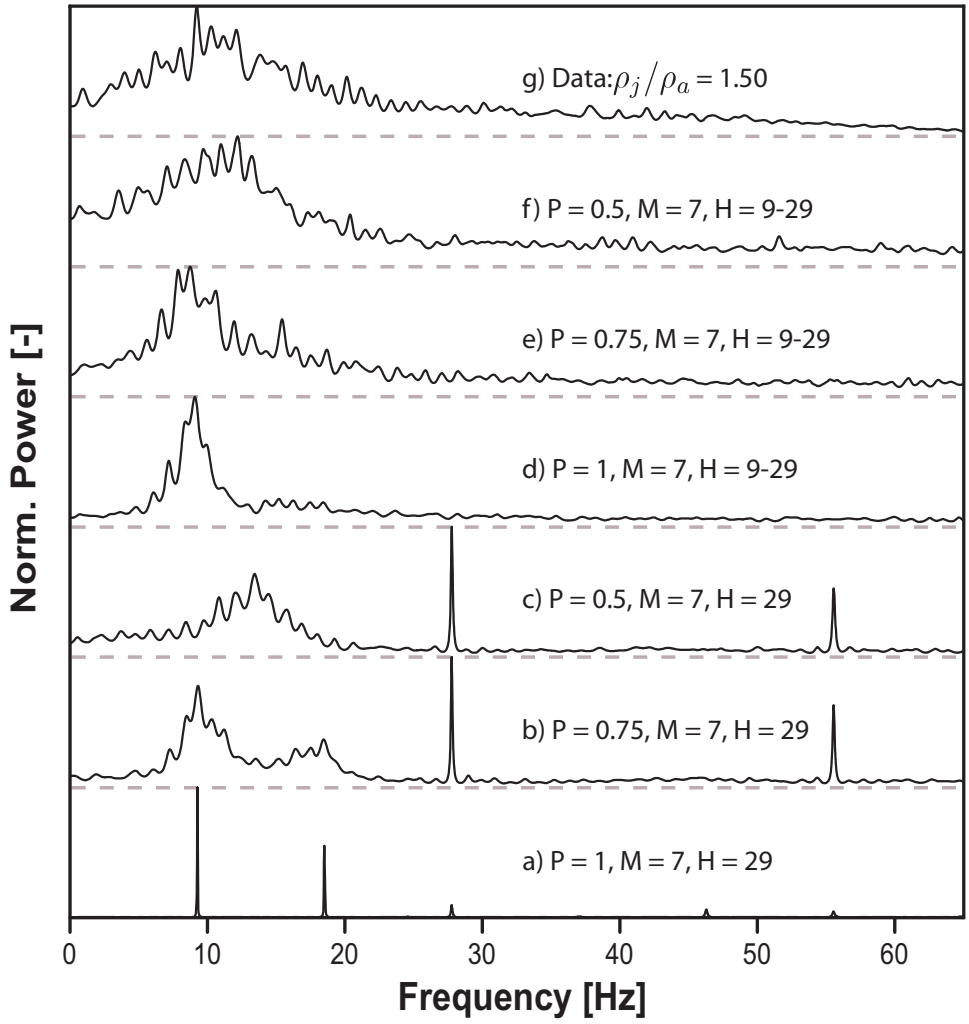

Figure 4.11: Frequency spectra calculated from a probabilistic simulation.

any flow divergence, and the influence this has on the centreline decay gradient, will only be affected by the instantaneous jet deflection angle, and the rate of spread from this deflected jet.

4.3 Conclusions

Velocity measurements by PIV and pressure measurements of the oscillation frequency have been used to investigate the flow from a TOJ nozzle under variable density conditions. Half-widths calculated from the PIV data show that when the density of the jet fluid is greater than the ambient, the effect of density on the mean jet spread is small. However when the jet fluid is less dense than the ambient the mean spread of the jet is significantly reduced. A similar trend is seen for the instantaneous jet deflection angle. Hence these two trends are consistent with each other.

The inverse centreline decay rate, also calculated from the PIV data, shows that, as the density of the jet fluid is increased with respect to the ambient, the centreline decay rate is also increased. This result is consistent with the measurements of the half width, which increases with the decay rate. However at high jet-fluid densities, the decay rapidly increases despite causing little influence on the mean spread. This is due to the mean flow becoming conically divergent as a result of the high instantaneous jet-deflection angle. The trends are not consistent with a significant low pressure core.

Oscillation frequency measurements show that increasing the density of the jet fluid leads to a reduction in the dominant frequency of oscillation. Converting the oscillation frequencies into an oscillation Strouhal number, revealed two distinct regimes. The regime in which the jet fluid density is less than or equal to the ambient has a Strouhal number sufficiently high at $St_{osc} \approx 0.005$ to produce a low pressure core. However for $\rho_j/\rho_a > 1$ it was observed that St_{osc} decreases by an order of magnitude, which is unlikely to produce a low pressure core. Further, the probabilistic frequency simulations have shown the frequency spectra are most likely the result of a random 3-D "flapping" rather than a regular oscillation. This suggests that the formation of a strong low pressure core to counteract mean flow divergence is unlikely even if the Strouhal number of oscillation is high.

High spread and decay produced by the oscillating flow were previously associated with beneficial performance in some industrial applications. On this basis, if the jet fluid is of lower density than the ambient, then the nozzle performance will be sensitive to operating temperature changes. However the sensitivity to operating

temperature changes should be low if the jet fluid density is greater than or equal to the ambient, provided that near-field flow divergence does not impact adversely on nozzle performance. Given that practical designs are expected to introduce colder, more dense air via the nozzle into hot, less dense products and air, this finding is particularly relevant.

Chapter 5

Variable Density TOJ with Variable L/D

5.1 Introduction

Chapter 4 investigated the effect of density ratio on the TOJ flow from a fixed nozzle geometry, motivated by the fact that kiln operating temperatures and gas compositions in a cement kiln can vary significantly. However depending on it's capacity and the process, the physical dimensions of a kiln can also vary significantly. This means that, while the spread achieved by the nozzle in one kiln may be suitable, the same spread in another kiln may lead to flame impingement onto the refractory walls leading to reduced refractory life. Therefore, to help optimise the nozzle for each application it is important to understand the influence of changing the chamber length at various fixed density ratios. To meet this need, therefore, the aim of the present chapter is to investigate, at five different density ratios, the effect of changing the chamber length on the near field of the emerging flow from a TOJ nozzle.

The parameters used in the investigation are as follows. As described in section 3.3.2 the jet fluid is introduced through the nozzle with a momentum flux of 0.06 kgms^{-2}. The bulk mean velocity and Reynolds number for each case at this momentum flux are shown in table 4.1. The nozzle chamber length parameter, L/D, was varied between 2.02 and 2.96. This matrix of configurations was selected on

$\rho_j/\rho_a \setminus L/D$	2.02	2.11	2.21	2.30	2.40	2.49	2.58	2.68	2.77	2.87	2.96
0.20	X	X	X	X	X	X	X				
0.45		X	X	X	X	X	X	X			
1.00			X	X	X	X	X	X	X		
2.24				X	X	X	X	X	X	X	
5.00					X	X	X	X	X	X	X

Table 5.1: Chamber lengths investigated for variable density TOJ.

the basis of preliminary investigations that showed that lower density ratios perform better with shorter chamber lengths. Table 5.1 shows the chamber lengths investigated at each density ratio. All other nozzle dimensions are as described in section 3.2. The density ratios investigated are 0.2, 0.45, 1.0, 2.24 and 5.0, covering the range of density ratios investigated in chapter 4.

5.2 Background

Nathan (1988) investigated the effect of changing L/D for the FPJ nozzle and found that an increase in L/D above the minimum required for precession resulted in an increase in the jet spread. However continuing to increase L/D yields a critical L/D, beyond which any further increases in L/D result in a decrease in the jet spread. It has been shown in chapter 4 that mean jet spread is closely linked with instantaneous jet deflection angle, θ. Since surrounding fluid is continually drawn into the chamber and entrained into the jet, some mixing has taken place prior to the jet leaving the nozzle. Therefore an increase in L/D at lengths shorter than the critical L/D increases the length in which internal mixing can occur, and hence more internal spread. Increasing the internal spread leads to greater interaction with the exit lip resulting in larger deflection, θ. However, while increasing L/D beyond the critical L/D will increase internal mixing further, the associated extra internal spread causes the flow within the chamber to approach that of developed pipe flow, with the external jet tending to that which is observed for a simple axial jet.

Lee et al (2003) previously showed that for $\rho_j/\rho_a = 1.0$ the critical L/D is 2.50. When the nozzle operates at non-unity ρ_j/ρ_a, any spread within the nozzle cham-

ber will be affected by ρ_j/ρ_a. Since a lower density fluid discharging into a denser fluid spreads more rapidly (Richards and Pitts, 1993) it is expected that for a fixed L/D more internal spread will occur when ρ_j/ρ_a is smaller. Therefore it is expected that the critical L/D will be shorter when $\rho_j/\rho_a < 1.0$ and longer when $\rho_j/\rho_a > 1.0$.

5.3 Results and Discussion

Figures 5.1, 5.2 and 5.3 present the axial velocity component of the ensemble averaged flow fields, $u/\bar{U}_1$, for density ratios of $\rho_j/\rho_a = 0.2$, 1.0 and 5.0 respectively at various chamber lengths, L/D. Here the axial component, u, of the velocity is normalised by the bulk mean orifice velocity $\bar{U}_1$. From these figures it can be seen that, as ρ_j/ρ_a is increased, the contour envelope becomes shorter and broader, as was the case in chapter 4. The contour envelope also appears to become shorter and broader as L/D is increased at fixed ρ_j/ρ_a except for ρ_j/ρ_a=0.2, where no obvious difference is observed. The figures for $\rho_j/\rho_a = 0.45$ and 2.24 show similar trends and are presented in appendix A. There is no evidence of an obvious peak in the spreading. That is, the critical L/D cannot be clearly identified from figures 5.1, 5.2, and 5.3.

Figures 5.4, 5.5, and 5.6 show the normalised mean half widths, $\bar{r}_{1/2}/D$, over the L/D range for $\rho_j/\rho_a = 0.2$, 1.0 and 5.0 respectively. The half widths for $\rho_j/\rho_a = 0.45$ and 2.24 can be found in appendix A. Figure 5.7 shows the gradient of spread, $\Delta\bar{r}_{1/2}/\Delta x$, calculated from the half widths over the range $x/D = 1.25$ - 2.0. Due to a lack of half width data in some cases the gradient calculated over the mentioned range was based on three or fewer data points. Caution is required to avoid drawing conclusion from these cases, and they are therefore not presented in figure 5.7.

For $\rho_j/\rho_a = 0.2$ the results of the half widths and spread gradient show that a change in the chamber length over the L/D range 2.02 - 2.58 has no significant effect on the mean spread of the flow. At the other density ratios a change in the chamber length does result in a change in the mean spread of the TOJ flow. Based solely on the half widths, over the L/D range investigated, an increase

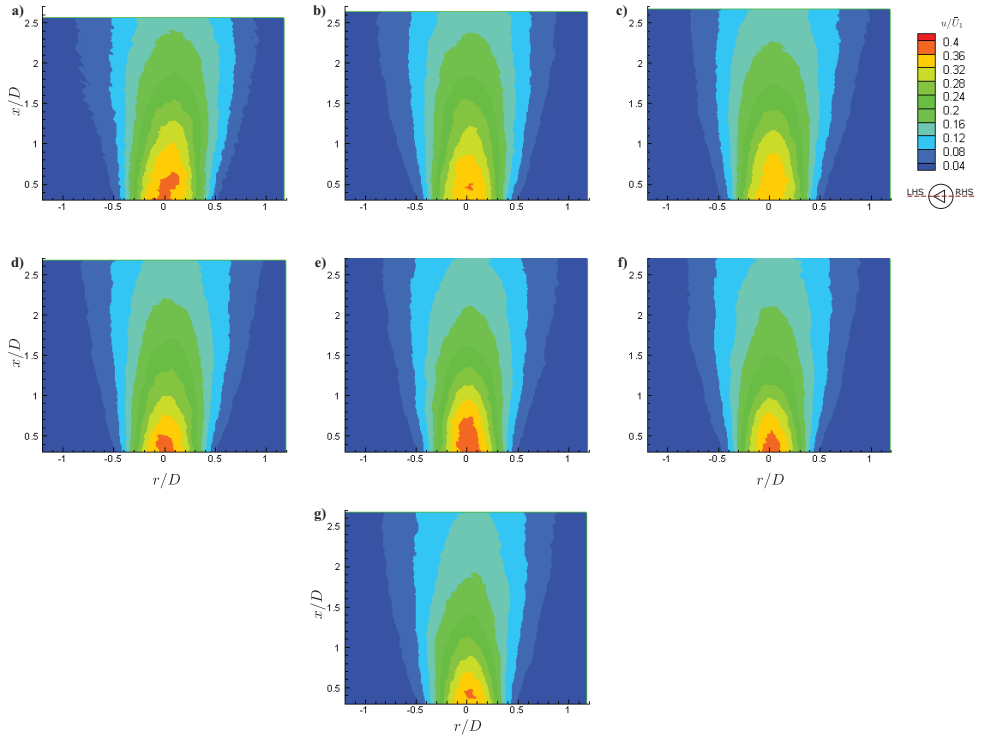

Figure 5.1: Axial velocity component of the ensemble averaged flow fields, $u/\bar{U}_1$, with density ratio, $\rho_j/\rho_a = 0.2$, for L/D = a) 2.02, b) 2.11, c) 2.21, d) 2.30, e) 2.40, f) 2.49 and g)2.58.

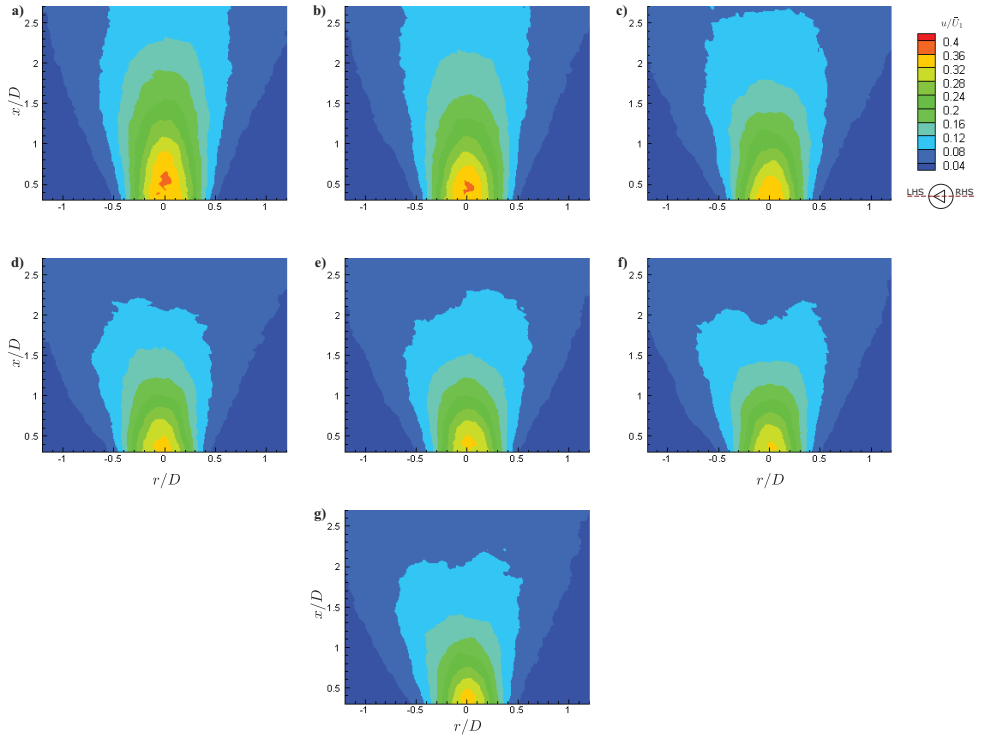

Figure 5.2: Axial velocity component of the ensemble averaged flow fields, $u/\bar{U}_1$, with density ratio, $\rho_j/\rho_a = 1.0$, for L/D = a) 2.21, b) 2.30, c) 2.40, d) 2.49, e) 2.58, f) 2.68 and g)2.77.

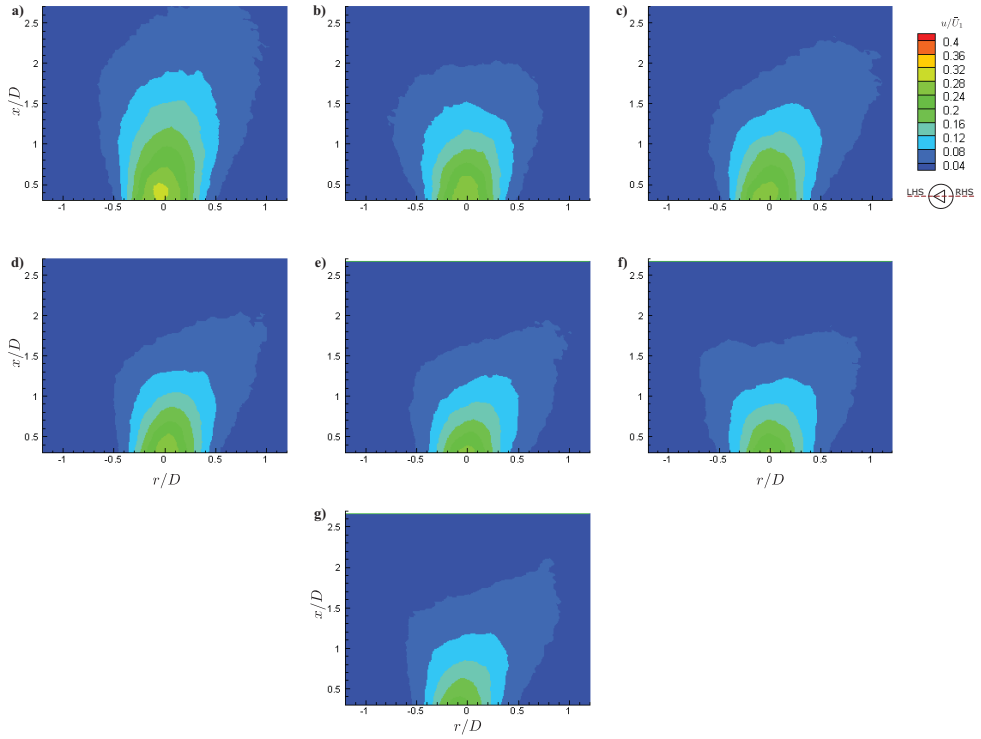

Figure 5.3: Axial velocity component of the ensemble averaged flow fields, $u/\bar{U}_1$, with density ratio, $\rho_j/\rho_a = 5.0$, for $L/D =$ a) 2.40, b) 2.49, c) 2.58, d) 2.68, e) 2.77, f) 2.87 and g)2.96.

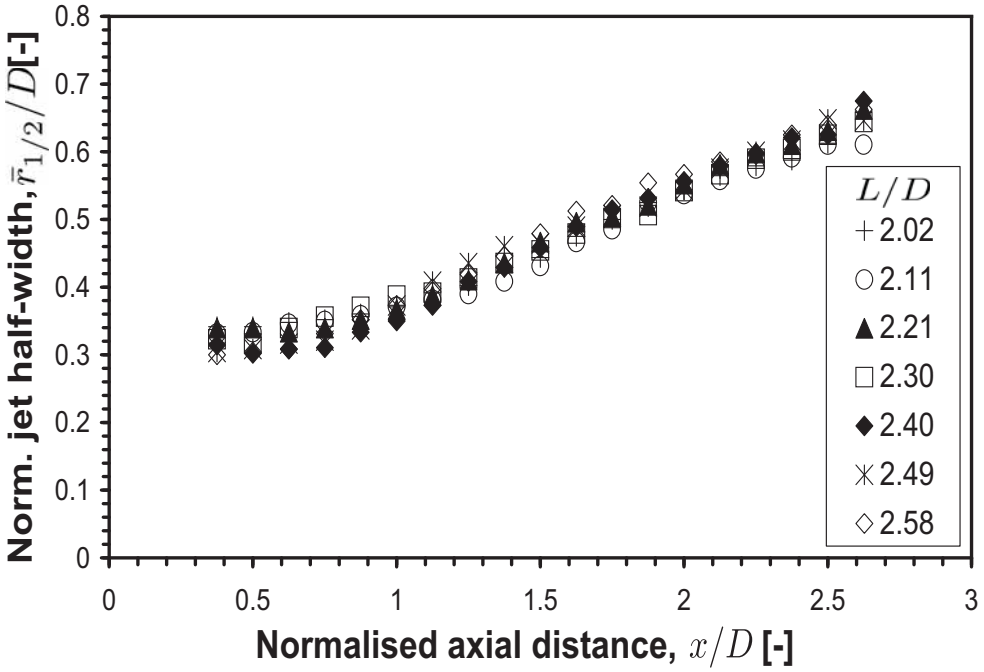

Figure 5.4: Mean half widths for the TOJ nozzle at various L/D for $\rho_j/\rho_a = 0.2$.

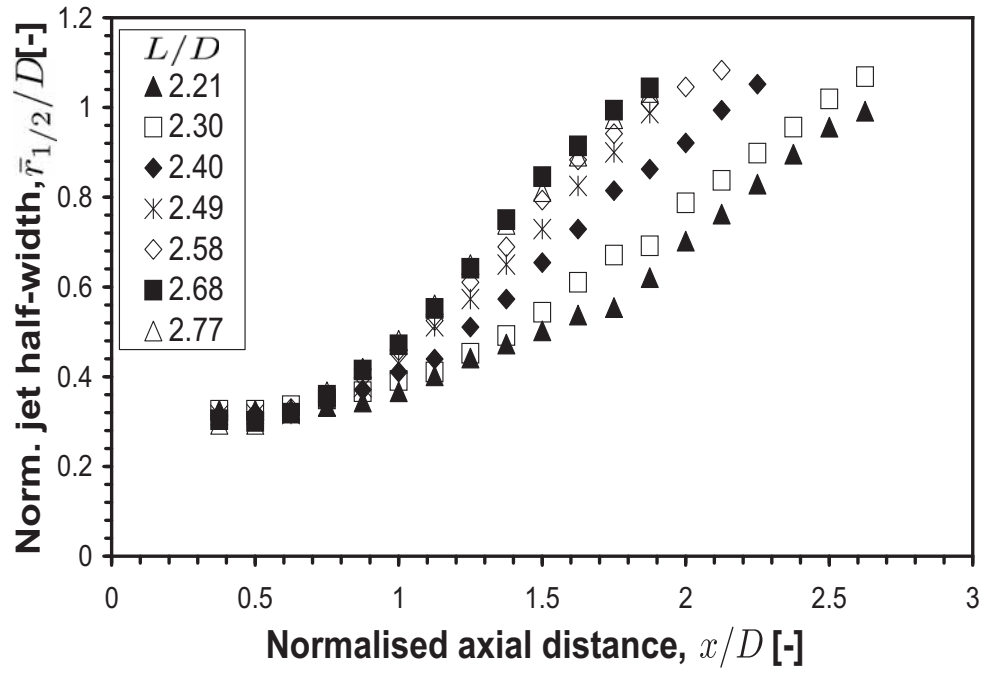

Figure 5.5: Mean half widths for the TOJ nozzle at various L/D for $\rho_j/\rho_a = 1.0$.

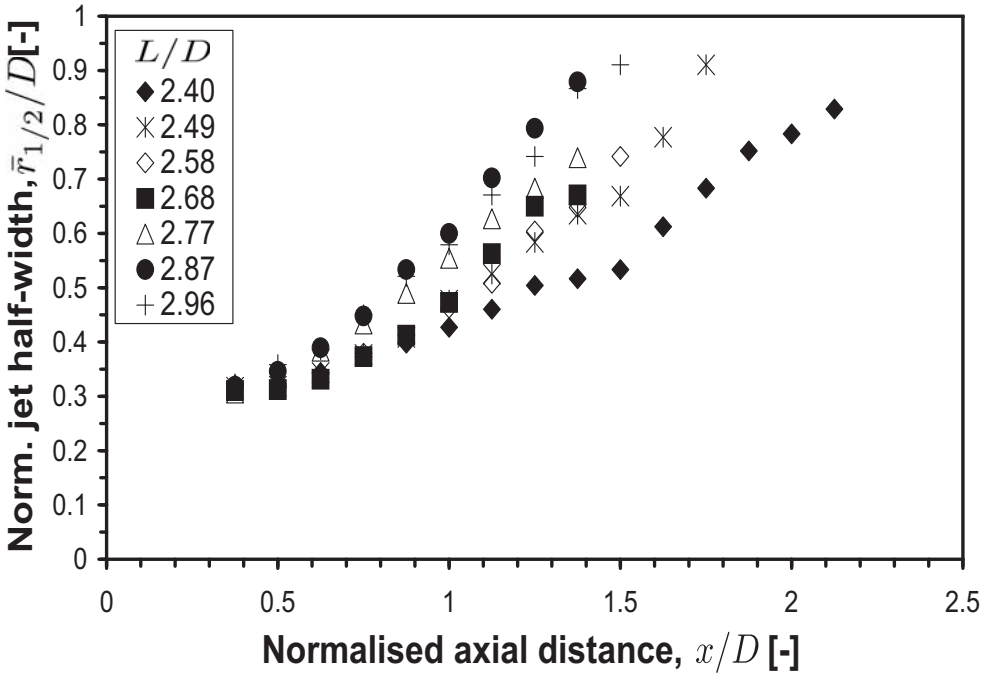

Figure 5.6: Mean half widths for the TOJ nozzle at various L/D for $\rho_j/\rho_a = 5.0$.

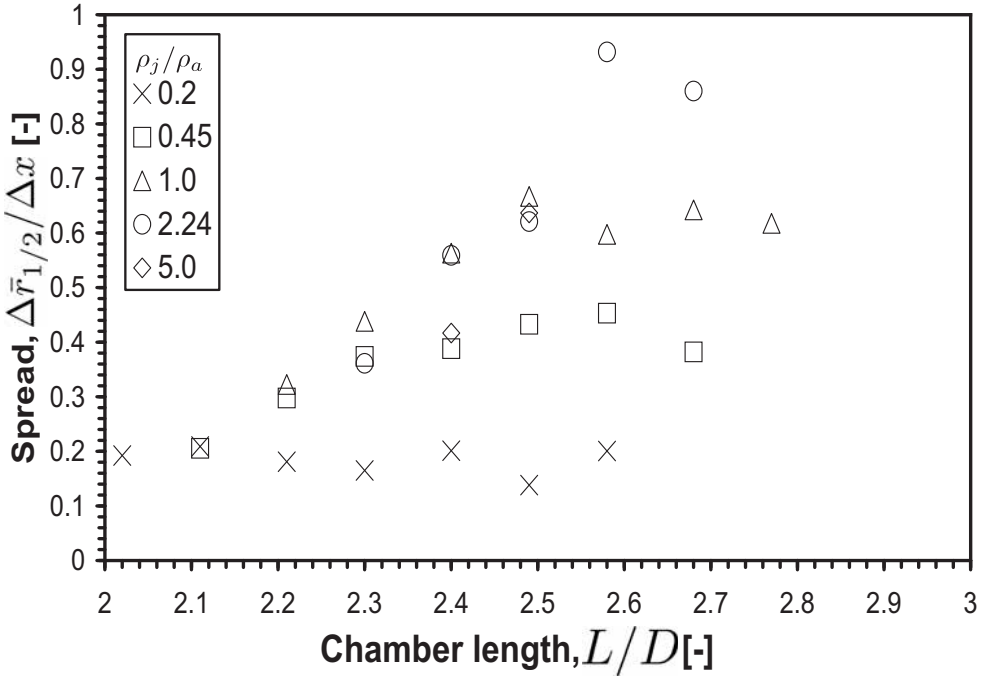

Figure 5.7: Gradient of spread as a function of L/D at $\rho_j/\rho_a = 0.2$, 0.45, 1.0, 2.24 and 5.0.

in the chamber length results in an increase in the mean spread, although the relative change becomes smaller with a longer chamber. This would suggest that for each ρ_j/ρ_a investigated, the critical L/D, if it exists, is either at a chamber length longer than those investigated, or it can be considered to be a narrow range rather than a single discrete L/D. Lee et al (2003) measured the critical L/D for $\rho_j/\rho_a = 1.0$ to be $L/D = 2.50$. The data presented here for $\rho_j/\rho_a = 1.0$ does not show a clear peak to confirm that finding.

It is important to note that Lee et al (2003) did not measure the mean spread but rather the jet deflection angle, θ. To qualitatively assess θ the PIV data were conditionally averaged. Since the conditional average is only qualitative, due to the small sample size, which in some cases was zero, the conditional averages are not presented here. However they can be seen in appendix A. Quantitative assessment of θ was conducted using the probability density analysis (section 3.3.10.2). Figures 5.8, 5.9 and 5.10 show the results for $\rho_j/\rho_a = 0.2$, 1.0 and 5.0 respectively. The figures for $\rho_j/\rho_a = 0.45$ and 2.24 can be found in appendix A. The jet deflection angle, θ, as determined from these figures, is presented as a function of L/D for each ρ_j/ρ_a in figure 5.11. Also shown in figure 5.11 is the data of Lee et al (2003).

The current investigation was based on the findings of Lee et al (2003), being the only available and relevant data. As such, their data will be examined first. To measure the deflection angle, θ, they attached a silk streamer to the centre of the nozzle exit. Long exposure photographs of the streamer's motion were taken, and from these an angle was measured by hand. It is clear from figure 5.11 that Lee et al (2003) show a critical L/D for $\rho_j/\rho_a = 1.0$ at $L/D = 2.50$. However, between $L/D = 2.25$ and 2.75 the relative difference in the measured deflection angle is small. Coupled with the large separation in L/D between data points, it is quite possible that the critical L/D is not at 2.50. The small difference in the measured deflection angle over this L/D range also suggests that the critical L/D could more accurately be described as a small range rather than a discrete point. It is also important to note that the data of Lee et al (2003), which does extend outside the bounds presented in figure 5.11, is fitted accurately with a fifth order polynomial curve fit. Considering the measurement technique used, and the fact that no error margin is presented, the accuracy with which the curve

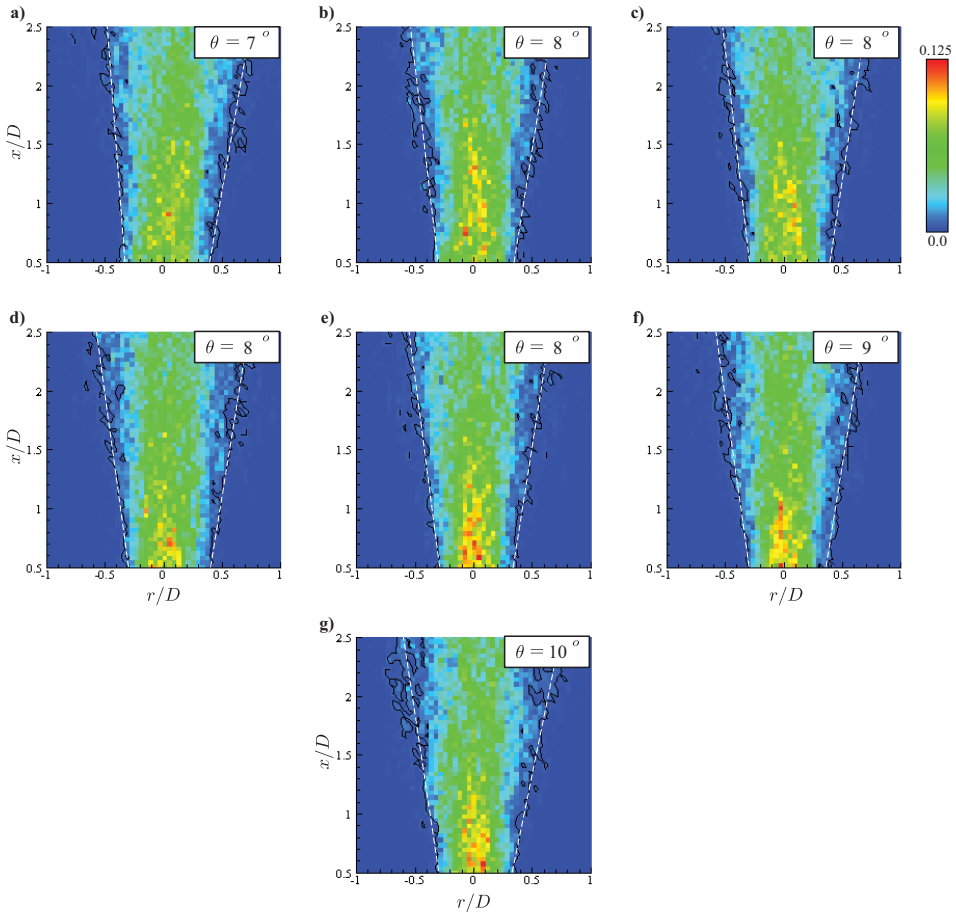

Figure 5.8: Probability density of maximum velocity magnitude for $\rho_j/\rho_a = 0.2$ and $L/D =$ a) 2.02, b) 2.11, c) 2.21, d) 2.30, e) 2.40, f) 2.49 and g)2.58.

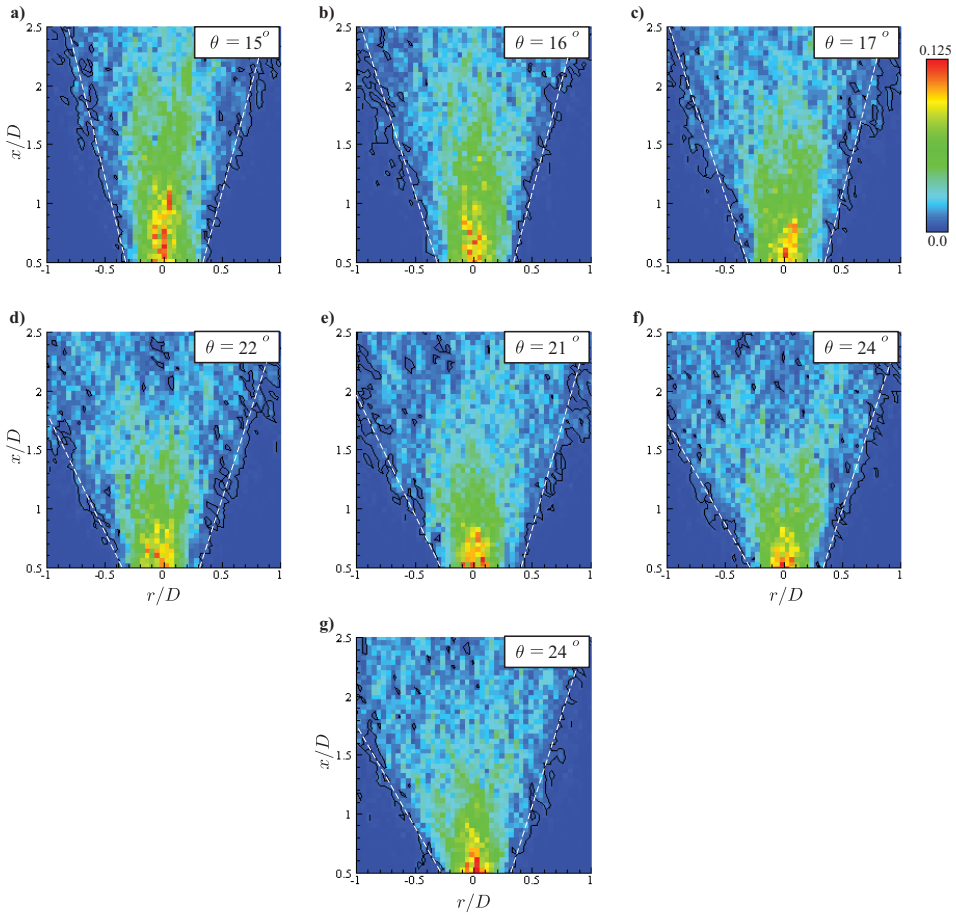

Figure 5.9: Probability density of maximum velocity magnitude for $\rho_j/\rho_a = 1.0$ and $L/D =$ a) 2.21, b) 2.30, c) 2.40, d) 2.49, e) 2.58, f) 2.68 and g)2.77.

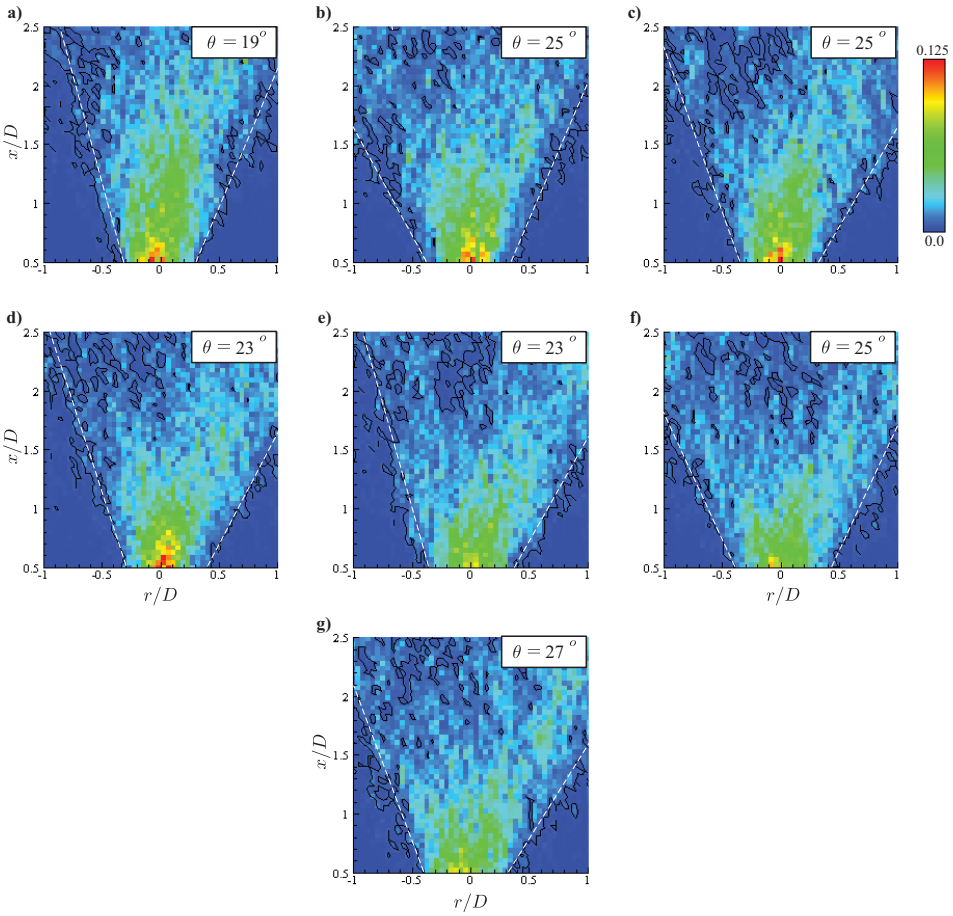

Figure 5.10: Probability density of maximum velocity magnitude for $\rho_j/\rho_a = 5.0$ and $L/D =$ a) 2.40, b) 2.49, c) 2.58, d) 2.68, e) 2.77, f) 2.87 and g)2.96.

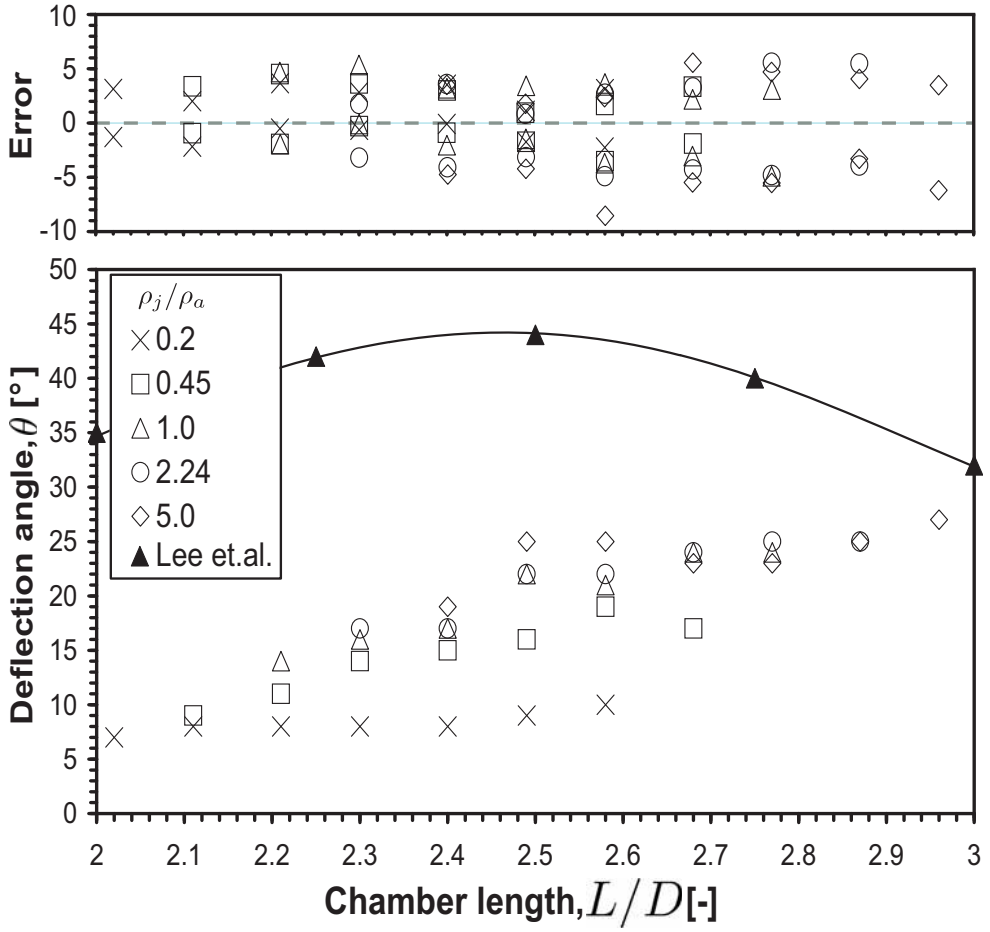

Figure 5.11: Deflection angle, θ, of the instantaneous emerging jet as a function of L/D with $\rho_j/\rho_a = 0.2$, 0.45, 1.0, 2.24 and 5.0.

fits the data casts some suspicion over the data's validity.

The experimental matrix selected the investigated L/D range for $\rho_j/\rho_a = 1.0$ to be centered around the critical L/D as determined by Lee et al (2003). Comparing their data with the new data for $\rho_j/\rho_a = 1.0$ reveals two key issues. The first is the absolute difference in the measured angle between the different data sets, and the second is that the finer experimental grid used here does not confirm the location of the critical L/D as measured by Lee et al (2003).

The absolute difference between the measured angle for the new data and that of Lee et al (2003) when $\rho_j/\rho_a = 1.0$ can be explained by the experimental differences. The first difference is the measurement technique. The technique used here directly measures the location of the maximum velocity magnitude throughout the image plane, so it can be considered reliable. Lee et al (2003) infer jet deflection from a single streamer that is tied to the centre of the nozzle exit. In regions of high velocity gradient, such as are found at the nozzle exit, this could easily lead to an increase in the measured angle. Their measurement also relies on the streamer accurately following the flow along the streamer's entire length. The frequency response of the streamer is unknown but it is certainly possible that this also leads to an increase in the measured angle. Other differences that could account for the large difference in the measured angle between the data sets are the Reynolds number and the geometric parameter d_2/D, which were 50000 and 0.9 for Lee et al (2003) and 17900 and 0.82 here.

More interesting than the absolute difference in the measured angle is the geometry providing maximum jet deflection, and hence spread, termed the critical L/D. The data of Lee et al (2003) show the critical L/D to be at $L/D = 2.50$. However, despite the present data spanning the range in which the data of Lee et al (2003) plateaus, the new data do not reach a peak. Over this range the new data continue to show a slight increase in the jet deflection angle. There must be a critical L/D as at large L/D the flow must approach that of a simple axisymmetric pipe jet. The present data therefore suggest that this critical L/D could be at $L/D \geq 2.77$. The issue is further clouded by the difference in the parameter d_2/D between the two data sets. One would expect that, when d_2/D is smaller, the location of the critical L/D should also be smaller. Comparison of the data sets does not show this. The issues arising from the comparison of

these two independent data sets suggest that further measurements are required to clarify the situation, and should therefore be the focus of future work.

Despite the above mentioned issues, examination of the data for variable density at various L/D, (figure 5.11) along with the half widths (figures 5.4, 5.5 and 5.6) and the spread gradient (figure 5.7), again it can be seen that θ is closely linked with the mean spread from the TOJ nozzle, indicating the data are internally consistent. As is the case for $\rho_j/\rho_a = 1.0$, figure 5.11 does not reveal a critical L/D over the range of L/D and ρ_j/ρ_a investigated. To determine the location of the critical L/D at each ρ_j/ρ_a, further measurements are required. These measurements should therefore also be the focus of future work.

While the critical L/D at each ρ_j/ρ_a is not revealed by this data, other relevant information can be gained. Neglecting the case where $\rho_j/\rho_a = 0.2$, since it appears to be a fundamentally different case, centered around $L/D = 2.58$ is a region for which the deflection angle, θ, is insensitive to a change in ρ_j/ρ_a. This insensitivity to ρ_j/ρ_a at a fixed L/D becomes even more apparent for $\rho_j/\rho_a \geq 1.0$. In fact for each L/D where all three $\rho_j/\rho_a \geq 1.0$ are investigated, the measured value of θ is similar. This finding is particularly important for industrial design where operational density ratios are expected to be $\rho_j/\rho_a \geq 1.0$. Therefore L/D can be selected to provide be insensitive to a change in ρ_j/ρ_a.

Figures 5.12, 5.13 and 5.14 show the axial variation in the jet mean centreline velocity over the L/D range for $\rho_j/\rho_a = 0.2$, 1.0 and 5.0 respectively. The data for $\rho_j/\rho_a = 0.45$ and 2.24 can be found in appendix A. The decay gradient, $\Delta(\bar{U}_1/U_c)/\Delta(x/D)$, presented in figure 5.15 is determined from the mean centreline velocities over the same range as the spread gradient (figure 5.7). These figures show internal consistency within the data sets as an increase in the spread, as presented above, results in an increase in the decay gradient.

Figures 5.16, 5.17 and 5.18 show the frequency power spectra for the TOJ at various L/D for $\rho_j/\rho_a = 0.2$, 1.0 and 5.0 respectively. This is the output from the first pressure vs time trace as determined using the Burg Maximum Entropy method. Although four pressure vs time traces were collected, there are no qualitative differences in the behaviour, and this result is typical of all four pressure traces. Again the data for $\rho_j/\rho_a = 0.45$ and 2.24 can be found in appendix A. By comparison of these figures it can be seen that increasing ρ_j/ρ_a results in a

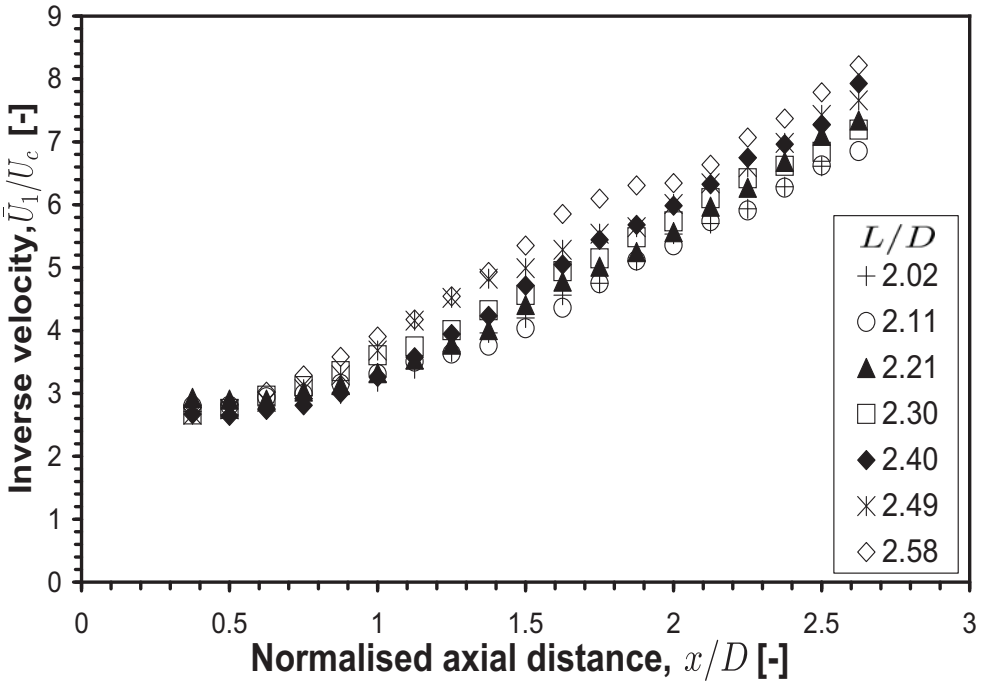

Figure 5.12: Centreline inverse velocity for the TOJ nozzle at various L/D with $\rho_j/\rho_a = 0.2$.

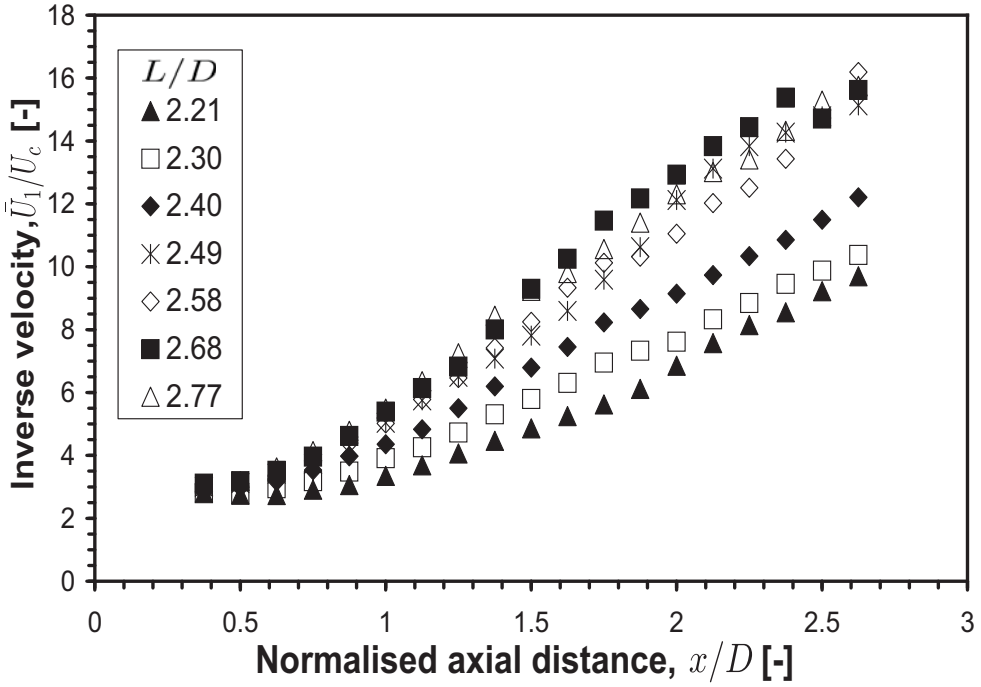

Figure 5.13: Centreline inverse velocity for the TOJ nozzle at various L/D with $\rho_j/\rho_a = 1.0$.

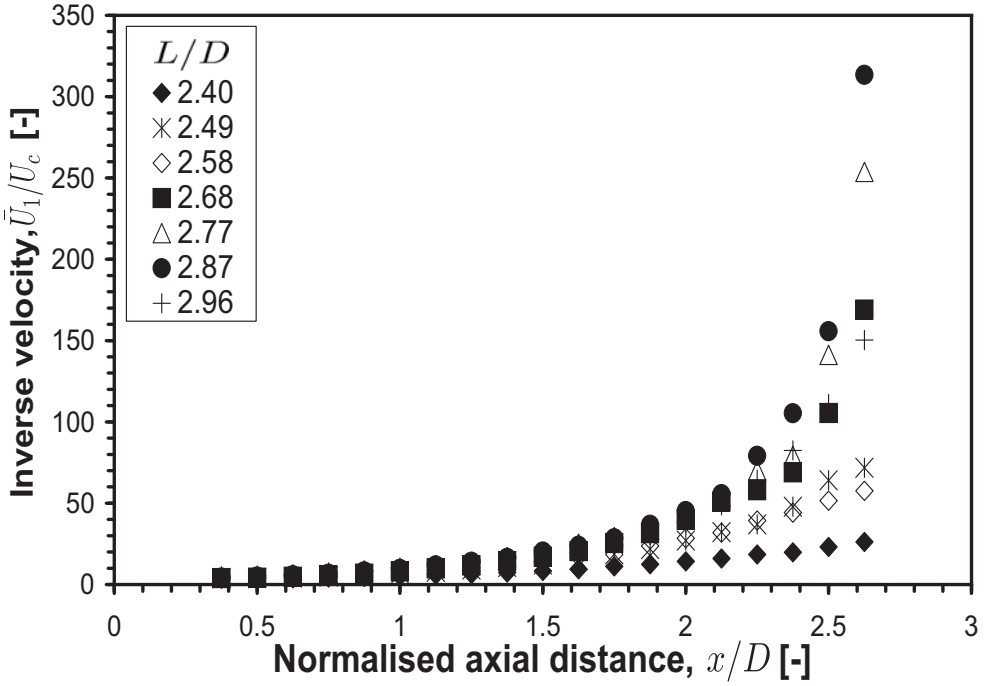

Figure 5.14: Centreline inverse velocity for the TOJ nozzle at various L/D with ρ_j/ρ_a = 5.0.

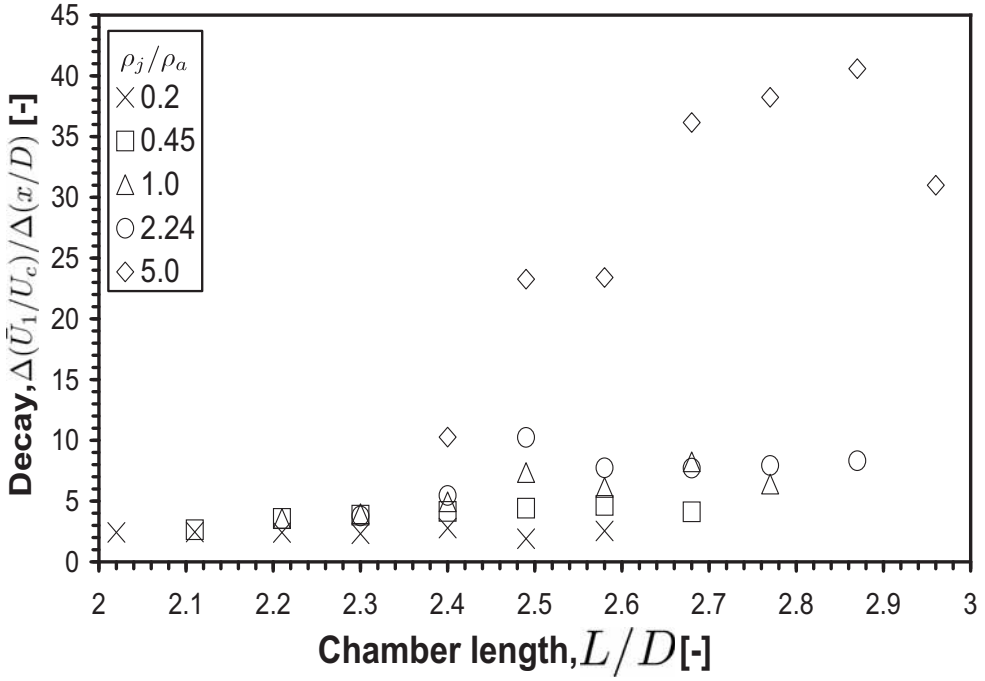

Figure 5.15: Centreline decay gradient as a function of L/D at ρ_j/ρ_a = 0.2, 0.45, 1.0, 2.24 and 5.0.

decrease in the oscillation frequency as is established in chapter 4. These figures also show that, regardless of ρ_j/ρ_a, an increase in L/D results in an increase in the frequency. This gives further evidence that the oscillation is not the result of acoustical coupling because an increase in L/D would result in a decrease in the frequency of any acoustic response. Mi and Nathan (2004) have previously investigated the frequency of oscillation as a function of L/D for the FPJ nozzle. They also found that an increase in L/D resulted in an increase in the oscillation frequency. They argue that the reason for this is that the magnitude of f_{osc} depends upon the internal axial momentum of the jet (M_x) and the angular momentum of the swirling fluid around the main jet (M_ϕ), and that increasing the ratio M_ϕ/M_x will result in greater f_{osc}. They continue by arguing that increasing the chamber length increases the ratio M_ϕ/M_x. This is due to the swirling fluid being comprised of both fluid from the main jet and fluid induced from outside the nozzle, and with greater L/D more of the swirling fluid will be from the main jet and less induced from the ambient due to greater jet spread within the chamber. Therefore more of the initially axial momentum is converted to angular momentum, and hence the increase in M_ϕ/M_x and subsequently f_{osc}.

In chapter 4 it was shown that decreasing ρ_j/ρ_a resulted in an increase of f_{osc}. Therefore it can be argued that decreasing ρ_j/ρ_a is analogous to increasing L/D with respect to f_{osc}. In chapter 4, where ρ_j/ρ_a was investigated at fixed L/D, the initial axial momentum (at the orifice) was identical in each case. Mi and Nathan (2004) found that f_{osc} is dependent upon M_ϕ/M_x, with an increase in the ratio resulting in an increase in f_{osc}. In their explanation they argue that greater internal jet spread results in more of the initially axial momentum being converted into angular momentum resulting in greater M_ϕ/M_x, and hence f_{osc}. This therefore implies that, since a decrease in ρ_j/ρ_a results in an increase of f_{osc}, more of the axial momentum has been converted into angular momentum, meaning there must be increased spreading of the jet within the chamber. Greater internal jet spread at a fixed L/D implies that the critical L/D will occur at a smaller L/D. To confirm this a more detailed understanding of flow within the chamber under variable density conditions is required.

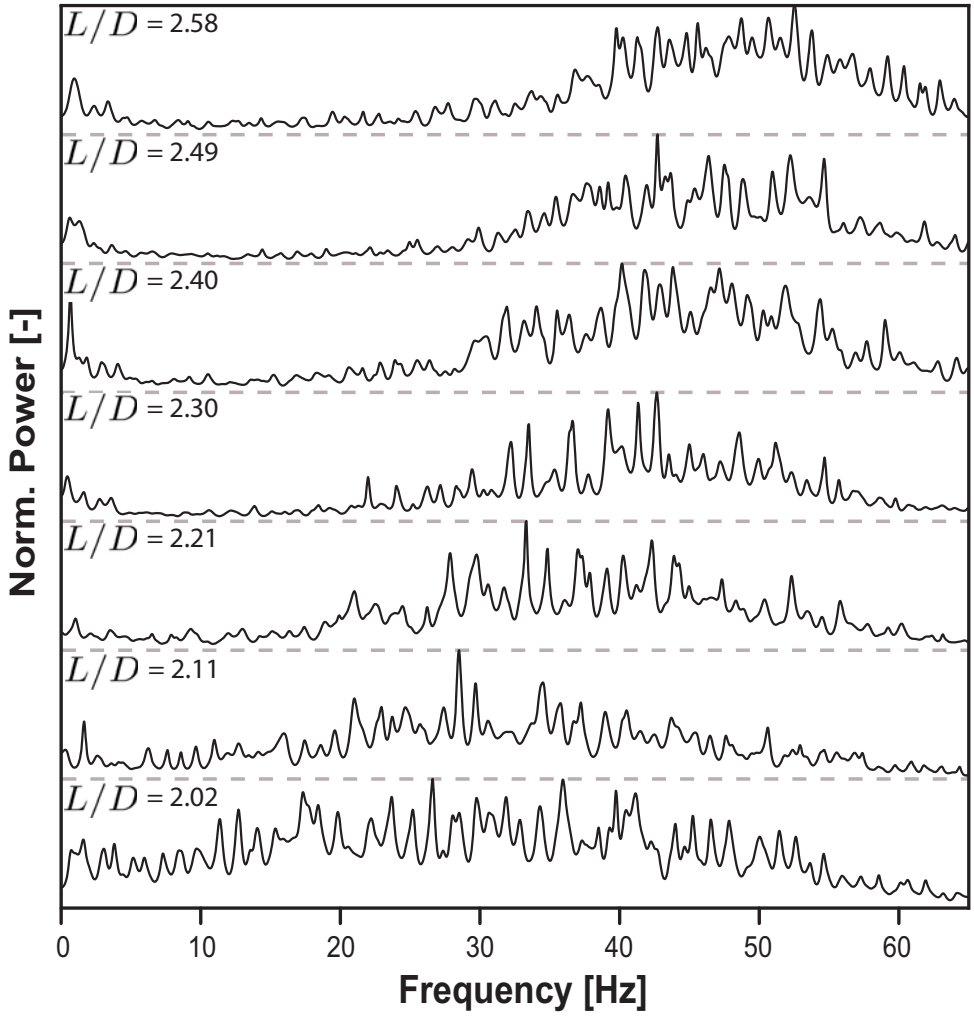

Figure 5.16: Frequency power spectra for all L/D, with density ratio, ρ_j/ρ_a=0.2.

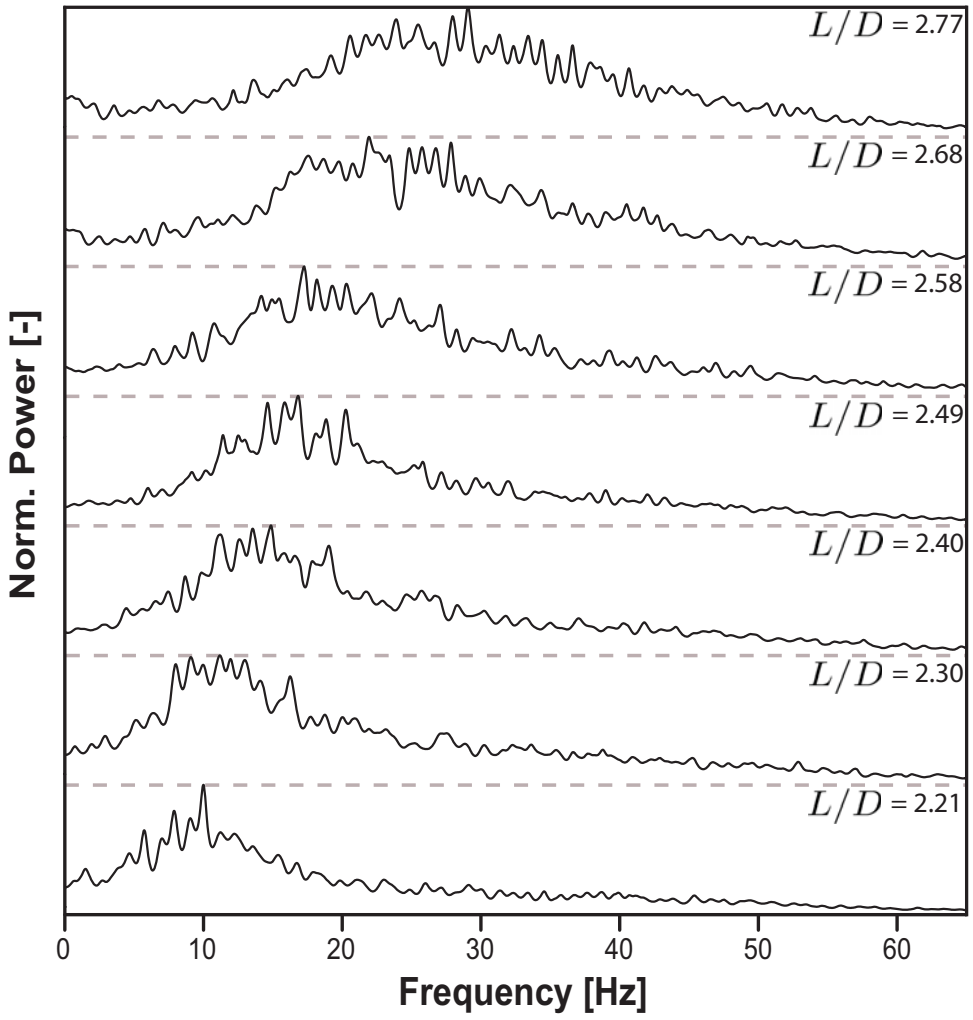

Figure 5.17: Frequency power spectra for all L/D, with density ratio, ρ_j/ρ_a=1.0.

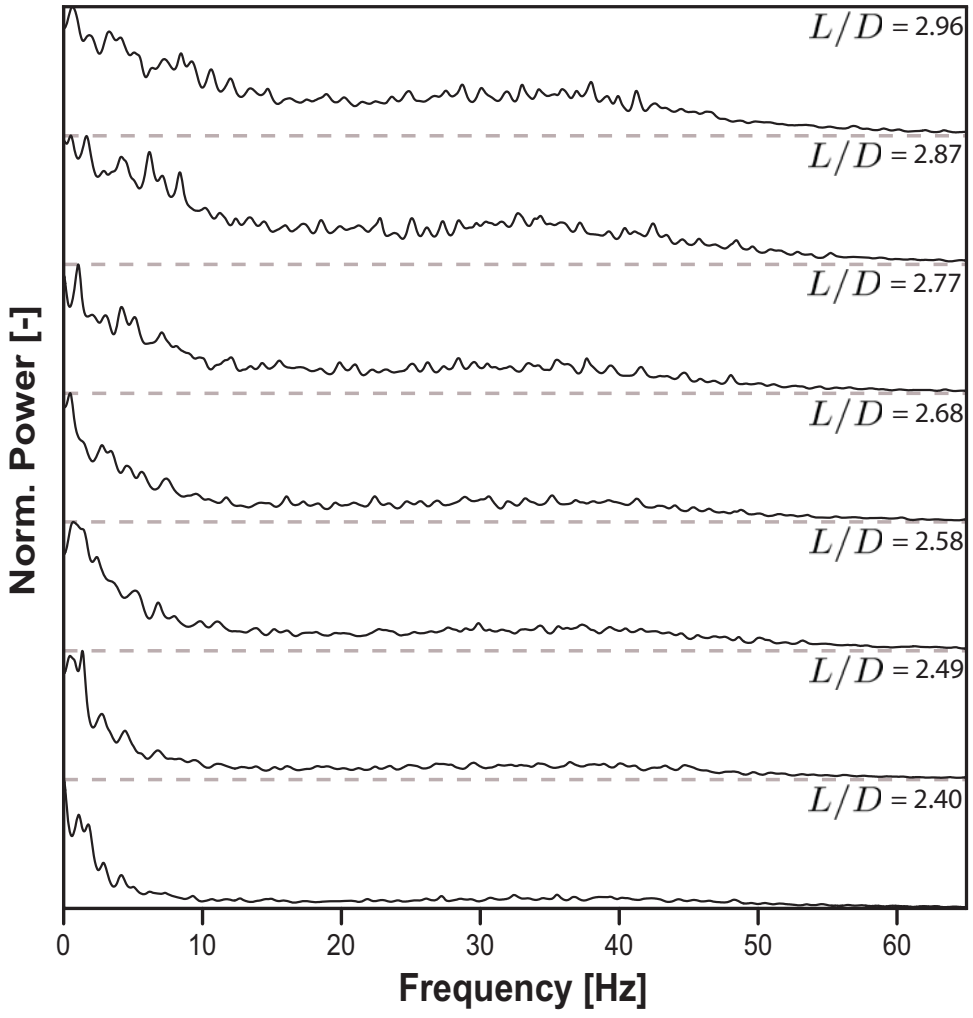

Figure 5.18: Frequency power spectra for all L/D, with density ratio, ρ_j/ρ_a=5.0.

5.4 Conclusions

Velocity measurements by PIV and pressure measurements of the oscillation frequency have been used to investigate the flow from a TOJ nozzle at various chamber lengths for five different density ratios. Except for $\rho_j/\rho_a = 0.2$, where no influence of L/D is observed, the half-widths calculated from the PIV data show that an increase in the chamber length results in an increase in the mean spread. The jet deflection angle and mean centreline decay, also calculated from the PIV data, are consistent with this result. Based on the data presented, determination of any critical L/D, the L/D for which maximum spread is observed, was not possible for the investigated density ratios. This may be due either to the critical L/D not lying within the investigated range, or the scatter in the data being comparable with the low gradient in θ with respect to L/D. This finding contradicts the work of Lee et al (2003) who determined the critical L/D for $\rho_j/\rho_a = 1.0$ to be 2.50. Therefore, further investigation into the effects of the chamber length on the flow development under variable density conditions is warranted, and should be the focus of future work. The results do however show that for a fixed L/D, the instantaneous jet deflection angle is not sensitive to a change in ρ_j/ρ_a providing that $\rho_j/\rho_a \geq 1.0$.

Oscillation frequency measurements show that, regardless of the density ratio, an increase in the chamber length results in an increase in the frequency of oscillation. This is consistent with results published in the literature for a FPJ nozzle with unity density ratio. It also shows that an increase in the chamber length is analogous to a decrease in the density ratio between the jet fluid and the ambient fluid.

Since kiln dimensions depend on the process, nozzle dimensions must be tailored to each kiln to produce optimum performance. To optimally design a TOJ nozzle for use in a rotary kiln, knowledge of the effects of changing the chamber length at various fluid density ratios is required, enabling the design to function effectively over the desired operating temperature range. Expected operating temperature will result in operational density ratios of $\rho_j/\rho_a \geq 1.0$. Given that the instantaneous deflection angle, and hence mean spread, is insensitive to changes in ρ_j/ρ_a at fixed L/D, for $\rho_j/\rho_a \geq 1.0$, effects of ρ_j/ρ_a can then essentially be ignored

when designing a nozzle for industrial use. However, to further assist in nozzle design, knowledge of the chamber's critical length as a function of density ratio would be extremely helpful. Since the data presented here do not clearly identify this relationship, further investigation is required. Knowledge of the internal flow under variable density conditions would also significantly aid in future nozzle design.

Chapter 6

Density Effects Uncoupled from Viscosity

6.1 Introduction

Chapter 4 investigated the effect of density ratio on the TOJ flow at a fixed L/D. However in that investigation the factor of 25 change in density ratio was accompanied by a factor of less than 1.3 change of opposite sign in the viscosity ratio. As such the effect of density ratio and viscosity ratio were coupled, although not strongly. It is important to understand the effect of the density separately from viscosity. To meet this need, the aim of the present chapter is to investigate the effect of density ratio uncoupled from viscosity ratio on the flow in the near field of the emerging flow from a TOJ nozzle.

The parameters used in the investigation are as follows. As described in section 3.3.2 the jet fluid is introduced through the nozzle with a momentum flux of 0.06 kgms^{-2}. The bulk mean velocity and Reynolds number for each case as a result of this momentum flux are shown in table 6.1, which describes the conditions for variable density with a fixed viscosity ratio of 1.02. To achieve these conditions, gas mixtures were chosen from blends of the gases discussed in section 3.1 as well as argon and carbon dioxide. The nozzle chamber length parameter, L/D, was fixed at 2.49, with all other nozzle dimensions fixed as described in section 3.2.

Gas mixture	ρ_j/ρ_a	$\bar{U}_1$ [ms^{-1}]	Re [$\times 10^3$]
He 73.1% - CO_2 26.9%	0.52	46.13	12.6
He 21.4% - Air 78.6%	0.82	36.87	15.8
Ar 9.1% - Air 90.9%	1.04	32.72	17.8
Ar 50.0% - CO_2 50.0%	1.47	27.44	21.2
He 70.2% - SF_6 29.8%	1.65	25.90	22.5
Ar 46.4% - SF_6 53.6%	3.44	17.95	32.5

Table 6.1: Operating conditions for variable density TOJ with fixed viscosity ratio, $\mu_j/\mu_a = 1.02$.

6.2 Results and Discussion

Figure 6.1 presents the axial velocity component of the ensemble averaged flow fields, $u/\bar{U}_1$, for all density ratios examined with the viscosity ratio fixed at 1.02. Here the axial component, u, of the velocity is normalised by the bulk mean orifice velocity $\bar{U}_1$. This figure shows a similar trend to that in figure 4.1, in that as ρ_j/ρ_a is increased, the contour envelope tends to become shorter and broader, indicating greater jet spread and a higher rate of jet decay. It is noted that the velocities measured in the region $r/D \leq$ -0.7 are slightly increased compared with the velocities in the region $r/D \geq 0.7$. This was due to a problem with the co-flow seeding system causing a bias in the seeding co-flow momentum. However as it is present in all cases, the trends can still be considered to be reliable.

Figure 6.2a shows the normalised mean half widths, $\bar{r}_{1/2}/D$, and figure 6.2b shows the gradient of spread for the TOJ nozzle at each of the density ratios investigated. The gradient of spread, $\Delta\bar{r}_{1/2}/\Delta x$, was determined from the half widths over the range $x/D = 1.25$ - 2.0. Due to a lack of half width data in the range over which the gradient of spread was calculated, the gradient of spread for ρ_j/ρ_a=3.44 is unreliable, and is therefore not presented. Together figure 6.2a and b show that a decrease in ρ_j/ρ_a below unity results in a corresponding decrease in the jet spread, and an increase in ρ_j/ρ_a above unity results in a corresponding increase in the jet spread. However the effect of an increase in ρ_j/ρ_a above unity is much less significant than that below unity. Also shown in figure 6.2b is the result presented in chapter 4 where both ρ_j/ρ_a and μ_j/μ_a were varied. The trend and relative magnitude of the results for fixed μ_j/μ_a are within experimental

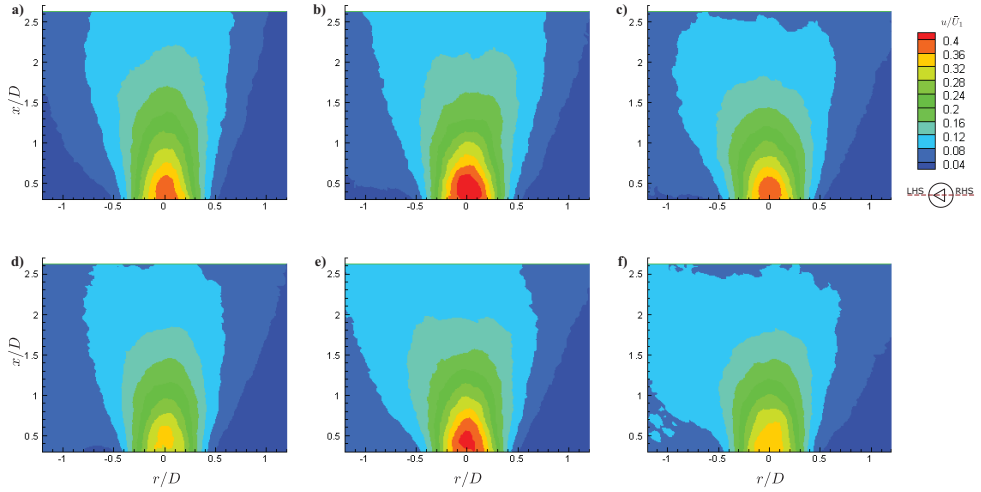

Figure 6.1: Axial velocity component of the ensemble averaged flow fields, $u/\bar{U}_1$, with viscosity ratio, μ_j/μ_a= 1.02 and density ratio ρ_j/ρ_a= a) 0.52, b) 0.82, c) 1.04, d) 1.47, e) 1.65 and f) 3.44.

uncertainty of the result measured when μ_j/μ_a was not fixed. This comparison suggests that, while μ_j/μ_a must influence the development of the jet, it plays a less significant role than ρ_j/ρ_a.

It is shown in chapter 4 that the jet spread is strongly correlated with the instantaneous deflection angle, θ. Therefore figure 6.3 presents the conditionally averaged measurement of instantaneous deflection for the TOJ with various ρ_j/ρ_a and with μ_j/μ_a= 1.02. This shows qualitatively that θ is larger at higher values of ρ_j/ρ_a. To give a quantitative measure of θ the probability density analysis (section 3.3.10.2) was used. The result is shown in figure 6.4. Figure 6.5 then presents θ, as determined from figure 6.4, as a function of ρ_j/ρ_a and μ_j/μ_a= 1.02. This shows that decreasing ρ_j/ρ_a below unity reduces θ, while an increase in ρ_j/ρ_a above unity increases θ. The dependence of θ on ρ_j/ρ_a also appears to be much more significant when ρ_j/ρ_a is less than unity. This is consistent with the result presented in chapter 4.

The measurements of deflection angle, θ, previously presented in chapter 4 for variable μ_j/μ_a is also shown in figure 6.5. This allows a direct comparison between the dependence of θ on ρ_j/ρ_a both with and without fixed μ_j/μ_a. In this figure the solid symbols are calculated for cases where μ_j/μ_a is variable and hollow symbols are for cases where μ_j/μ_a is fixed at 1.02. That there is good agreement between

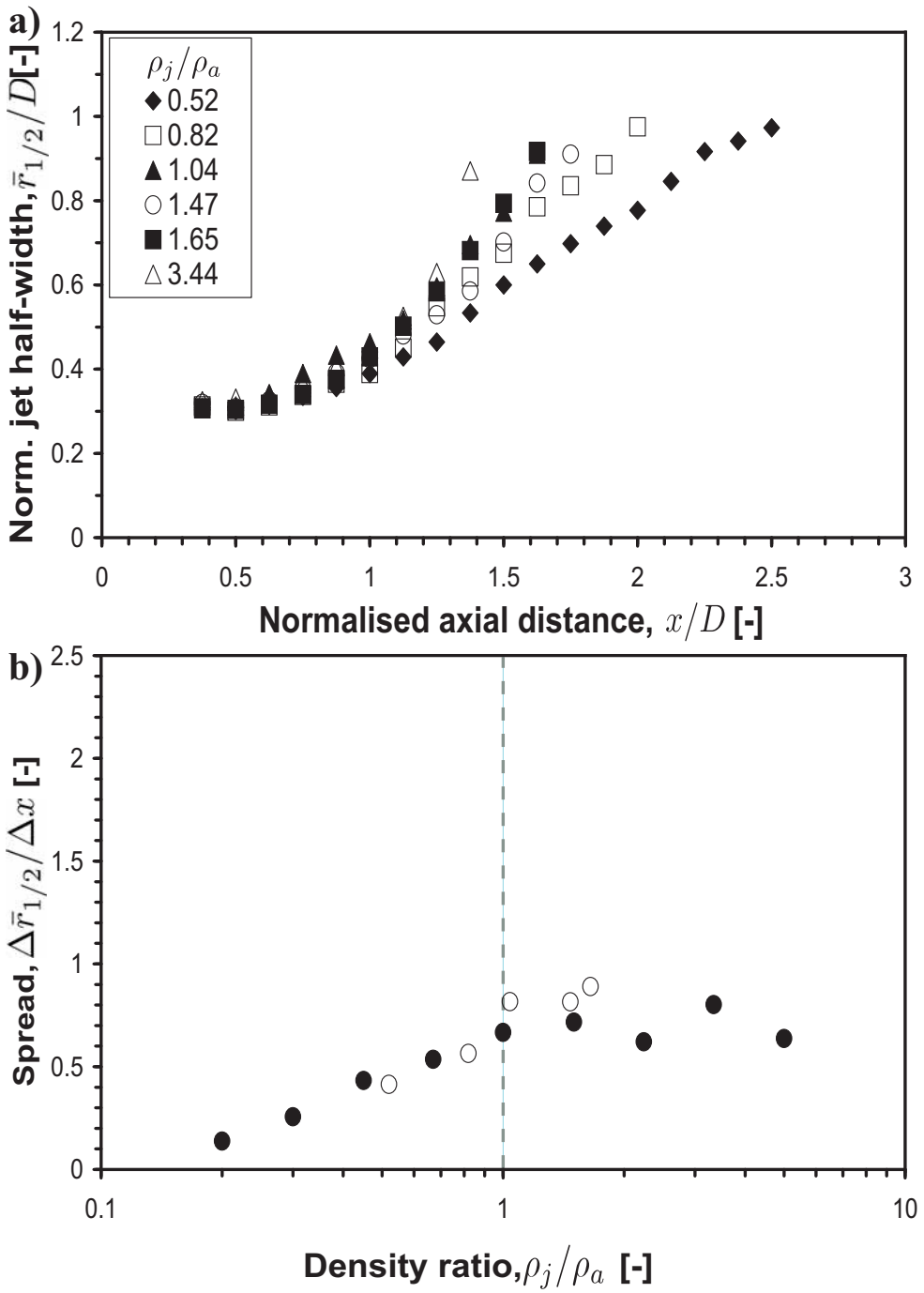

Figure 6.2: a) Mean half widths for the TOJ nozzle at various density ratios, ρ_j/ρ_a, with μ_j/μ_a= 1.02, and b) gradient of spread with: Hollows μ_j/μ_a= 1.02 and Solids μ_j/μ_a variable.

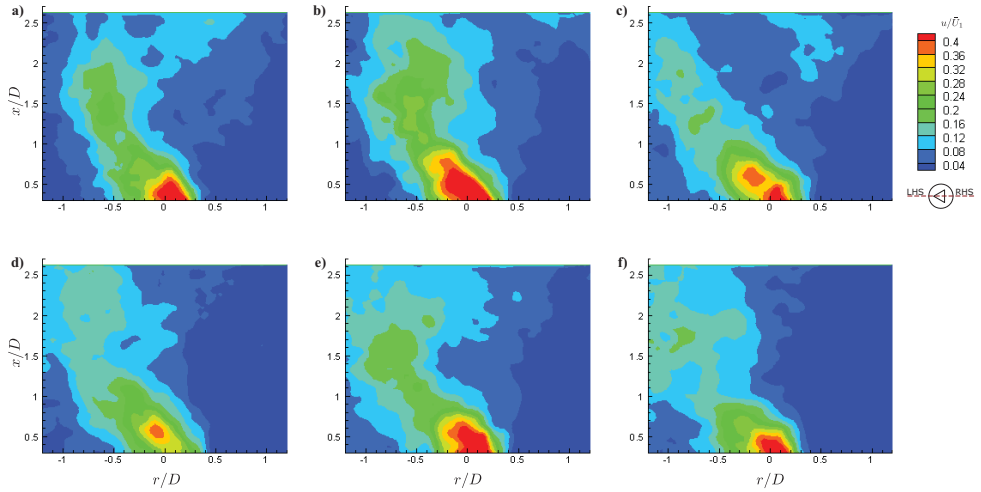

Figure 6.3: Axial velocity component of the conditionally averaged flow fields, $u/\bar{U}_1$, with viscosity ratio, μ_j/μ_a= 1.02 and density ratio ρ_j/ρ_a= a) 0.52, b) 0.82, c) 1.04, d) 1.47, e) 1.65 and f) 3.44.

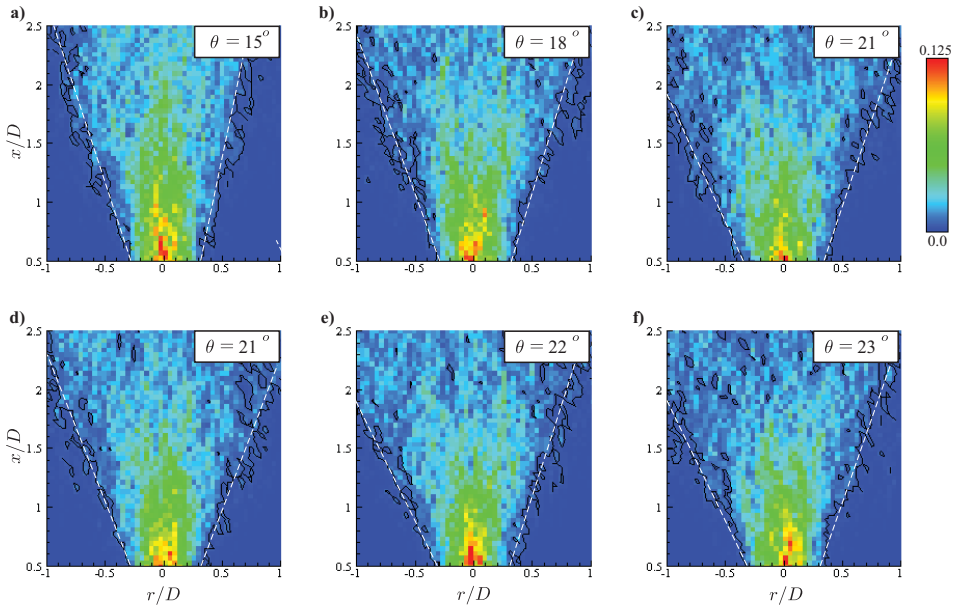

Figure 6.4: Probability density of maximum velocity magnitude for density ratios a) 0.52, b) 0.82, c) 1.04, d) 1.47, e) 1.65 and f) 3.44 with $\mu_j/\mu_a = 1.02$.

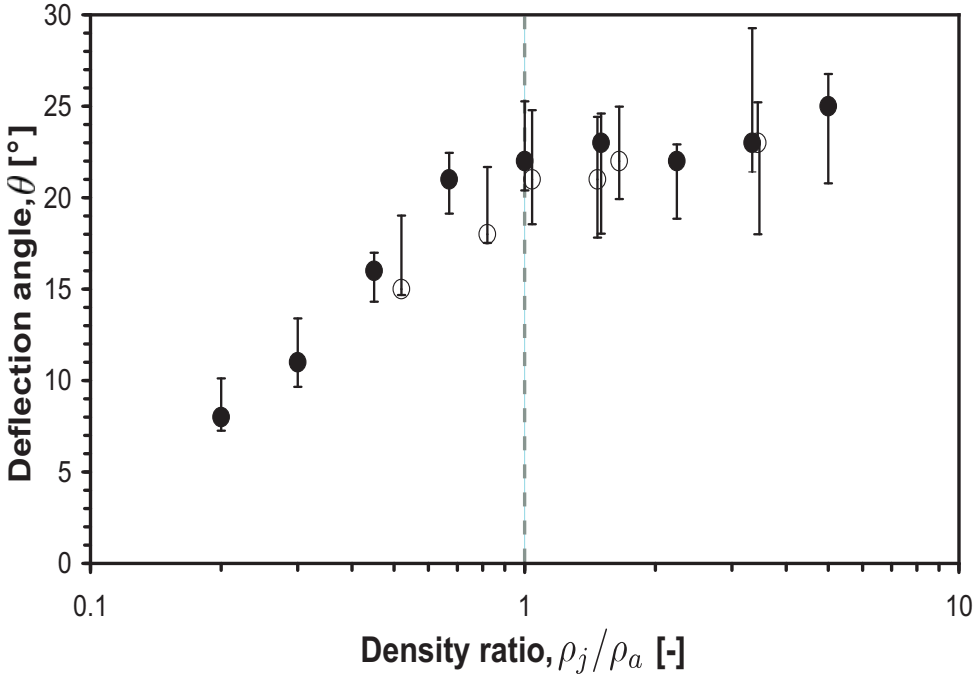

Figure 6.5: Deflection angle, θ, of the instantaneous emerging jet as a function of density ratio, ρ_j/ρ_a, with: Hollows $\mu_j/\mu_a = 1.02$ and Solids μ_j/μ_a variable.

the fixed and non-fixed μ_j/μ_a cases gives further evidence that any influence of μ_j/μ_a on the mean flow from the nozzle is minor in comparison with that of ρ_j/ρ_a.

Figure 6.6a shows the axial variation in the jet mean centreline velocity, and 6.6b shows the mean velocity decay gradient for all ρ_j/ρ_a with $\mu_j/\mu_a = 1.02$. Figure 6.6b shows both the fixed and variable (from chapter 4) μ_j/μ_a data. Data are presented as an inverse velocity. The decay gradient, $\Delta(\bar{U}_1/U_c)/\Delta(x/D)$, is determined over the same range as the spread gradient (figure 6.2b). Comparing the result of figure 6.6 with figure 6.2 reveals a generally consistent trend that increasing spread corresponds to an increase in decay as expected. Figure 6.6b shows that for $\rho_j/\rho_a \leq 2$ there is some agreement between the fixed and non-fixed μ_j/μ_a data. However figure 6.6b also reveals a significant difference in the decay gradient between two cases with similar ρ_j/ρ_a, namely the $\rho_j/\rho_a = 3.34$ and 3.44 cases. It is clear that this difference cannot be explained purely by the less that 3% difference in ρ_j/ρ_a between the cases. It is, however, noted that there is nearly 11% difference in the viscosity ratio present in these two cases.

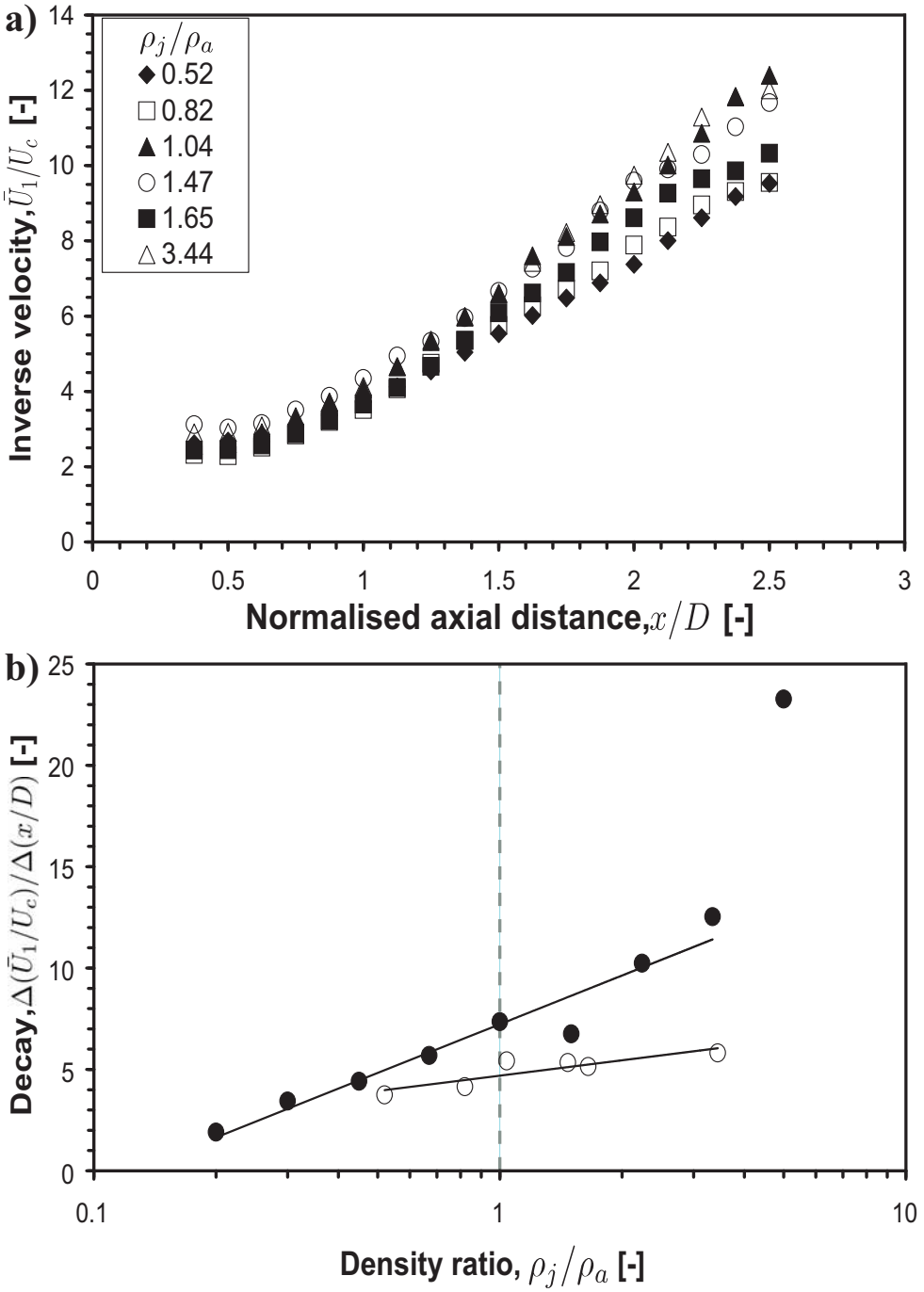

Figure 6.6: a) Centreline inverse velocity at various density ratios, ρ_j/ρ_a, and b) centreline decay gradient, with: Hollows μ_j/μ_a= 1.02 and Solids μ_j/μ_a variable.

ρ_j/ρ_a	μ_j/μ_a	% difference in μ_j/μ_a from 1.02
0.2	1.09	+7.08
0.3	1.08	+5.96
0.45	1.06	+4.29
0.67	1.04	+1.78
1.0	1.00	-1.96
1.50	0.98	-3.83
2.24	0.95	-6.62
3.34	0.91	-10.80
5.0	0.85	-17.05

Table 6.2: Corresponding viscosity ratio for each density ratio for the non-fixed viscosity data and the percentage difference in viscosity ratio from the fixed viscosity data.

It is therefore plausible that the large difference in the decay is caused by the significant difference in μ_j/μ_a. In fact, the lines of best fit through the fixed and non-fixed μ_j/μ_a data have significantly different slopes. With the only parametric difference between the data sets being the variability of μ_j/μ_a, one must conclude that, within experimental error, the difference in the slopes is due to the effect of μ_j/μ_a. It should be noted that the exceptionally high decay of the data point $\rho_j/\rho_a = 5.0$ is attributed to the conical divergence as previously discussed in chapter 4. Hence this point was not included in the determination of the line of best fit.

It is therefore clear that μ_j/μ_a does influence the development of the flow. Previously it was noted that, with respect to jet spread and jet deflection angle, the influence of μ_j/μ_a was less significant when compared with the influence of ρ_j/ρ_a. By use of the values presented in table 6.2, it can be seen that for the variable μ_j/μ_a data there is a factor of 25 difference between the least and greatest ρ_j/ρ_a, but that the corresponding difference in μ_j/μ_a is less than a factor of 1.3. Therefore the fact that flow development is dominated by ρ_j/ρ_a rather than μ_j/μ_a is most likely due to the relative change in these parameters over the range being an order of magnitude larger for ρ_j/ρ_a.

Figure 6.7 shows the frequency power spectra for the TOJ at various ρ_j/ρ_a with $\mu_j/\mu_a = 1.02$. This is the output from the first pressure vs time trace as determined using the Burg Maximum Entropy method. Although four pressure vs

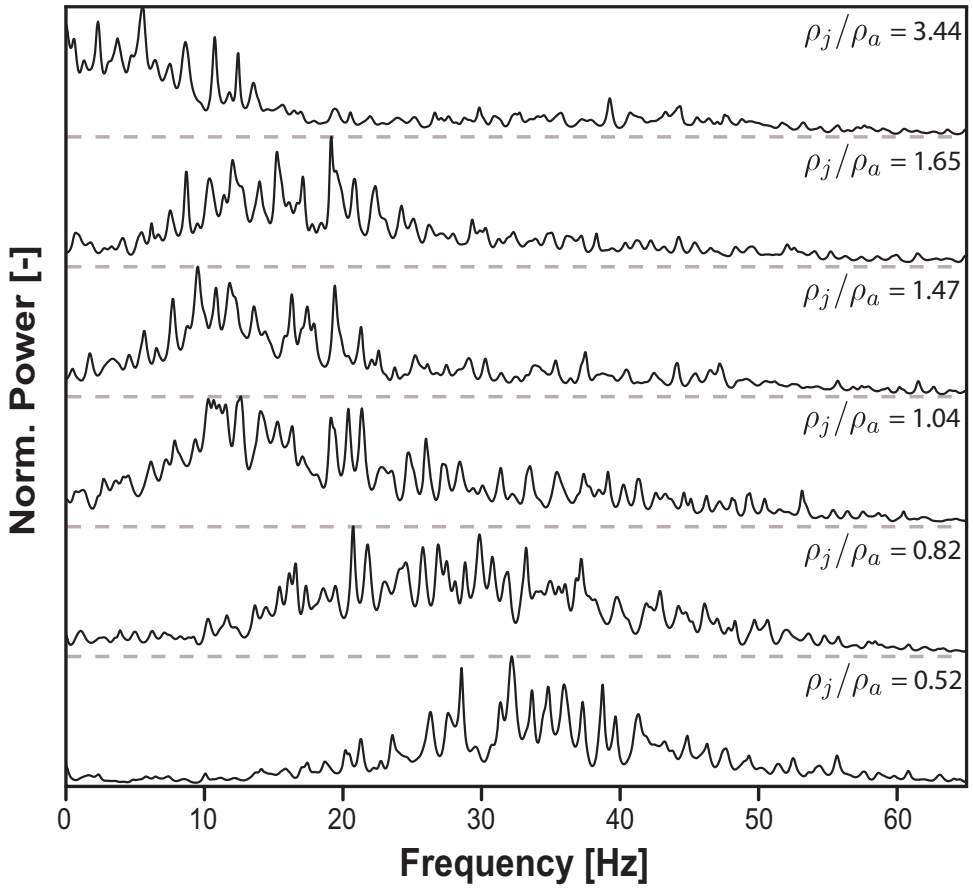

Figure 6.7: Frequency power spectra for all density ratios, ρ_j/ρ_a, with viscosity ratio, $\mu_j/\mu_a = 1.02$.

time traces were collected, there are no qualitative differences in the behaviour, and this result is typical of all four pressure traces. Figure 6.7 clearly shows that, as ρ_j/ρ_a is increased, f_{osc} decreases. The value of f_{osc} as a function of ρ_j/ρ_a with $\mu_j/\mu_a = 1.02$ is shown in figure 6.8. Also shown in figure 6.8 is the measured result calculated using the Burg Maximum Entropy method for when both μ_j/μ_a and ρ_j/ρ_a were variable as previously presented in chapter 4.

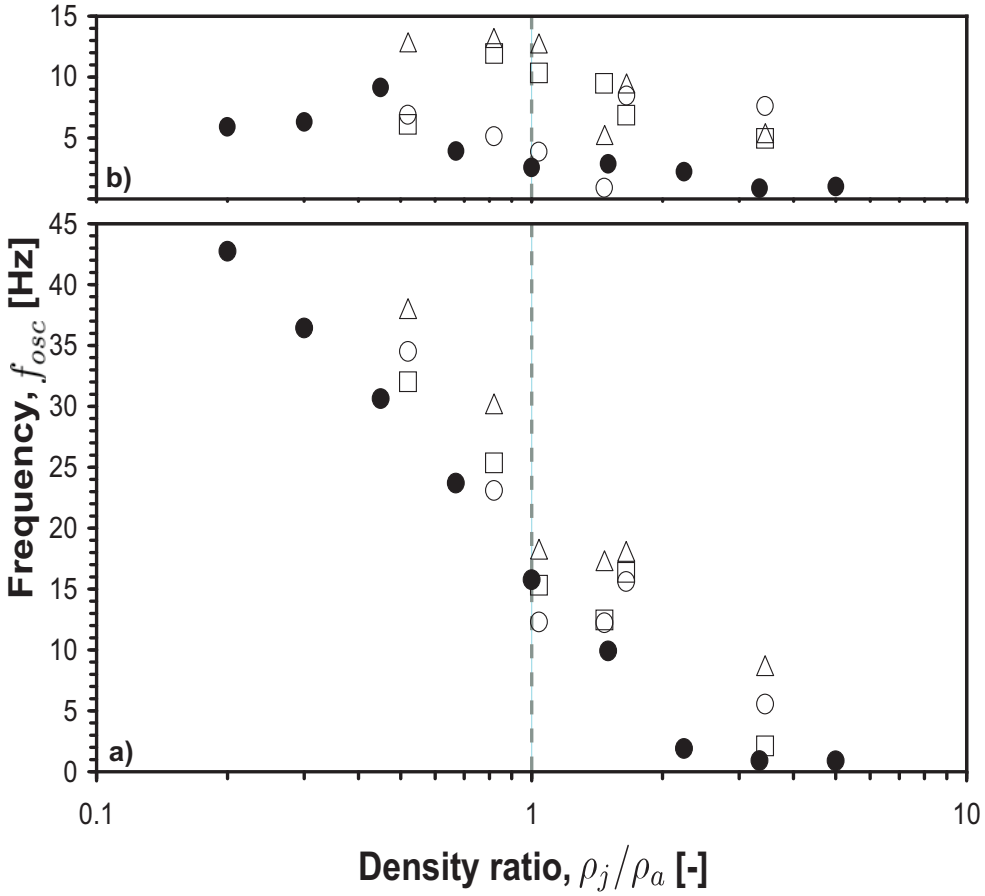

Figure 6.8: a) Oscillation frequency, f_{osc}, as a function of density ratio, ρ_j/ρ_a, with viscosity ratio: Hollow μ_j/μ_a= 1.02, Solid μ_j/μ_a variable, and b) Measurement uncertainty. (Circles = FFT, Squares = Burg-MEM, Triangles = Peak counting)

Figure 6.9 presents St_{osc} as a function of ρ_j/ρ_a. When the measurement uncertainty is taken into consideration, figure 6.9 shows that the trend and order of magnitude are the same whether μ_j/μ_a is fixed or variable. Again this shows that while μ_j/μ_a influences the flow from the TOJ nozzle, any effect caused by μ_j/μ_a is minor in comparison to the effect of ρ_j/ρ_a.

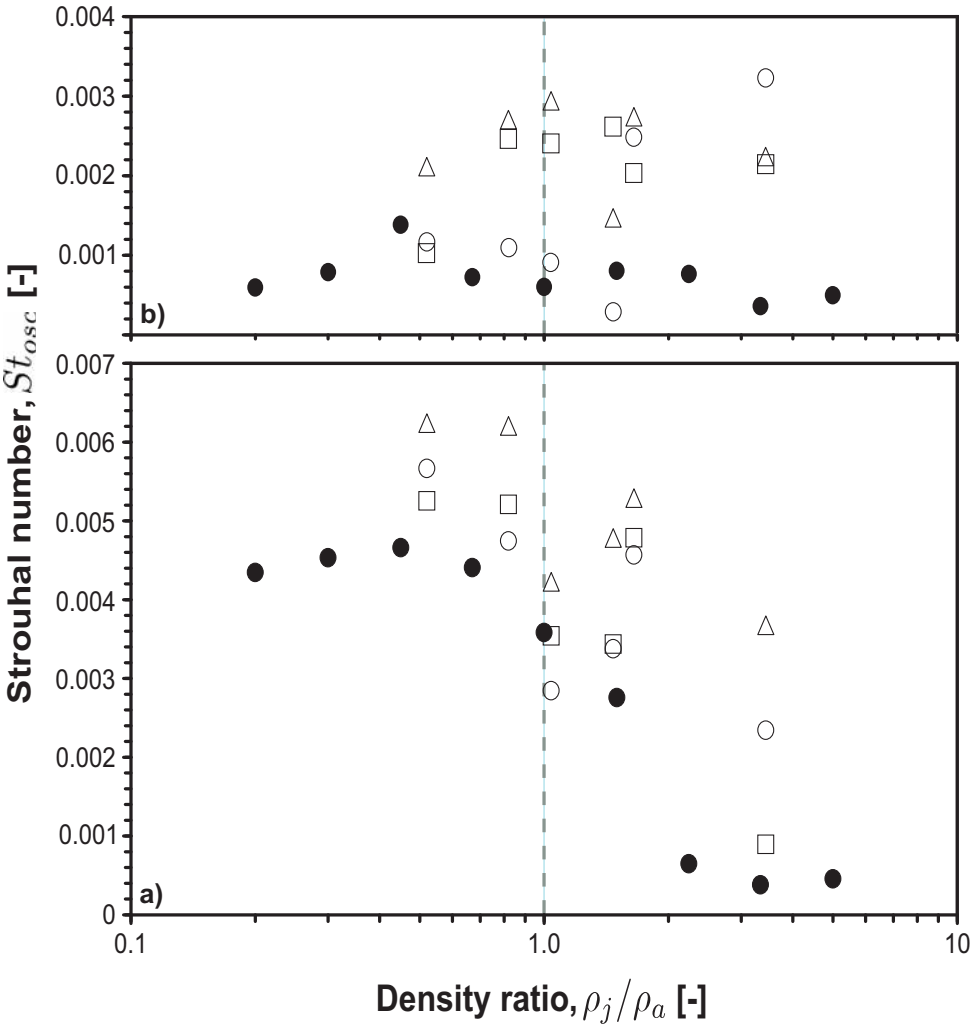

Figure 6.9: a) Jet Strouhal number, St_{osc}, as a function of density ratio, ρ_j/ρ_a, with viscosity ratio: Hollow μ_j/μ_a= 1.02, Solid μ_j/μ_a variable, and b) Measurement uncertainty. (Circles = FFT, Squares = Burg-MEM, Triangles = Peak counting)

While the results presented show that the effect of viscosity ratio is minor compared to that of density ratio, the effects of viscosity ratio are still noticeable. Figure 6.10 shows the viscosity of air as a function of temperature as determined using Sutherland's law (equation 6.1) and the power law (equation 6.2) for an ideal gas. For air the constants for Sutherland's law C, μ_0 and T_0 are 120 K, 1.827×10^{-5} Pa.s and 291.15 K respectively, and for the power law μ_0, T_0 and ω are 1.716×10^{-5} Pa.s, 273 K and 2/3. By use of Sutherland's law the value of μ_j/μ_a for ambient air emitting into air at a typical cement kiln secondary air temperature of 1200°C is 0.35. At this secondary air temperature $\rho_j/\rho_a = 5.0$. Therefore μ_j/μ_a for a typical secondary air temperature is less than half the value investigated, which is $\mu_j/\mu_a = 0.85$, for the corresponding density ratio of $\rho_j/\rho_a = 5.0$. Therefore it is quite conceivable that for industrial design the effects of viscosity ratio cannot be neglected.

$$\mu = \mu_0 \frac{T_0 + C}{T + C} \left(\frac{T}{T_0}\right)^{3/2} \tag{6.1}$$

$$\mu = \mu_0 \left(\frac{T}{T_0}\right)^{\omega} \tag{6.2}$$

Due to the possibility of viscosity ratio being important, a study on the effect of changing μ_j/μ_a at fixed ρ_j/ρ_a was conducted. With constraints on the gas mixtures able to be used in this study the viscosity range was small ($0.82 \leq \mu_j/\mu_a \leq 1.03$). The lower bound of this range was also still more than twice that which could be expected to be seen in a typical cement kiln. The results of this investigation (shown in appendix B) did not reveal any clear and consistent trends on how μ_j/μ_a effects the flow in the near field region of the TOJ flow. Also literature searches found no relevant previous studies on the effects of μ_j/μ_a that have been published with which to compare the present studies results with. Therefore no conclusion are drawn from this data. However, this highlights the fact the future work should address the effects of μ_j/μ_a both on the TOJ and on simple jet flows.

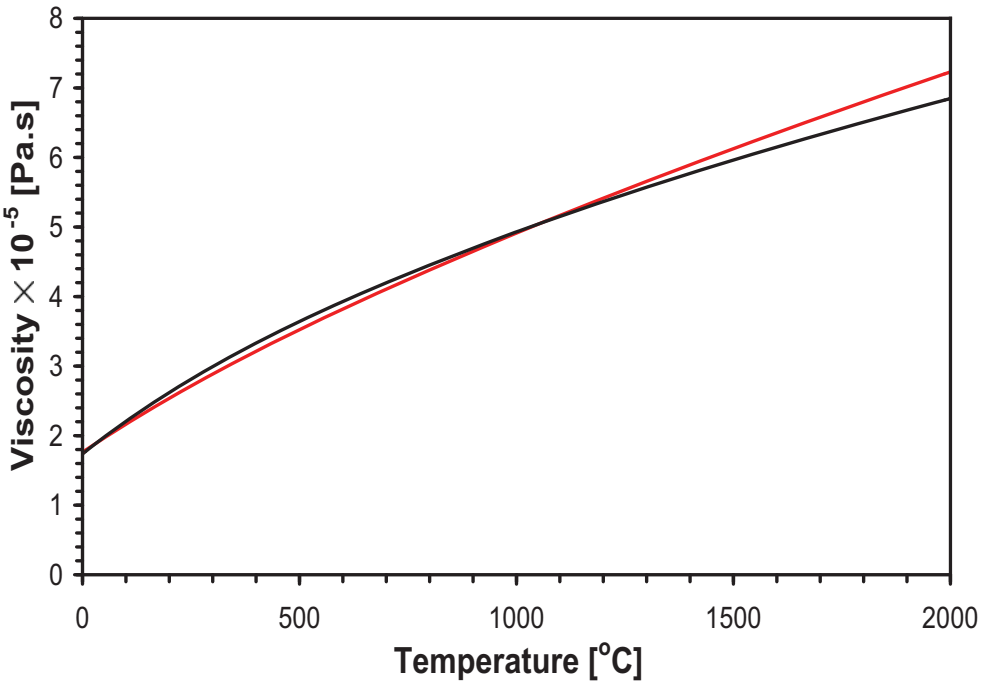

Figure 6.10: Viscosity of air with respect to temperature (Black: Sutherland's law, Red: Power law).

6.3 Conclusions

Velocity measurements by PIV and pressure measurements of the oscillation frequency have been used to investigate the flow from a TOJ nozzle under variable density - fixed viscosity conditions. Half-widths and centreline decay calculated from the PIV data, as well as the instantaneous jet deflection angle, show similar trends to those observed in chapter 4, where density was varied without fixing the viscosity. However, while the trends are similar there are some differences that cannot be entirely explained by measurement uncertainty, particularly for the centreline decay. It is clear therefore that both density and viscosity influence the near field flow of the TOJ nozzle. The data show that when density and viscosity are coupled the influence on the flow is dominated by the effect of density, although, as the change in these parameters over the range is an order of magnitude different, the effects of viscosity may still be important. As such future work should investigate the effects of viscosity ratio on the near field flow of the TOJ nozzle.

Oscillation frequency measurements also showed a similar trend to that observed in chapter 4 despite increased measurement uncertainty. Again the results show that density has a more significant effect on the TOJ flow than viscosity.

Temperature affects both the density and the viscosity of air. Therefore a change in operating temperature will result in a change to both the air density and viscosity. When designing the optimum nozzle for an installation, one needs to consider the likely variation in operating temperature. The current work suggests the effects of viscosity are small, although future work is required to confirm this when compared to the effects of density. If these results are confirmed, only the density difference over the operating temperature range needs to be considered when designing the nozzle.

Chapter 7

TOJ with Surrounding Co-annular Flow

7.1 Introduction

The previous chapters have reported investigations of the TOJ flow discharging into ambient surrounds. While the information gained from this is important, an industrial installation will most likely comprise the TOJ burner surrounded by a co-annular flow, with the combined flow from both emitted to the ambient. The reason for this burner arrangement is discussed in section 2.6.2. Therefore it is also important to understand how the combined nozzle flows are affected by changes in the density ratio. To meet this need, the aim of the present chapter is to investigate the effect of density ratio on one combined nozzle arrangement, operated at various co-annular to TOJ flow momentum ratios, on the flow in the near field region.

The parameters used in the investigation are as follows. As described in section 3.3.2 the jet fluid is introduced through the nozzle with a momentum flux of 0.06 kgms^{-2}. Three density ratios, ρ_j/ρ_a, (0.45, 1.0 and 2.24) were investigated. The bulk mean velocity and Reynolds number for the TOJ flow in each case corresponding to this momentum flux are shown in table 7.1. The density of fluid eminating from both the TOJ and co-annular component of the nozzle flow was the same (ρ_{TOJ}/ρ_{c-a}=1.0). The co-annular fluid was introduced through

ρ_j/ρ_a	$\bar{U}_1$ [ms^{-1}]	Re_{TOJ} [$\times 10^3$]	M_{c-a}/M_{TOJ}	$\bar{U}_{c-a}$ [ms^{-1}]	Re_{c-a} [$\times 10^3$]
0.45	49.79	11.2	0.1	13.25	3.55
			0.32	23.55	6.32
			1.0	41.89	11.2
			3.16	74.49	20.0
			10.0	132.46	35.5
1.0	33.30	17.9	0.1	8.86	5.65
			0.32	15.75	1.01
			1.0	28.01	17.9
			3.16	49.81	31.8
			10.0	88.58	56.5
2.24	22.27	28.1	0.1	5.92	8.88
			0.32	10.53	15.8
			1.0	18.73	28.1
			3.16	33.31	49.9
			10.0	59.24	88.8

Table 7.1: Operating conditions for the combined nozzle flow.

a 0.5mm channel surrounding the TOJ flow. The separation between the two flow components is shown in figure 7.1. The relevant flow parameters of the co-annular flow are shown in table 7.1 for each of the momentum ratios investigated. To achieve the described conditions, gas mixtures were formed with the gases discussed in section 3.1. The TOJ nozzle chamber length parameter, L/D, is fixed at 2.49, with all other TOJ nozzle dimensions as described in section 3.2.

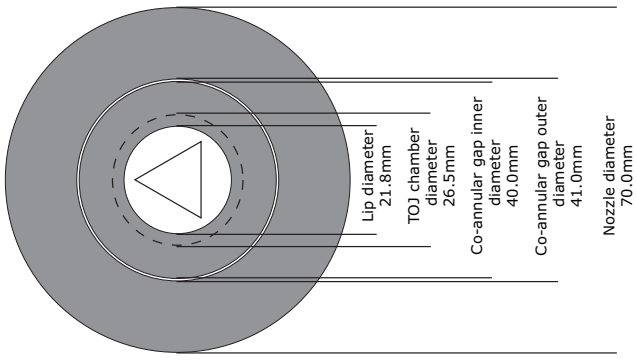

Figure 7.1: Combined nozzle dimensions as seen from view A (figure 3.7).

7.2 Results and Discussion

Figure 7.2 presents the axial velocity component of the ensemble averaged flow fields, u, for the co-annular flow only. The density ratio, ρ_j/ρ_a, is unity and the initial bulk mean velocities, $\bar{U}_{c-a}$, are shown in table 7.1. This figure shows that, despite some eccentricity, the flow from the co-annular channel is relatively uniform over a wide range of initial velocities.

Figure 7.3 presents the axial velocity component of the ensemble averaged flow fields, $u/\bar{U}_1$, for all density and momentum ratios examined. Here the axial component, u, of the velocity is normalised by the bulk mean orifice velocity of the TOJ, $\bar{U}_1$. This figure shows that, regardless of ρ_j/ρ_a, as M_{c-a}/M_{TOJ} is increased the combined flow transitions from being dominated by the oscillating component to being dominated by the co-annular component. Therefore at low M_{c-a}/M_{TOJ} the shape of the flow resembles that of the TOJ whereas at high M_{c-a}/M_{TOJ} the shape resembles that of a bluff body flow. As expected, increasing M_{c-a}/M_{TOJ} results in a decrease in the jet spread and rate of decay.

Figures 7.4, 7.5 and 7.6 show the normalised mean half widths, $\bar{r}_{1/2}/D$, of the combined nozzle at density ratios, $\rho_j/\rho_a = 0.45$, 1.0 and 2.24 respectively for all momentum ratios, M_{c-a}/M_{TOJ}. In each case all momentum ratios investigated are shown. All three show that as M_{c-a}/M_{TOJ} is increased the jet spread is decreased. The data for the axial variation in the mean centreline velocity (Appendix C) for each of the density ratios are consistent with these results in that decreased spread is accompanied by decreased centreline decay. The transition of the flow from TOJ dominated to co-annular dominated and the resulting change in the spread and decay are interesting. However, the primary aim of the present investigation is to assess the effects of density. Therefore, what is of more interest here is how the spread gradient and decay gradient change with respect to a change in ρ_j/ρ_a at fixed M_{c-a}/M_{TOJ}.

Figures 7.7, 7.8 and 7.9 show the normalised mean half widths, $\bar{r}_{1/2}/D$, of the combined nozzle at momentum ratios, $M_{c-a}/M_{TOJ} = 0.1$, 1.0 and 10.0 respectively for all density ratios, ρ_j/ρ_a, investigated. It can be seen from the three figures that each momentum ratio produces different behaviour. This is the result of the change in M_{c-a}/M_{TOJ} shifting the flow from one that is dominated by the

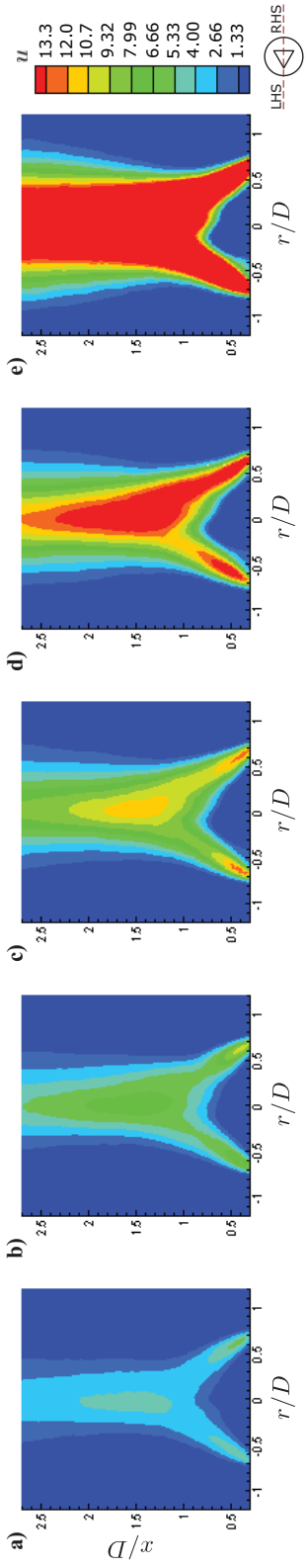

Figure 7.2: Axial velocity component of the ensemble averaged flow fields, u, for the nozzle co-annular flow only with $\rho_j/\rho_a = 1.0$ and $\bar{U}_{c-a}$ = a) 8.86, b) 15.75, c) 28.01, d) 49.81 and e) 88.58 (ms^{-1}).

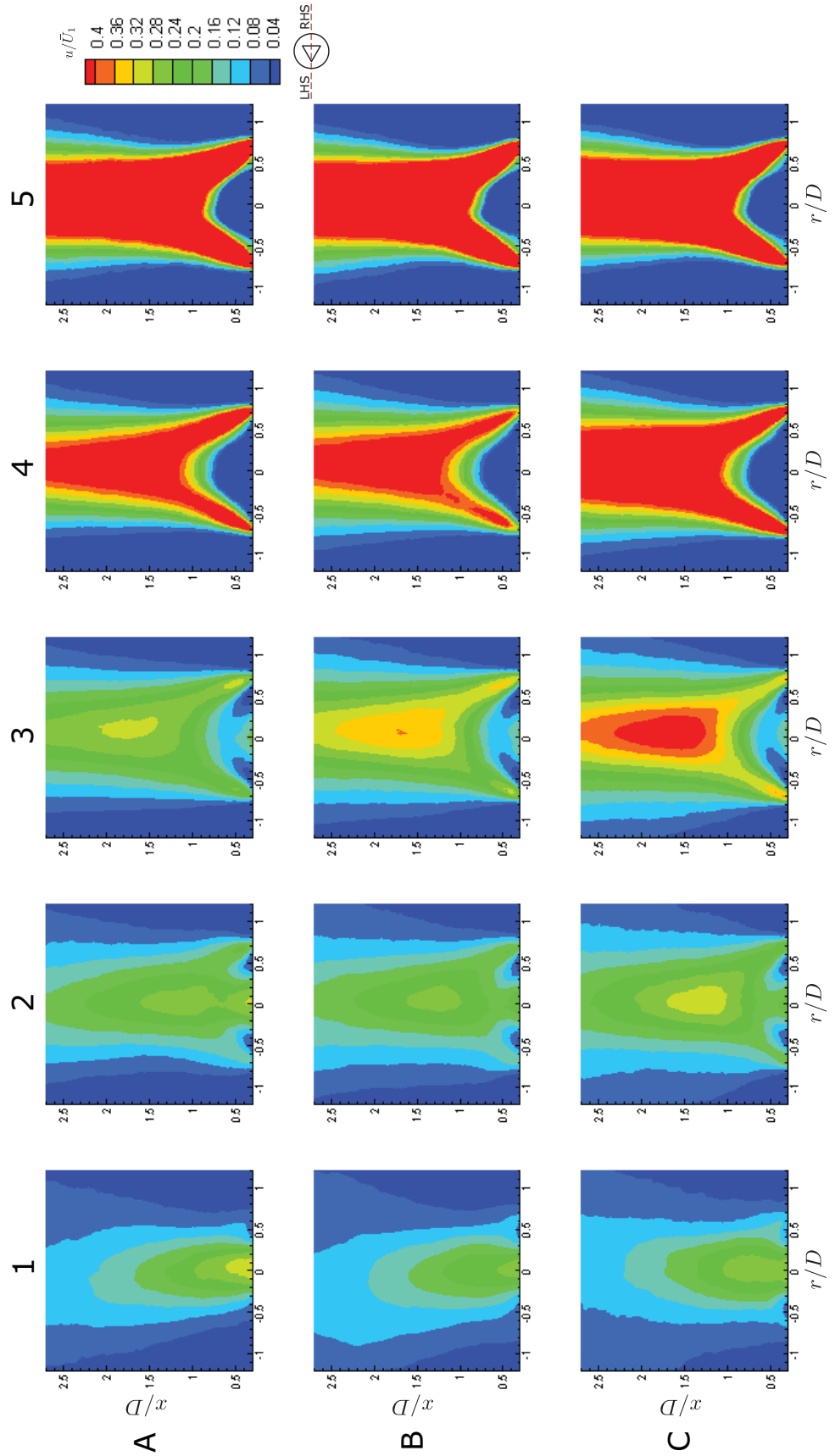

Figure 7.3: Axial velocity component of the ensemble averaged flow fields, $u/\bar{U}_1$, with density ratio ρ_j/ρ_a= A) 0.45, B) 1.0 and C) 2.24 and momentum ratio, M_{c-a}/M_{TOJ}= 1) 0.1, 2) 0.32, 3) 1.0, 4) 3.16 and 5) 10.0.

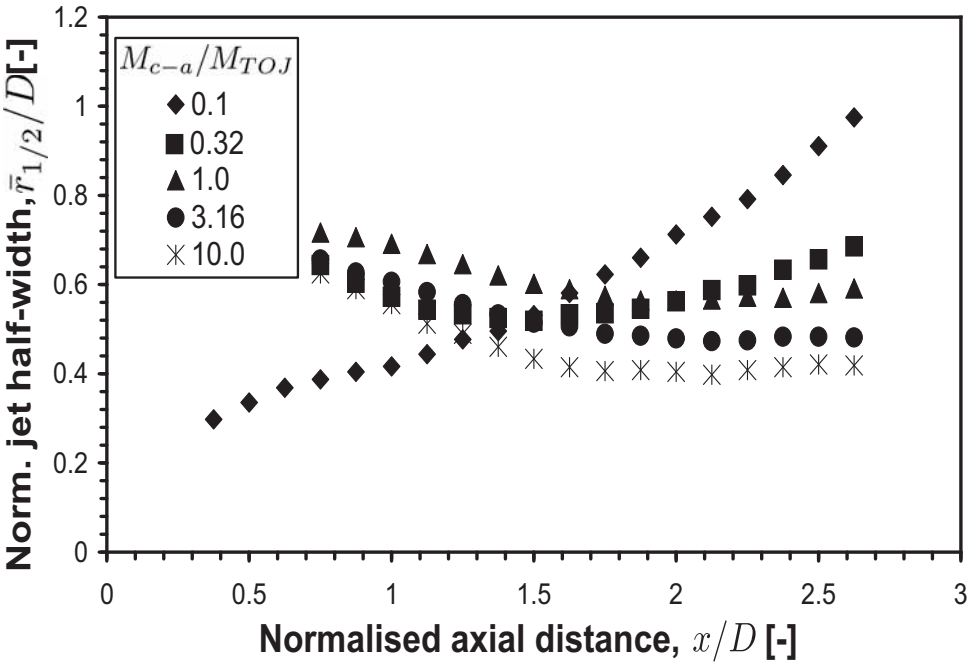

Figure 7.4: Mean half widths for the combined nozzle at various momentum ratios, M_{c-a}/M_{TOJ}, and density ratio, ρ_j/ρ_a=0.45.

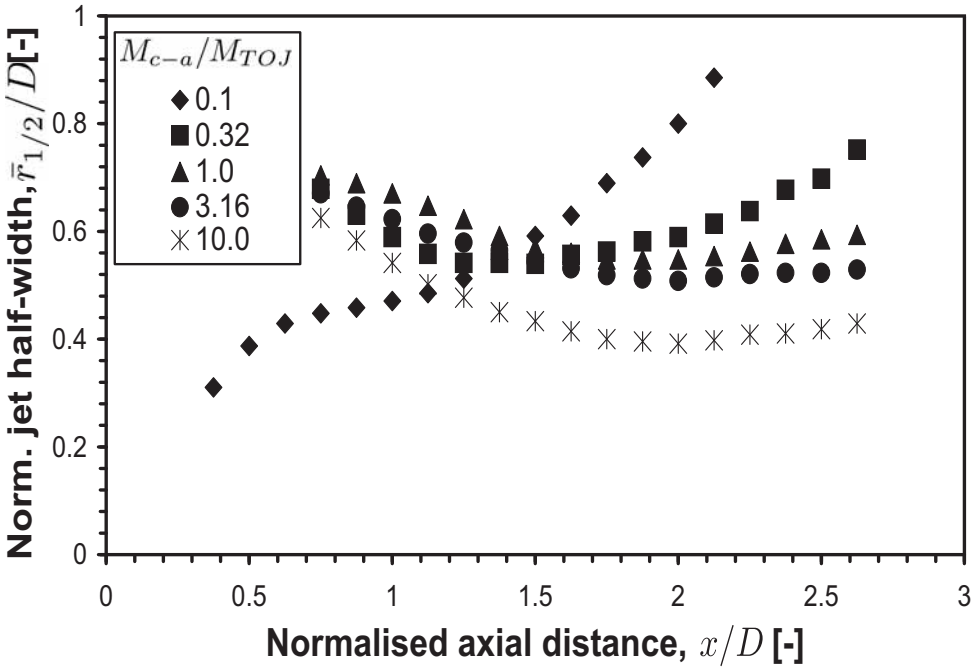

Figure 7.5: Mean half widths for the combined nozzle at various momentum ratios, M_{c-a}/M_{TOJ}, and density ratio, ρ_j/ρ_a=1.0.

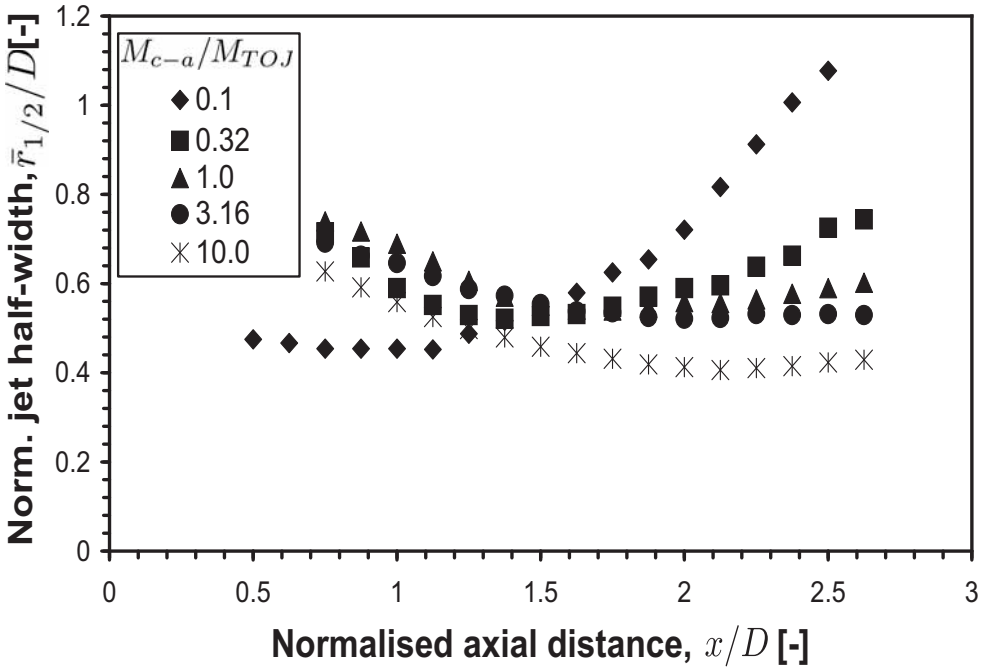

Figure 7.6: Mean half widths for the combined nozzle at various momentum ratios, M_{c-a}/M_{TOJ}, and density ratio, ρ_j/ρ_a=2.24.

TOJ to one that is dominated by the co-annular flow as was shown in figures 7.4, 7.5 and 7.6. However, within each figure the half widths are almost independent of ρ_j/ρ_a. This shows that the spread of the combined nozzle flow is insensitive to a change in ρ_j/ρ_a at any M_{c-a}/M_{TOJ}. Further evidence to support the results of figures 7.7, 7.8 and 7.9 is shown for $M_{c-a}/M_{TOJ} = 0.32$ and 3.16 in appendix C.

The insensitivity of the spread with respect to ρ_j/ρ_a suggests that the co-annular flow surrounding the TOJ provides a shielding effect, isolating the TOJ from the effects of density. This is certainly a plausible explanation for the insensitivity since the density ratio between the combined flow and the ambient surroundings, ρ_j/ρ_a, is variable, while the density ratio between the TOJ component of the flow and the co-annular component of the flow, ρ_{TOJ}/ρ_{c-a}, is always initially unity. Therefore, in the near field, the interaction between the TOJ and co-annular flow components is essentially, parametrically speaking, identical regardless of the density ratio between the combined flow and the ambient, ρ_j/ρ_a. There should however still be an effect of a change in density between the combined flow and the ambient surroundings similar to that observed for a simple jet. Figures 7.7,

7.8 and 7.9 do not show the trend as previously determined for variable density simple jets (Era and Saima, 1977; Richards and Pitts, 1993), but rather show only a small difference with no consistent trend.

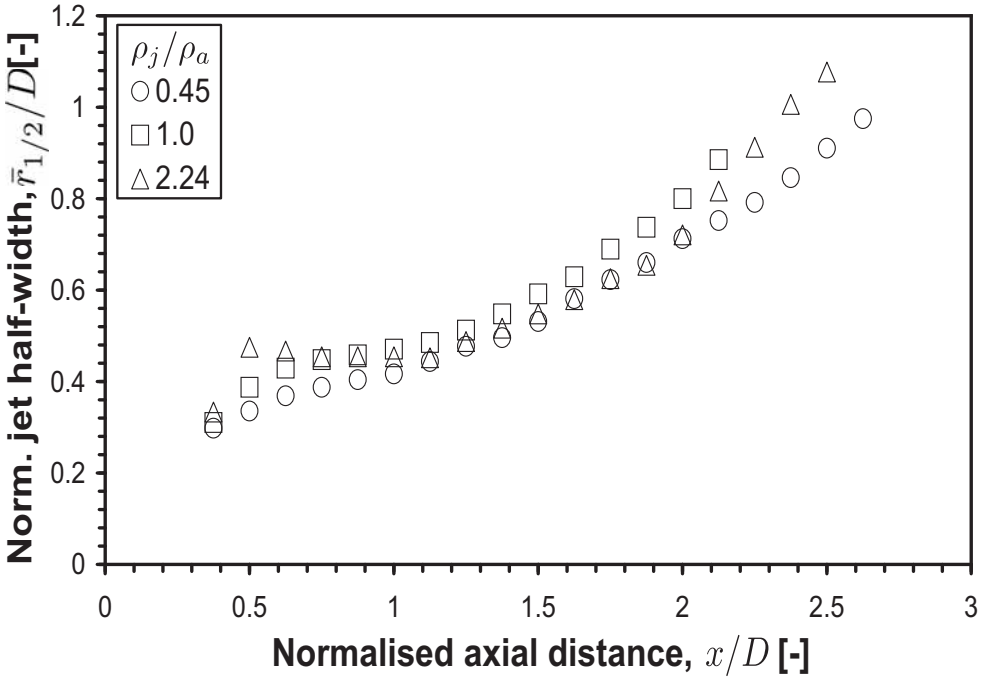

Figure 7.7: Mean half widths for the combined nozzle at various density ratio, ρ_j/ρ_a, and momentum ratio, M_{c-a}/M_{TOJ}=0.1.

Figures 7.10, 7.11 and 7.12 show the axial variation in the jet mean centreline velocity of the combined nozzle at momentum ratios, $M_{c-a}/M_{TOJ} = 0.1$, 1.0 and 10.0 respectively for all density ratios, ρ_j/ρ_a, investigated. Data are presented as an inverse velocity. These figures show that in each case the absolute value of the inverse velocity is higher, meaning greater jet decay, when ρ_j/ρ_a is lower. This trend is the same as that which has been previously established for simple jets (Era and Saima, 1977; Richards and Pitts, 1993) but is the opposite of that shown for the TOJ in the absence of the co-annular flow. This provides further evidence that the co-annular component of the combined nozzle flow is shielding the TOJ component from the effects of ρ_j/ρ_a. The same trend is also seen for $M_{c-a}/M_{TOJ} = 0.32$ and 3.16. The data for these cases are shown in appendix C.

The trend presented for the centreline decay agrees with the previously established trend for simple jets, indicating that the combined flow behaves more like

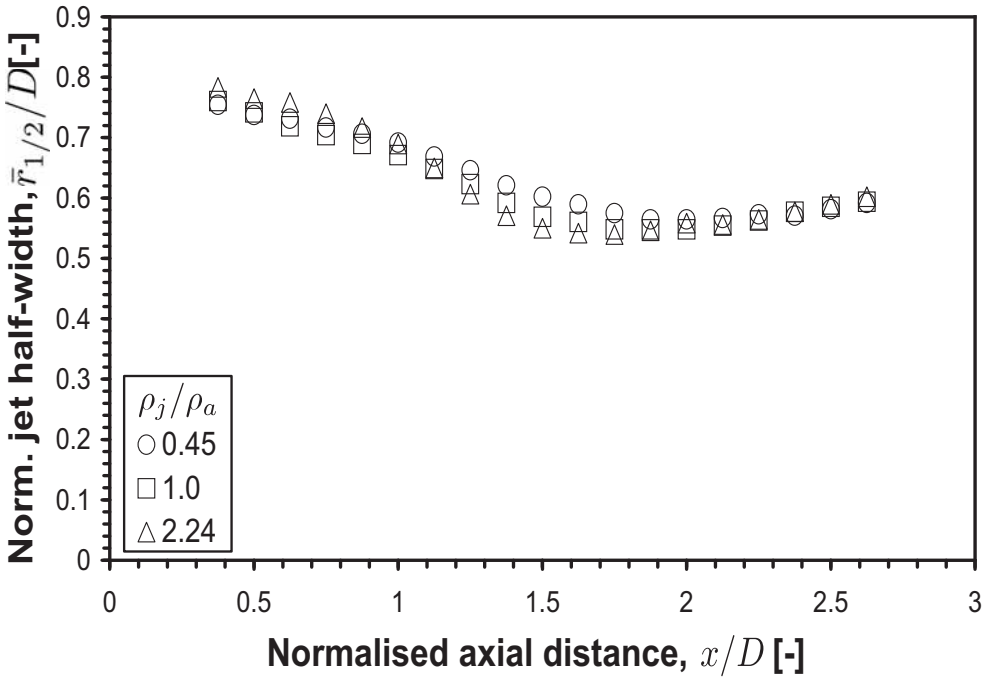

Figure 7.8: Mean half widths for the combined nozzle at various density ratio, ρ_j/ρ_a, and momentum ratio, M_{c-a}/M_{TOJ}=1.0.

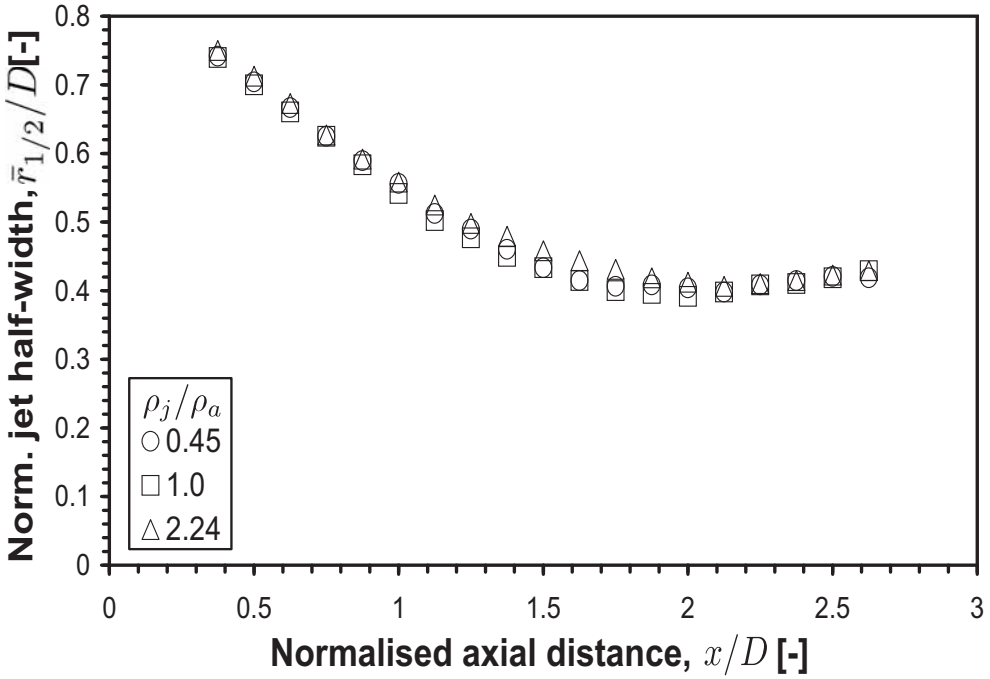

Figure 7.9: Mean half widths for the combined nozzle at various density ratio, ρ_j/ρ_a, and momentum ratio, M_{c-a}/M_{TOJ}=10.0.

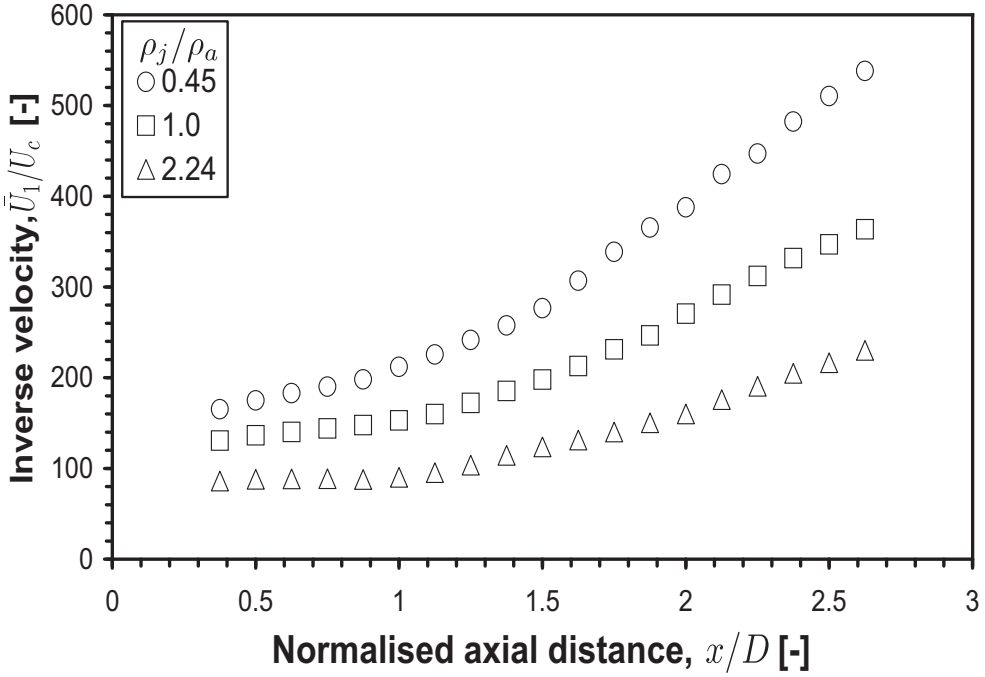

Figure 7.10: Centreline inverse velocity for the combined nozzle at various density ratios, ρ_j/ρ_a, and momentum ratio, M_{c-a}/M_{TOJ}=0.1.

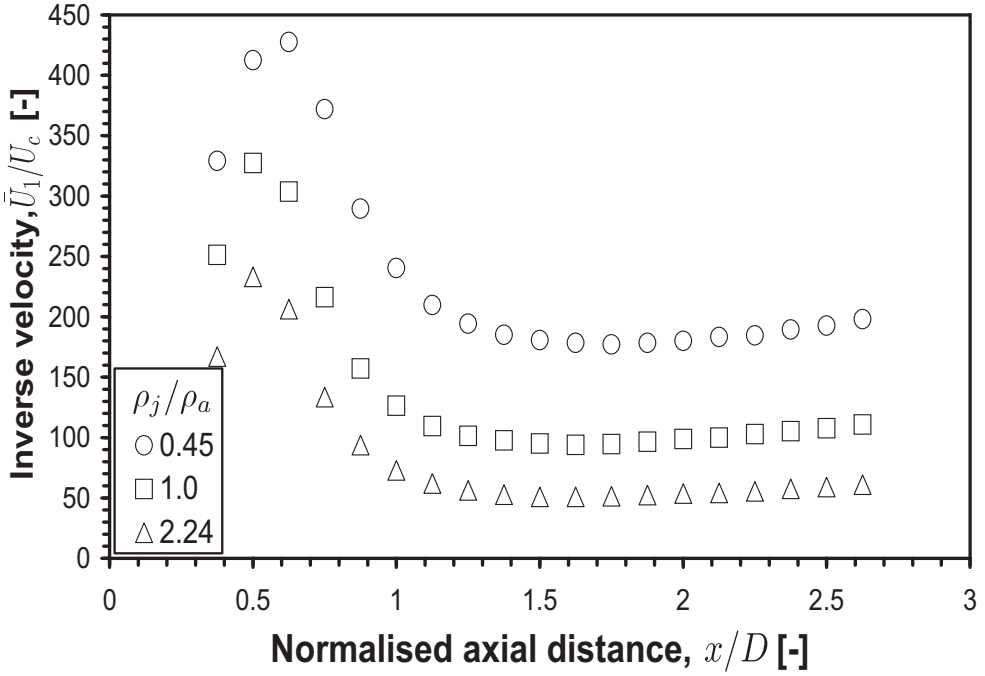

Figure 7.11: Centreline inverse velocity for the combined nozzle at various density ratios, ρ_j/ρ_a, and momentum ratio, M_{c-a}/M_{TOJ}=1.0.

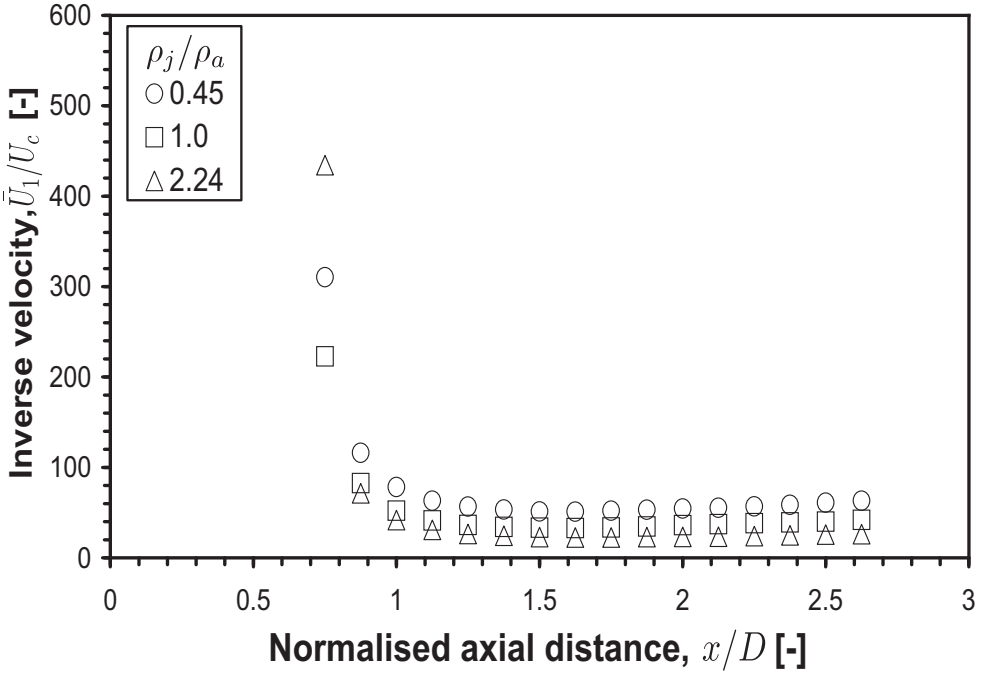

Figure 7.12: Centreline inverse velocity for the combined nozzle at various density ratios, ρ_j/ρ_a, and momentum ratio, M_{c-a}/M_{TOJ}=10.0.

a simple jet with the co-annular component shielding the TOJ component from the effects of ρ_j/ρ_a. However, with the shielding in place one would expect that the centreline velocity should converge to the same normalised value at the nozzle exit for all ρ_j/ρ_a, before deviating from one another with greater downstream difference. While there is no measured data that is closer to the nozzle exit than $x/D = 0.375$, it is clear from figures 7.10 and 7.11 that the normalised centreline velocities at the exit do not converge to a common value for $M_{c-a}/M_{TOJ} = 0.1$ and 1.0. While the data for $M_{c-a}/M_{TOJ} = 10.0$ does not show this due to the reverse flow in the near field due to the bluff body like recirculation of the co-annular flow, it can be assumed that a similar trend applies. This non-convergence of the exit centreline velocities implies that the decay within the TOJ nozzle chamber in each of the cases is different, with the decay being higher when ρ_j/ρ_a is lower. This difference in internal decay suggests that either, even in the near field, the effect of ρ_j/ρ_a is not totally shielded by the co-annular flow or there is another reason for the greater internal decay, which would be present with or without any shielding.

In each case the TOJ fluid is introduced at constant momentum flux. However the corresponding velocities, and hence Re, are significantly different. Deo et al (2008) have shown that the development of plane jets has a dependence on Reynolds number for Re $\leq 25.0 \times 10^3$. The Reynolds numbers for the current investigation are 11.2×10^3, 17.9×10^3 and 28.1×10^3 for $\rho_j/\rho_a = 0.45$, 1.0 and 2.24 respectively. These Reynolds numbers are certainly within the range for which a Reynolds number dependence can be expected. Deo et al (2008) show that the changes are associated with differences in the exit velocity profile and frequency spectra, implying different behaviour of the underlying coherent structures. They also show that an increase in Reynolds number leads to a decrease in the spreading and decay of the jet. Likewise, axisymmetric jets with low Reynolds number, but still fully turbulent, vary their spread inversely proportional to Reynolds number (Malmstrom et al, 1997). The results presented here show increased decay at lower Reynolds number, and is therefore consistent with the findings in the literature. However, to confirm that the increased decay within the chamber is as a result of Reynolds number, a detailed parametric study of the flow within the chamber is required, and should be addressed in future studies.

Both the conditional averaging of the data and the probability density analysis use algorithms based on the local momentum to determine the instantaneous deflection angle of the TOJ. With the current data set, it is impossible to separate the component of the local momentum derived from the co-annular flow, from that derived from the TOJ flow. Therefore determination of the instantaneous deflection angle of the TOJ component of the combined flow is also impossible with the current data set.

Figure 7.13 shows the frequency power spectra for the combined flow at various M_{c-a}/M_{TOJ} with ρ_j/ρ_a=1.0. This is the output from the first pressure vs time trace as determined using the Burg Maximum Entropy method. Although four pressure vs time traces were collected, there are no qualitative differences in the behaviour, and this result is typical of all four pressure traces. It can be seen from this figure that as M_{c-a}/M_{TOJ} is increased the dominant frequency at which the TOJ flow component oscillates also increases. The same trend of increased oscillation frequency with increased M_{c-a}/M_{TOJ} also occurs at the other ρ_j/ρ_a

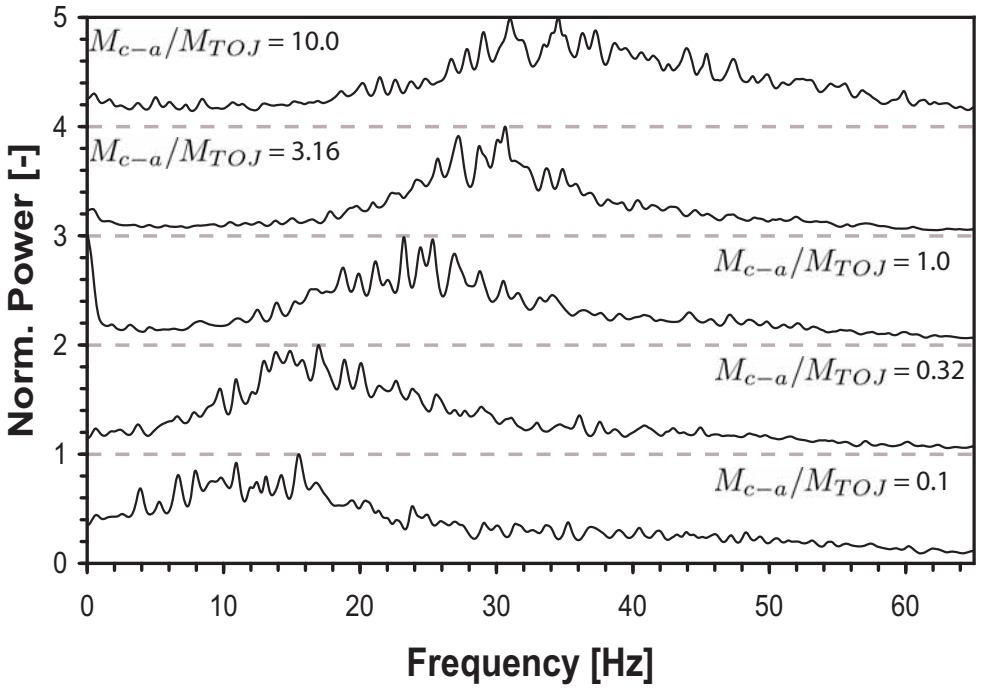

Figure 7.13: Frequency power spectra for all momentum ratios, M_{c-a}/M_{TOJ}, with ρ_j/ρ_a=1.0.

investigated, although the absolute value at each M_{c-a}/M_{TOJ} is different from that which is observed for ρ_j/ρ_a=1.0. The frequency power spectra for ρ_j/ρ_a= 0.45 and 2.24 can be seen in appendix C.

Figure 7.14 shows the oscillation frequency, f_{osc}, as a function of M_{c-a}/M_{TOJ} at all ρ_j/ρ_a investigated. There are two trends that this figure reveals. First, that regardless of ρ_j/ρ_a an increase in M_{c-a}/M_{TOJ} results, within measurement uncertainty, in an increase in f_{osc}. Second, that regardless of M_{c-a}/M_{TOJ} an increase in ρ_j/ρ_a results in a decrease in f_{osc}.

To understand the increase in f_{osc} that results from an increase in M_{c-a}/M_{TOJ}, one looks to the previous findings of Mi and Nathan (2004). They found that the magnitude of f_{osc} depends upon the internal axial momentum of the jet (M_x) and the angular momentum of the swirling fluid around the main jet (M_ϕ), and that increasing the ratio M_ϕ/M_x will result in greater f_{osc}. The swirling fluid that provides the angular momentum, M_ϕ, is comprised of both fluid from the main jet and fluid induced from outside the TOJ nozzle. Now the co-annular component of the flow without the TOJ component is essentially a bluff body

flow. Such a bluff body flow will, close to the nozzle on the nozzle axis, have a region of reverse flow due to the bluff body recirculation. It is deduced that this reverse flow caused by the bluff body recirculation enhances the amount of fluid entrained into the TOJ chamber, which results in an increase in M_ϕ and ultimately the ratio M_ϕ/M_x. Naturally the higher the value of M_{c-a}/M_{TOJ} the stronger the reverse flow will be. Therefore as M_{c-a}/M_{TOJ} is increased, M_ϕ will also increase, increasing the ratio M_ϕ/M_x resulting in a greater f_{osc}.

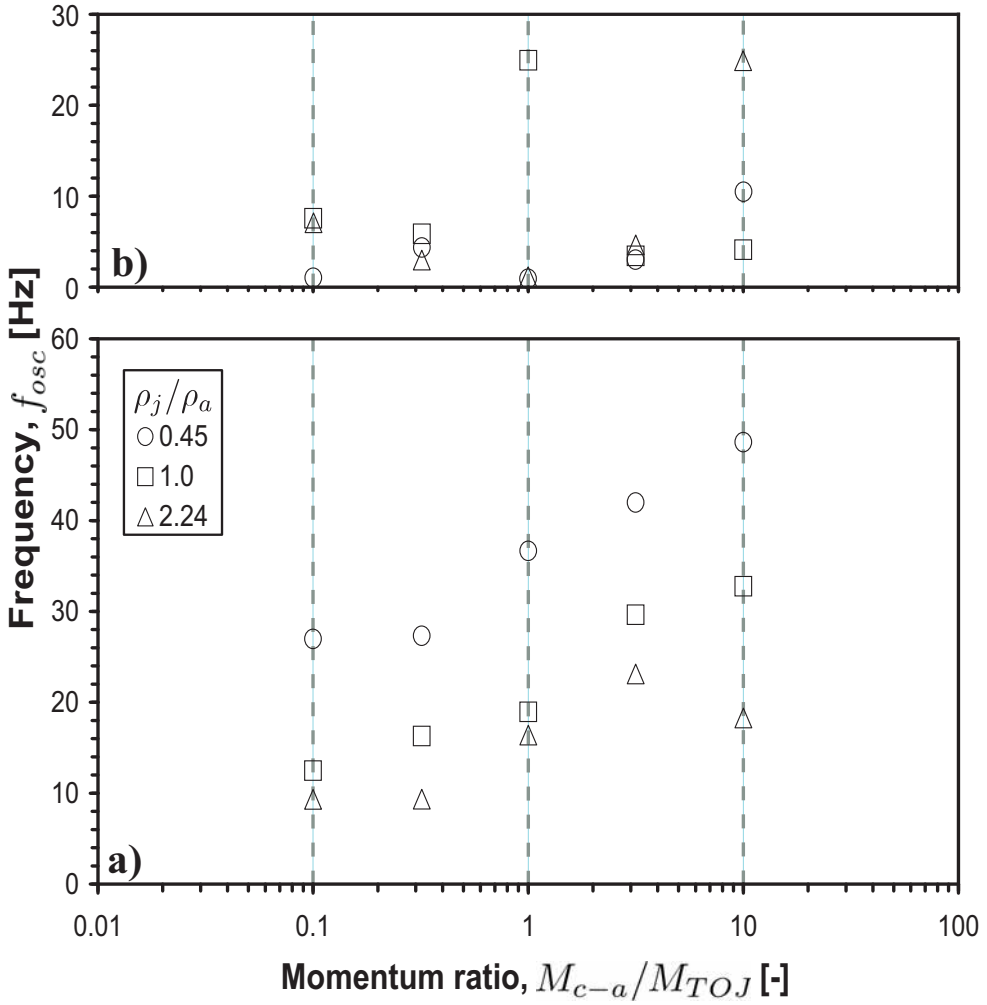

Figure 7.14: a) Oscillation frequency, f_{osc}, as a function of momentum ratio, M_{c-a}/M_{TOJ}, b) Measurement uncertainty.

The increase in f_{osc} observed when ρ_j/ρ_a is decreased is the same as the trend that was observed for the TOJ without the surrounding co-annular flow (Chapter 4). However, here the fluid entrained back into the chamber is expected to be

of a similar density to that entering the chamber via the triangular orifice due to the shielding effect of the co-annular flow. Therefore the change in f_{osc} is not significantly influenced by the change in ρ_j/ρ_a. The trend is however clear that regardless of M_{c-a}/M_{TOJ}, when ρ_j/ρ_a is higher f_{osc} is lower. With ρ_{TOJ}/ρ_{c-a} being unity in each case the only parameters that are obviously different are the initial velocities of the TOJ and co-annular flow, $\bar{U}_1$ and $\bar{U}_{c-a}$. Therefore, while a change in the ratio M_ϕ/M_x will result in a change in f_{osc}, it appears to be the initial velocity of the TOJ, not momentum flux, that determines the absolute value of f_{osc}, with higher initial velocity resulting in higher f_{osc}.

Higher initial velocity resulting in a higher f_{osc} is a result that can be explained using the definition of the Strouhal number. Using the Strouhal number definition, with fixed d_{e1}, f_{osc} and $\bar{U}_1$ must be proportional for a constant St_{osc}. Figure 7.15 shows the oscillation Strouhal number, St_{osc}, as a function of M_{c-a}/M_{TOJ} at all ρ_j/ρ_a investigated. This figure shows that, within the measurement uncertainty, at each M_{c-a}/M_{TOJ} the Strouhal number, St_{osc}, can be considered as a constant, confirming that the initial velocity of the TOJ, and not momentum flux, controls the absolute value of f_{osc}.

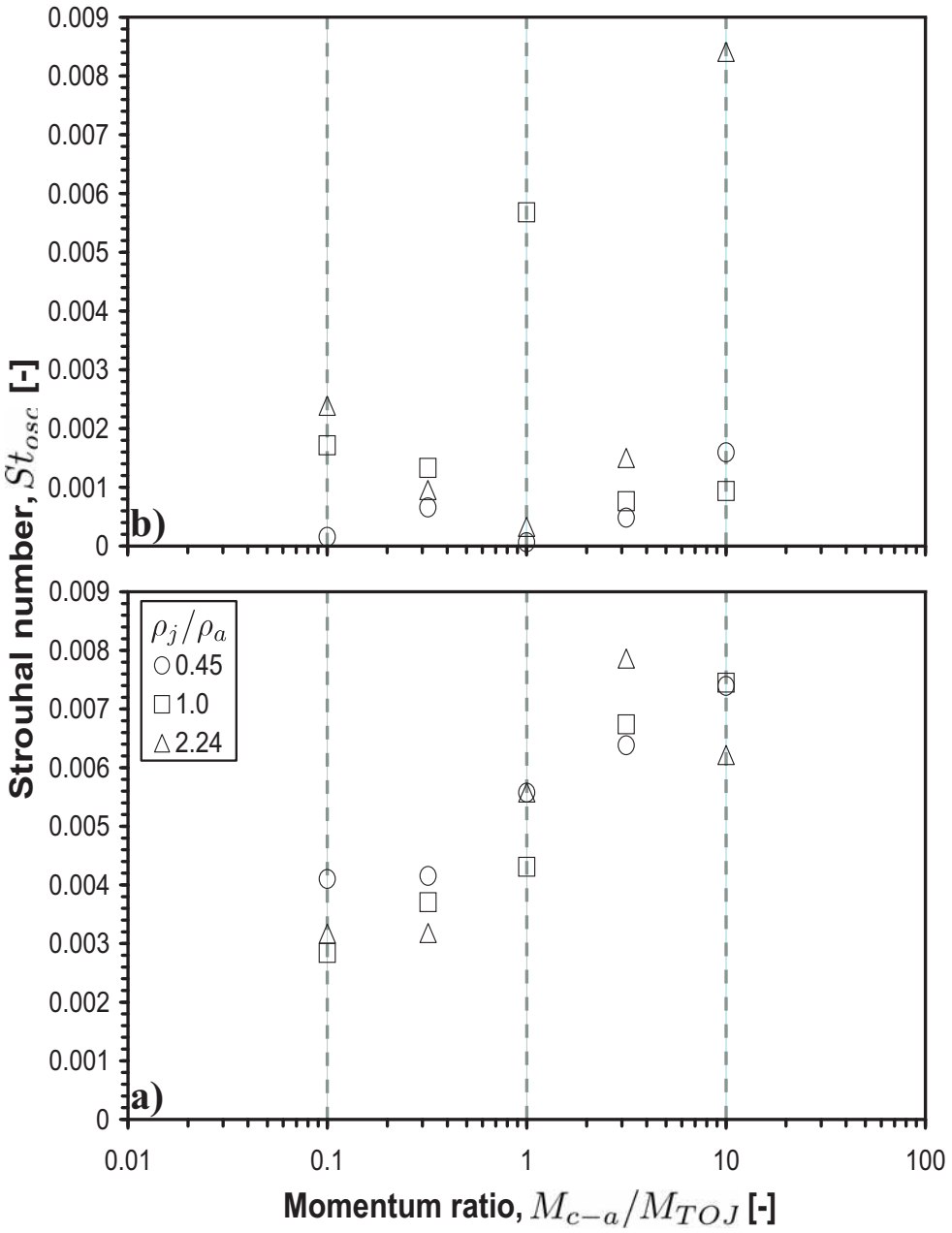

Figure 7.15: a) Oscillation Strouhal number, St_{osc}, as a function of momentum ratio, M_{c-a}/M_{TOJ}, b) Measurement uncertainty.

7.3 Conclusions

Velocity measurements by PIV and pressure measurements of the oscillation frequency have been used to investigate the flow from a more practical design of the TOJ nozzle. This design surrounds the TOJ flow with a co-annular flow of equal density. The combined flow was investigated under variable density conditions at various co-annular to TOJ momentum ratios. Half-widths and centreline decay data at fixed ρ_j/ρ_a show that as the momentum ratio is increased the combined flow changes from one which is dominated by the TOJ, to one which is dominated by the co-annular component, resembling a bluff body flow. At fixed momentum ratio the half-widths show that the rate of spread is similar despite the difference in ρ_j/ρ_a. The centreline decay data are consistent with this although the data do show a slight increase in the decay rate at lower ρ_j/ρ_a, consistent with the findings in the literature. These results at fixed momentum ratio are deduced to be as a result of the co-annular component of the combined nozzle flow shielding the TOJ component from the effects of ρ_j/ρ_a that occur for the TOJ in isolation as shown previously shown in chapter 4.

While the rate of decay outside of the chamber may be similar despite ρ_j/ρ_a, the rate of decay within the chamber varied in an inverse relationship with ρ_j/ρ_a. However, the difference is unlikely to be due to ρ_j/ρ_a, since fluid entrained back into the chamber is expected to be similar in density due to the shielding provided by the co-annular flow. The differences can be explained by the indirect influence of jet Reynolds number, consistent with the trends from Deo et al (2008) and Malmstrom et al (1997) for free jets in that decay is increased at lower Re. Reynolds number effects will also be present in the unshielded data, and therefore confirming this relationship within the chamber is important. Therefore future studies could perform a detailed parametric study on the flow within the TOJ chamber.

Oscillation frequency measurements show, that regardless of momentum ratio, the frequency of oscillation is higher at lower ρ_j/ρ_a, consistent with the results of chapter 4. They also show that at a fixed ρ_j/ρ_a, increasing the momentum ratio, M_{c-a}/M_{TOJ}, results in an increase in the frequency of oscillation. This is due to the bluff body recirculation associated with the co-annular component of

the combined flow increasing the amount of fluid entrained back into the TOJ chamber. This increase in entrained fluid alters the ratio of angular to axial momentum within the chamber, which has previously been deduced to influence the frequency of oscillation.

With industrial designs likely to comprise of the TOJ flow surrounded by a co-annular flow, it is important to understand the effects of density on the combined flow. This work looked at one specific arrangement of such a design. Therefore extrapolating these results to differently scaled arrangements should be done with caution. However, the results showed that the present arrangement of the co-annular flow effectively shielded the TOJ flow from the effects of density on the spread and decay, with the effect on the combined flow being consistent with the trends shown in the literature for simple jets, although the absolute difference is small. This finding is important as it means that when designing a burner for an industrial application the effects of the density ratio between the nozzle fluid and the ambient can essentially be ignored providing that the TOJ and co-annular components of the nozzle flow are of the same density.

Chapter 8

Conclusions

8.1 Introduction

Combustion provides, and will continue in the foreseeable future to be, a major component of the world's energy supply. With increasing awareness of the need to improve efficiency and reduce harmful emissions, improved combustion technology is required. This thesis has focussed on the TOJ nozzle, a burner that has applications in, but not limited to, the cement and lime industry. Improving the understanding of this burner's operation allows it's design to be improved, with respect to efficiency and emission reduction, for future installations. This study has focussed on improving the understanding of the TOJ by investigating the effect varying density has on the resulting flow in the near field region. Four specific aims are addressed with the findings associated with each discussed below.

8.2 Results

To establish the relationship between density ratio and mean spread, centreline decay, instantaneous jet deflection angle and the oscillation Strouhal number

To address this aim the nozzle momentum flux was held constant while the density

ratio between the nozzle fluid and the ambient surroundings (ρ_j/ρ_a) was varied on a $\log_5$ scale between $\rho_j/\rho_a = 0.2$ and $\rho_j/\rho_a = 5.0$. Measurements showed that increasing ρ_j/ρ_a leads to an increase in the mean jet spread and centreline decay, a trend which, in the mean, is opposite to that of a simple axisymmetric jet. This is due to the oscillatory nature of the TOJ, and that at any instant the jet is deflected off the nozzle axis. It is shown that the instantaneous angle of deflection is strongly correlated with the mean jet spread.

Result of the mean jet spread and instantaneous angle of deflection show two distinct regimes. The first is over the range $\rho_j/\rho_a \leq 1.0$ and the second where $\rho_j/\rho_a \geq 1.0$. In the first regime a change in ρ_j/ρ_a was found to result in a significant change in the spread and deflection angle. However, in the second regime the spread and deflection angle are relatively insensitive to a change in ρ_j/ρ_a.

The frequency of oscillation has an inverse dependence on ρ_j/ρ_a. As is the case with the spread and deflection, this relationship is less sensitive at higher ρ_j/ρ_a. After converting the frequencies into a Strouhal number three regimes are revealed. The first, where $\rho_j/\rho_a \leq 0.67$, has a constant value of the Strouhal number at a comparatively high value. The second, where $\rho_j/\rho_a \geq 2.24$, has a constant Strouhal number at a comparatively low value. The third, where $0.67 < \rho_j/\rho_a < 2.24$, is a region of transition between the other two. As shown there are two identified regimes relating to the spread and jet deflection. Although the Strouhal number transition region partially straddles these regimes, it can be seen that high Strouhal number region corresponds to the regime where spread and deflection change significantly with ρ_j/ρ_a, while the low Strouhal number region corresponds to the regime where spread and deflection are relatively insensitive to changes in ρ_j/ρ_a.

Clearly the nozzle produces a flow which is azimuthally time dependent. However frequency simulations show that this time dependence is not truly periodic. The oscillatory nature of the flow is deduced not to result from a periodic oscillation, but rather to be comprised of a series of random flapping events between preferred alignments.

The effect of variation in ρ_j/ρ_a on the near field has been identified for constant momentum flux. Since the momentum flux is held constant the Reynolds number

is not. Work on the practical configuration of the nozzle showed that Reynolds number may affect the flow within the nozzle chamber. Therefore, the above findings could in part be attributed to the changing Reynolds number. However, since no data exists that correlates Reynolds number effects on the TOJ flow, separating any Reynolds number effects from the effects of ρ_j/ρ_a is not possible at present.

To determine the relationship between mean spread, centreline decay, instantaneous jet deflection angle, oscillation frequency number and the nozzle chamber length at several density ratios

To address this aim five density ratios, $\rho_j/\rho_a = 0.2$, 0.45, 1.0, 2.24 and 5.0, were investigated over a range of chamber lengths. Again the nozzle momentum flux was held constant. Measurements showed that increases in L/D resulted in an increase in the mean jet spread and centreline decay regardless of ρ_j/ρ_a. Although changes to the spread and decay became less sensitive to changes in L/D at larger L/D. As above the instantaneous jet deflection angle strongly correlates with the mean jet spread.

A previous study conducted by Lee et al (2003) determined a critical L/D, for $\rho_j/\rho_a = 1.0$, at which the instantaneous jet deflection was maximised. This critical L/D was $L/D = 2.50$. Examination of the deflection results of the current study do not identify a clear peak with a single critical L/D for $\rho_j/\rho_a = 1.0$. The difference are attributed to the difference in the measurement techniques, with the current technique believed to be more accurate and reliable.

Over the L/D range investigated, the critical L/D for all ρ_j/ρ_a was unable to be determined, since no clear maximum was identified. However, the instantaneous jet deflection data did reveal an interesting result for $\rho_j/\rho_a \geq 1.0$. The results show that for any L/D where all $\rho_j/\rho_a \geq 1.0$ are investigated, the jet deflection, and hence mean spread is relatively insensitive to a change in ρ_j/ρ_a.

Regardless of ρ_j/ρ_a, the oscillation frequency increases with an increase in L/D. This finding is consistent with the findings of Mi and Nathan (2004), who deduce that this is the result of changing the ratio of angular momentum to axial momentum within the nozzle chamber, with increasing this ratio resulting in an increase in the oscillation frequency. With all the momentum initially axial, it

is deduced that some of this initially axial momentum is converted to angular momentum due to spreading within the chamber causing internal recirculation. Logically greater spread corresponds to greater recirculation, and hence more angular momentum and an increase in the angular to axial momentum ratio. As L/D is increased more internal spread will occur which ultimately leads to an increase in the oscillation frequency.

To isolate the influence on the flow due to a change in the density ratio without a simultaneous change in the viscosity ratio

To address this aim ρ_j/ρ_a was varied while keeping the viscosity ratio, μ_j/μ_a, constant. The nozzle momentum flux was held constant at the same rate as above so that comparisons could be drawn between this data where μ_j/μ_a was fixed and the above data where μ_j/μ_a was not fixed. To give the best comparison possible ρ_j/ρ_a was varied over as much of the range presented above, with ρ_j/ρ_a between 0.52 and 3.44. Results of the mean jet spread and instantaneous jet deflection angle showed similar trends to those described above. Although these trends are within experimental uncertainty of each other, there is some difference in the observed values at comparable ρ_j/ρ_a. Whether this difference is just measurement uncertainty or is due to μ_j/μ_a is not clear from the spread and deflection data.

Like the spread and deflection data, the oscillation frequency data shows a trend that within measurement uncertainty is similar to that described above where μ_j/μ_a is not a constant. Similarly any observed differences at comparable ρ_j/ρ_a could just be measurement uncertainty, or it could be as the results of the difference in μ_j/μ_a.

The trend presented for the centreline decay is internally consistent with the trends presented for the spread and deflection. However, the difference in the observed value at comparable ρ_j/ρ_a, between the trend where μ_j/μ_a is constant and the trend where μ_j/μ_a was not constant cannot be explained by measurement uncertainty. Therefore, the near field flow from the TOJ is affected by changes in both μ_j/μ_a and ρ_j/ρ_a. With no literature that describes the effects of changing μ_j/μ_a, even for simple jets, and the data presented in appendix B, where μ_j/μ_a was varied at constant ρ_j/ρ_a, revealing no consistent trend, separating the effects of ρ_j/ρ_a from those of μ_j/μ_a is not yet possible.

To assess the effectiveness of a practical configuration of an industrial burner with respect to changes in the density ratio

To address this aim three density ratios, namely ρ_j/ρ_a = 0.45, 1.0 and 2.24, were investigated with a surrounding co-annular flow. The density of the TOJ and co-annular flows was identical. The momentum flux of the TOJ flow was kept constant while the momentum ratio between the co-annular and TOJ flows was varied between 0.1 and 10.0. As the momentum ratio was increased the combined flow was found to transition from one which is dominated by the TOJ to one dominated by the co-annular flow resembling a bluff body flow.

Results showed that at a fixed momentum ratio, the mean spread of the combined nozzle flow was relatively insensitive to a change in ρ_j/ρ_a. However the change that was observed was consistent with that of simple jets rather than as previously described for the TOJ flow, in that a decrease in ρ_j/ρ_a lead to an increase in the mean jet spread. The results of the centreline decay was consistent with this finding. These findings indicate that by surrounding the TOJ flow with a co-annular flow of equal density, regardless of the momentum ratio between them, the effects of ρ_j/ρ_a on the TOJ previously described are shielded against.

Investigation of the centreline decay data also showed some difference between the decay within the TOJ chamber when ρ_j/ρ_a was varied. The trend was such that at lower ρ_j/ρ_a the decay within the chamber was greater. Since the co-annular flow shields the TOJ from the effects of ρ_j/ρ_a this change in the decay is not attributed to the change in ρ_j/ρ_a. Instead the change in decay is attributed to the difference in the Re of the TOJ flow, which change varies with ρ_j/ρ_a since the TOJ momentum flux is held constant. Therefore an increase in Re results in a decrease in the decay. This trend is consistent with trends from the literature for simple jets.

Oscillation frequency measurements show that at constant ρ_j/ρ_a, increasing the momentum ratio leads to an increase in the oscillation frequency. As is the case with a change in L/D this is due to a change in the angular to axial momentum ratio within the TOJ chamber. However, unlike for a change in L/D, the change in the angular to axial momentum ratio is not due to a change in the spread within the chamber but rather the change in recirculation within the chamber caused by the bluff body recirculation in the exit region of the TOJ nozzle.

8.3 Industrial Implications

This study has looked at the effects of ρ_j/ρ_a over the range $0.2 \leq \rho_j/\rho_a \geq 5.0$. However, the density ratios expected to occur in most applications are $\rho_j/\rho_a > 1.0$. Result presented for the TOJ under variable density conditions show that the spread, decay, and instantaneous deflection are insensitive to changes in ρ_j/ρ_a when $\rho_j/\rho_a \geq 1.0$. In this same ρ_j/ρ_a range the Strouhal number is constant when $\rho_j/\rho_a \geq 2.24$ but begins to increase as ρ_j/ρ_a approaches 1.0 from above. This suggests that the effects of ρ_j/ρ_a can be ignored when designing a burner for these industrial applications.

When $\rho_j/\rho_a \geq 1.0$, at a fixed L/D, the observed spread, decay and instantaneous jet deflection is insensitive to changes in ρ_j/ρ_a. This means that when designing a nozzle one can selected the appropriate L/D for the desired spread knowing that changes in ρ_j/ρ_a will have only a minor impact on the resulting flow.

Industrial designs are most likely to be comprised of a setup similar to that used in the practical configuration investigation. Results of that investigation showed that the co-annular flow that then surrounds the TOJ flow essentially shields the TOJ flow from the effects of ρ_j/ρ_a even when $\rho_j/\rho_a < 1.0$. However, this has only been shown when the density of the co-annular flow is the same as that of the TOJ flow. The fact that the co-annular flow shields the TOJ from the effects of ρ_j/ρ_a means that the effects of ρ_j/ρ_a become negligible and can therefore be ignored when designing this type of nozzle for most, if not all, industrial applications.

8.4 Future Work

This work has highlighted the need for further work in several areas.

The investigation on the practical configuration showed a potential dependence of the flow within the nozzle chamber on Re. Since the external flow is directly dependent on the flow within the nozzle chamber, knowledge of the relationship between the flow and Re is important for design purposes. This relationship is currently unknown and should therefore be addressed.

While investigate the effects of changing L/D at various ρ_j/ρ_a, the critical L/D was not determined at any of the investigated ρ_j/ρ_a. Knowledge of the critical L/D would be useful for industrial design purposes. Therefore future work should extend this investigation by broadening the L/D range investigated to determine the critical L/D.

This work showed that ρ_j/ρ_a is not the only fluid property that influences the TOJ flow. Viscosity ratio was also shown to have an effect. However, no relationships between μ_j/μ_a and measured quantities such as mean spread and decay were not determined. Therefore future work should investigate the effects of μ_j/μ_a on the TOJ flow to determine these relationships. Such a study should also be conducted on a simple jet as there is a lack of material in the published literature on the topic.

Bibliography

Adrian R (1997) Dynamic ranges of velocity and spatial resolution of particle image velocimetry. Measurement Science and Technology 8:1393–1398

Aggarwal S (1994) Relationship between Stokes number and intrinsic frequencies in particle-laden flows. AIAA Journal 32(6):1322–1325

Amielh M, Djeridane T, Anselmet F, Fulachier L (1996) Velocity near-field of variable density turbulent jets. International Journal of Heat and Mass Transfer 39(10):2149–2164

Bauer C (1990) Pyro-jet burners to reduce NOx emissions - current developments and practical experience. World Cement pp 118–124

Boateng A (2008) Rotary kilns: transport phenomena and transport processes. Elsevier

Borman GL, Ragland KW (1998) Combustion Engineering, International edn. The McGraw-Hill Companies, Inc.

Bowman C (1992) Control of combustion generated nitrogen oxide emissions: Technology driven by regulation. 24th Symposium (International) on Combustion/The Combustion Institute pp 859–878

Brown G, Roshko A (1974) On density effects and large structure in turbulent mixing layers. Journal of Fluid Mechanics 64(4):775–816

Chen C, Rodi W (1980) Vertical turbulent buoyant jets - A review of experimental data. Pergamon Press Ltd

Cuevas-Cubria C, Riwoe D (2006) Australian energy: national and state projections to 2029-30. Tech. rep., Australian Bureau of Agricultural and Resource Economics

Davison J, Freund P, Smith A (2001) Putting carbon back into the ground. Tech. rep., IEA Greenhouse Gas R and D Programme

Dellenback PA, Metzger DE, Neitzel G (1988) Measurements in turbulent swirling flow through an abrupt axisymmetric expansion. AIAA Journal 26(6):669–681

Deo R, Mi J, Nathan G (2008) The influence of Reynolds number on a plane jet. Physics of Fluids 20

Deussner M (1995) Clinker burning with reduced NOx emission. World Cement pp 52–58

Di Giancinto M, Sabetta F, Piva R (1982) Two-way coupling effects in dilute gas-particle flows. Transactions of the ASME 104:304–312

Dusome D (1995) Staged combustion for NOx control at the calaveras tehachapi plant. World Cement

Eaton J, Fessler J (1994) Preferential concentration of particles by turbulence. International Journal of Multiphase Flow 20:169–209

Era Y, Saima A (1977) Turbulent mixing of gases with different densities. Bulletin of the JSME 20(139):63–70

Fan J, Zhang L, Zhao H, Cen K (1990) Particle concentration and particle size measurements in a particle laden turbulent free jet. Experiments in Fluids 9:320–322

Fan J, Zhao H, Cen K (1996a) Particle concentration and size measurements in two-phase turbulent coaxial jets. Chemical Engineering Communications 156:115–129

Fan J, Zhao H, Jin J (1996b) Two-phase velocity measurements in particle-laden coaxial jets. The Chemical Engineering Journal 63:11–17

Fessler J, Kulick J, Eaton J (1994) Preferential concentration of heavy particles in a turbulent channel flow. Physics of Fluids 6(11):3742–3749

Fulkerson W, Judkins R, Sanghvi M (1990) Energy from fossil fuels. Scientific American pp 83–89

Hallet WLH, Gunther R (1984) Flow and mixing in swirling flow in a sudden expansion. Canadian Journal of Chemical Engineering 62:149–155

Hill SJ, Nathan GJ, Luxton RE (1992) Precessing and axial flows following a sudden expansion in an axisymmetric nozzle. Eleventh Australasian Fluid Mechanics Conference, University of Tasmania, Hobart, Australia

Hill SJ, Nathan GJ, Luxton RE (1995) Precession in axisymmetric confined jets. Twelfth Australasian Fluid Mechanics Conference, University of Sydney, Sydney, Australia

Huang H, Dabiri D, Gharib M (1997) On errors of digital particle image velocimetry. Measurement science and technology 8:1427–1440

IPCC (2007) Climate change 2007: Mitigtion of climate change. Tech. rep., Intergovernmental Panel on Climate Change

Kato SM, Groenewegen BC, Breidenthal RE (1987) Turbulent mixing in non-steady jets. AIAA Journal 25(1):165–168

Kay S, Marple S (1981) Spectrum analysis - a modern perspective. Proceedings of the IEEE 69(11):1380–1419

Kulik J, Fessler J, Eaton J (1994) Particle response and turbulence modification in fully developed channel flow. Journal of Fluid Mechanics 277:109–134

Landers T, Lacoss R (1977) Some geophysical applications of autoregressive spectral estimates. IEEE Transaction Geoscience Electronics GE15:26–32

Larson M, Jonsson L (1995) Modeling of mixing by turbulent jet in stably stratified fluid. Journal of Hydraulic Engineering 121(12):853–862

Law AK, Herlina (2002) An experimental study on turbulent circular wall jets. Journal of Hydraulic Engineering 128(2):161–174

Lee SK, Lanspeary PV, Nathan GJ, Kelso RM, Mi J (2003) Low kinetic-energy loss oscillating-triangular-jet nozzles. Experimental Thermal and Fluid Science 27:553–561

Longmire EK, Eaton JK (1992) Structure of a particle-laden round jet. Journal of Fluid Mechanics 236:217–257

Malmstrom T, Kirkpatrick A, Christensen B, Knappmiller K (1997) Centreline velocity decay measurements in low-velocity axisymmetric jets. Journal of Fluid Mechanics 246:363–377

Manias CG, Nathan GJ (1993) The precessing jet gas burner - a low NOx burner providing process efficiency and product quality improvements. World Cement pp 4–11

McQueen A, Bortz S, Hatch M, Leonard R (1995) Cement kiln NOx control. IEEE Transactions on Industry Applications 31(1):36–43

Megalos NP, Smith NL, Zhang DK (2001) The potential for low NOx from a precessing jet burner. Combustion and Flame 124:50–64

Melling A (1997) Tracer particles and seeding for particle image velocimetry. Measurement science and technology 8:1406–1416

Mi J, Nathan G (2005) Statistical analysis of the velocity field in a mechanical precessing jet flow. Physics of Fluids 17

Mi J, Nathan GJ (2001) Scalar mixing characteristics of a self-excited flip-flop jet nozzle. 14th Australasian Fluid Mechanics Conference, Adelaide University, Adelaide, Australia

Mi J, Nathan GJ (2004) Self-excited jet-precession strouhal number and its influence on turbulent mixing characteristics. Journal of Fluids and Structures 19:851–862

Mi J, Luxton RE, Nathan GJ (1998) The mean flow field of a precessing jet. Thirteenth Australasian Fluid Mechanics Conference, Monash University, Melbourne, Australia

Morris GJ, Jurewicz JT, Palmer GM (1992) Gas-solid flow in a fluidically oscillating jet. Transactions of the ASME: Journal of Fluids Engineering 114:362–366

Mullinger P (1994) Cement kiln firing and clear air requirements. World Cement pp 27–29

Nathan G, Luxton R (1991) Flame stability and emission characteristics of the enhanced mixing burner. 2nd European Confence on Industrial Furnaces and Boilers, Portugal

Nathan G, Manias C (1995) The role of process and flame interaction in reducing nox emissions. Combustion and Emissions Control pp 309–318

Nathan G, Luxton R, Smart J (1992) Reduced NOx emissions and enhabced large sacle turbulence from a precessing jet burner. 24th Symposium (International) on Combustion/The Combustion Instituite pp 1399–1405

Nathan G, Brumale S, Proctor D, Luxton R (1993) NOx reduction in flames by modification of turbulence with jet precession. Combustion and Emissions Control

Nathan G, Smith N, Mullinger P, Smart J (2000) Performance characteristics of, and an aerodynamic scaling parameter for, a practical pf burner design employing jet excitation to promote particle clustering. 5th International Conference on Industrial Furnaces and Boilers, Porto, Portugal

Nathan GJ (1988) The enhanced mixing burner. PhD thesis, Department of Mechanical Engineering, University of Adelaide, Australia

Nathan GJ, Hill SJ (2002) Full scale assesment of the influence of a precessing jet of air on the performance of pulverised coal flame in a cement kiln. FCT Internal Report

Nathan GJ, Turns SR, Bandaru RV (1996) The influence of fuel jet precession on the global properties and emissions of unconfined turbulent flames. Combustion Science and Technology 112:211–230

Nathan GJ, Hill SJ, Luxton RE (1998) An axisymetric 'fluidic' nozzle to generate jet precession. Journal of Fluid Mechanics 370:347–380

Newbold GJR (1998) Mixing and combustion in precessing jet flows. PhD thesis, Department of Mechanical Engineering, University of Adelaide, Australia

Newbold GJR, Nathan GJ (1999) The influence of changes to mixing on the sooting and NOx emission characteristics of unconfined turbulent jet diffusion flames. Developments in Chemical Engineering and Mineral Processing 7(3):361–374

Parham JJ, Nathan GJ, Smart JP, Hill SJ, Jenkins BG (2000) The relationship between heat flux and NOx emissions in gas-fired rotary kilns. Journal of the Institute of Energy 73:25–34

Pietri L, Gharbi A, Amielh M, Anselmet F (1998) Estimation of velocity in variable density jets using laser-doppler anemomerty. Experimental Thermal and Fluid Science 17:107–115

Pitts W (1991) Effects of global density ratio on the centreline mixing behavior of axisymmetric turbulent jets. Experiments in Fluids 11:125–134

Prathner M, Logan J (1994) Combustion's impact on the global atmosphere. 25th Symposium (International) on Combustion/The Combustion Institute pp 1513–1527

Raffel M, Willert C, Kompenhans J (1998) Particle Image Velocimetry - A Practical Guide. Springer

Raman G, Cornelius D (1994) Jet mixing control using excitation from miniature oscillating jets. AIAA Journal 33(2):365–368

Raman G, Hailye M, Rice EJ (1993) Flip-flop jet nozzle extended to supersonic flows. AIAA Journal 31(6):1028–1035

Raman G, Rice EJ, Cornelius DM (1994) Evaluation of flip-flop jet nozzles for use as practical excitation devices. Transactions of the ASME: Journal of Fluids Engineering 116:508–515

Richards CD, Pitts WM (1993) Global density effects on the self-preservation behaviour of turbulent free jets. Journal of Fluid Mechanics 254:417–435

Ricou FP, Spalding DB (1961) Measurements of entrainment by axisymmetrical turbulents jets. Journal of Fluid Mechanics 11:21–32

Ruffin E, Schiestel R, Anselmet F, Amielh M, Fulachier L (1994) Investigation of characteristic scales in variable density turbulent jets using a second-order model. Physics of Fluids 6(8):2785–2799

Sautet J, Stepowski J (1998) Evolution of the effective nozzle diameter in the bouyancy free development of turbulent jets with variable density. Experiments in Fluids 25:280–282

Schneider G, Vidakovic S, Hooper J, Musgrove A, Nathan G, Luxton R (1993) Theoretical and experimental pressure field evaluation downstream of a mechanical precessing jet. 4th Australian Heat and Mass Transfer Conference, Brisbane

Schneider G, Hooper J, Musgrove A, Nathan G, Luxton R (1997) Velocity and Reynolds stresses in a precessing jet flow. Experiments in Fluids 22:489–495

Smart JP, Van de Kamp WL (1999) The impact of scaling criteria on the characteristics of pulverised coal flames. Developments in Chemical Engineering and Mineral Processing 7(3):301–331

Smith N, Nathan G (2001) The role of unsteadiness within a central jet on the structure of a combined central and co-annular jet flow. Fourteenth Australasian Fluid Mechanics Conference, Adelaide University, Adelaide, Australia

Smith NL, Megalos NP, Nathan GJ, Zhang DK, Smart JP (1998a) Precessing jet burners for stable and low NOx pulverised fuel flames - preliminary results from small-scale trials. Fuel 77(9/10):1013–1016

Smith NL, Megalos NP, Nathan GJ, Zhang DK, Smart JP (1998b) The role of fuel rich clusters in flame stabilisation and NOx emission reduction with precessing jet p.f. flames. 27th International Symposium of Combustion, Colorado, USA

Smith NL, Nathan GJ, Zhang DK, Nobes DS (2002) The significance of particle clustering in pulverised coal flames. 29th Symposium (International) on Combustion

Sreenivasan K, Raghu S, Kyle D (1989) Absolute instability in variable density round jets. Experiments in Fluids 7:309–317

Stepowski D, Sautet J (2003) Measurement of the turbulent diffusivity in the near field of variable density jet using conditional velocimetry. Experiments in Fluids 35:397–407

Viets H (1975) Flip-flop jet nozzle. AIAA Journal 13(10):1375–1379

Wall T (2006) Combustion processes for carbon capture. Proceedings of 31st International Symposium on Combustion, University of Heidelberg

Westerweel J (1994) Efficient detection of spurious vectors in particle image velocimetry data. Experiments in Fluids 16:236–247

Westerweel J (1997) Fundamentals of digital particle image velocimetry. Measurement science and technology 8:1379–1392

Westerweel J, Scarano F (2005) Universal outlier detection for PIV data. Experiments in Fluids 39:1096–1100

Westerweel J, Draad AA, van der Hoeven J, van Oord J (1996) Measurement of fully-developed turbulent pipe flow with digital particle image velocimetry. Experiments in Fluids 20:165–177

Willert C, Gharib M (1991) Digital particle image velocimetry. Experiments in Fluids 10:181–193

Wong C (2004) The flow within and in the near external field of a fluidic precessing jet nozzle. PhD thesis, Department of Mechanical Engineering, University of Adelaide, Australia

Wong CY, Lanspeary PV, Nathan GJ, Kelso RM, O'Doherty T (2001) Phase averaged velocity field within a fluidic precessing jet nozzle. Fourteenth Australasian Fluid Mechanics Conference, Adelaide University, Adelaide, Australia pp 809–812

Wong CY, Nathan GJ, O'Doherty T (2002) The effect of different initial conditions on the exit flow from a fluidic precessing jet nozzle. 11th International

Symposium of Applications of Laser Techniques to Fluid Mechanics, Lisboa, Portugal

Wünning JA, Wünning JG (1997) Flameless oxidation to reduce thermal NO-formation. Progress in Energy Combustion and Science 23:81–94

Appendix A

Additional Variable L/D Figures

This appendix shows additional figures for the TOJ with L/D varied.

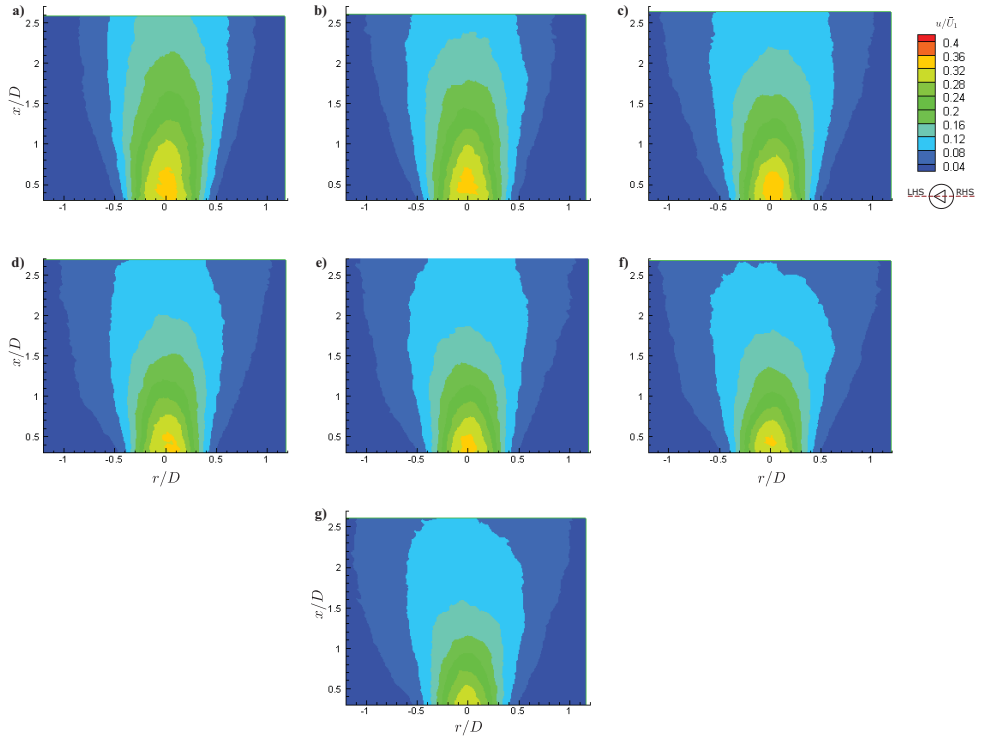

Figure A.1: Axial velocity component of the ensemble averaged flow fields, $u/\bar{U}_1$, with density ratio, ρ_j/ρ_a=0.45, for L/D= a) 2.11, b) 2.21, c) 2.30, d) 2.40, e) 2.49, f) 2.58 and g)2.68.

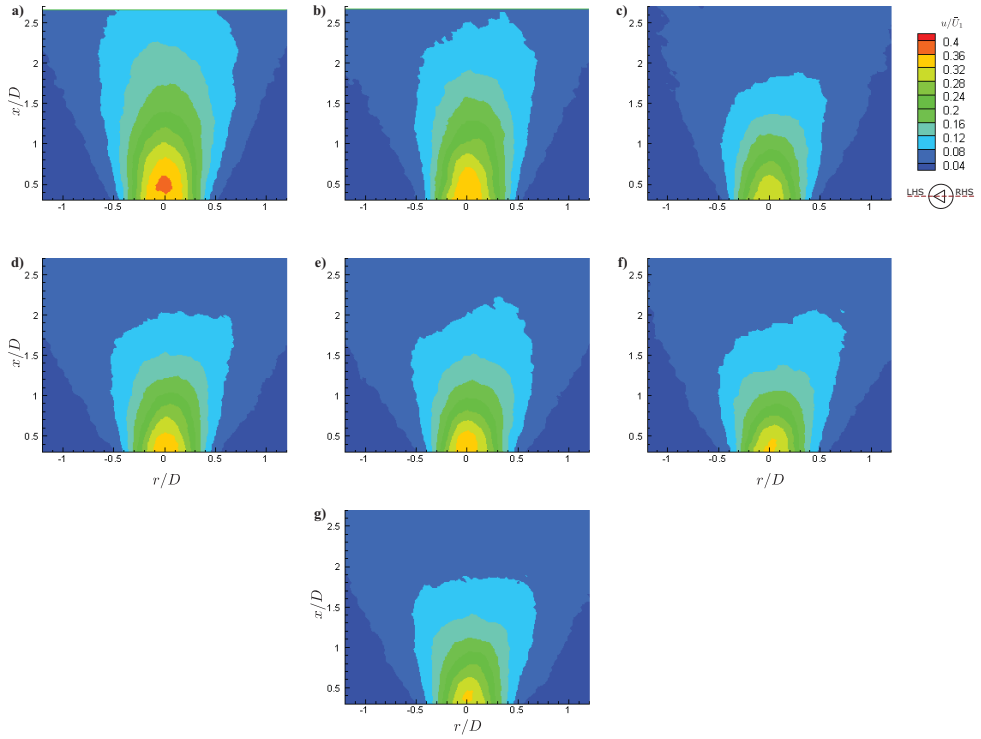

Figure A.2: Axial velocity component of the ensemble averaged flow fields, $u/\bar{U}_1$, with density ratio, ρ_j/ρ_a=2.24, for L/D= a) 2.30, b) 2.40, c) 2.49, d) 2.58, e) 2.68, f) 2.77 and g)2.87.

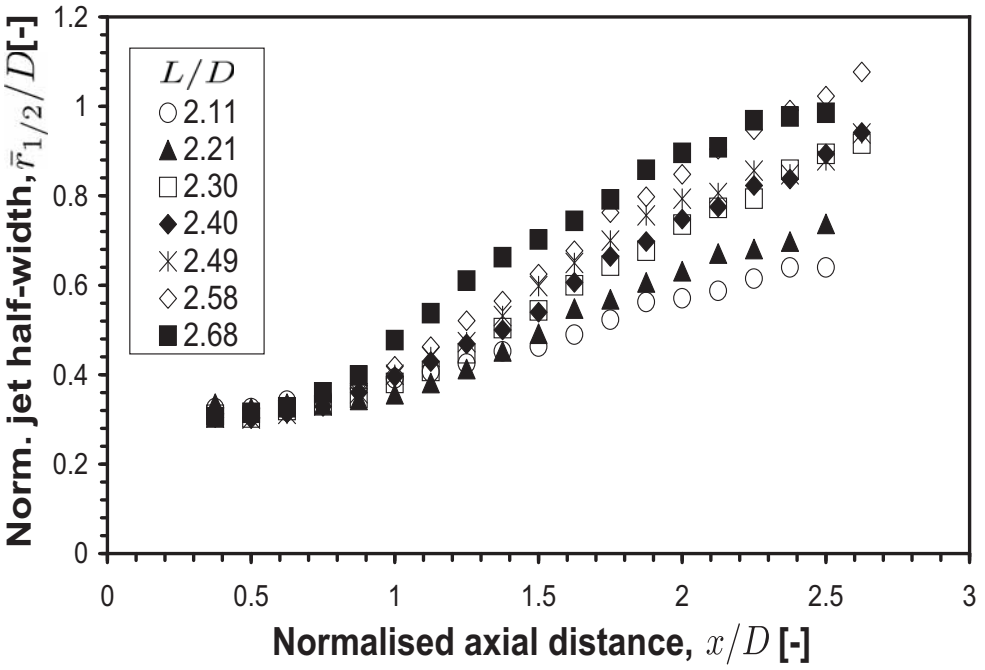

Figure A.3: Mean half widths for the TOJ nozzle at various L/D with ρ_j/ρ_a=0.45.

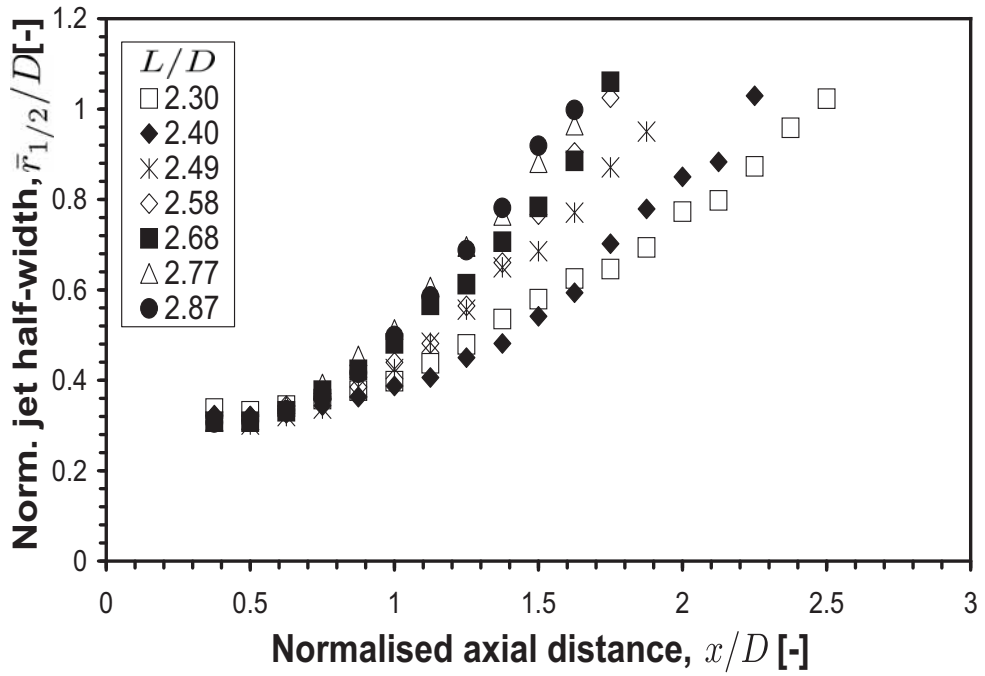

Figure A.4: Mean half widths for the TOJ nozzle at various L/D with ρ_j/ρ_a=2.24.

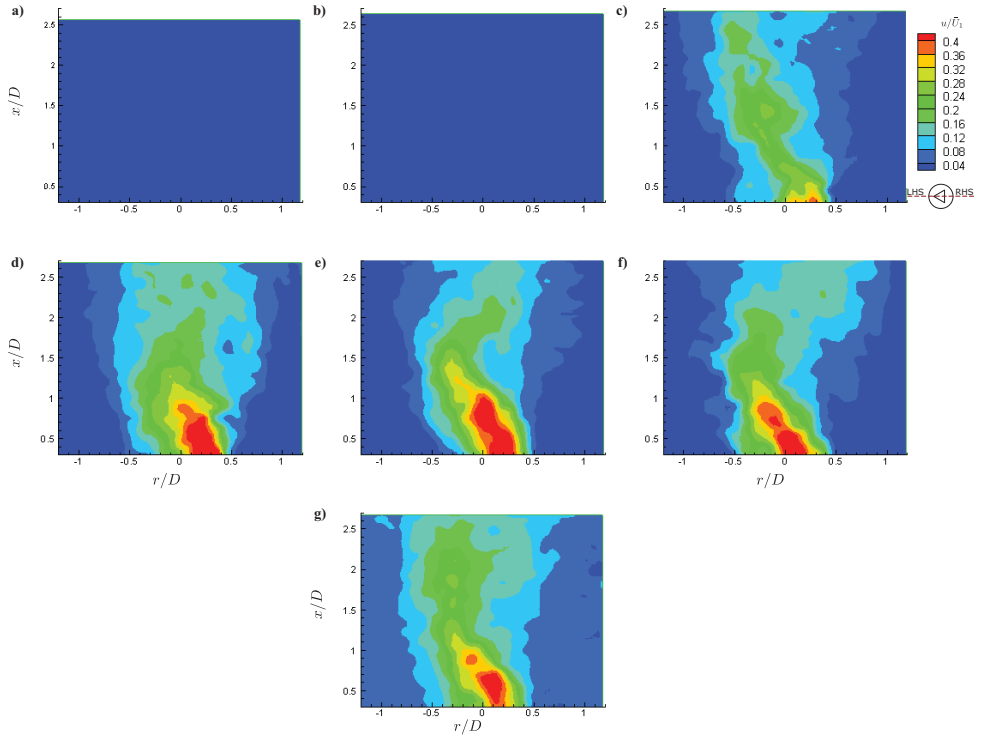

Figure A.5: Axial velocity component of the conditionally averaged flow fields, $u/\bar{U}_1$, with density ratio, ρ_j/ρ_a=0.2, for L/D= a) 2.02, b) 2.11, c) 2.21, d) 2.30, e) 2.40, f) 2.49 and g)2.58.

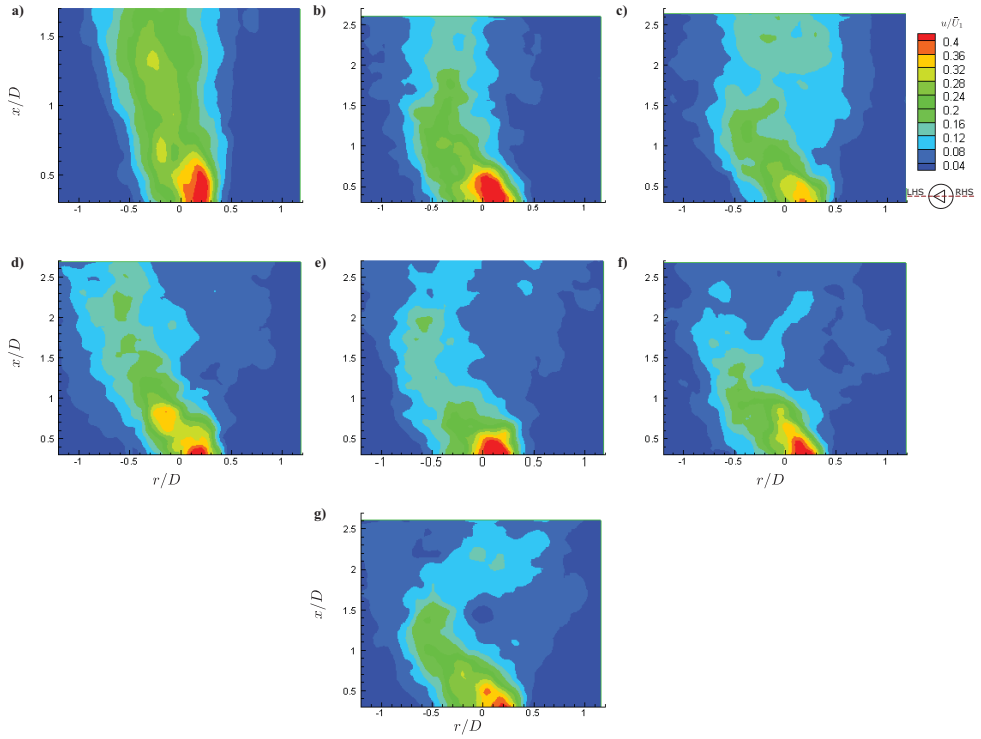

Figure A.6: Axial velocity component of the conditionally averaged flow fields, $u/\bar{U}_1$, with density ratio, ρ_j/ρ_a=0.45, for L/D= a) 2.11, b) 2.21, c) 2.30, d) 2.40, e) 2.49, f) 2.58 and g)2.68.

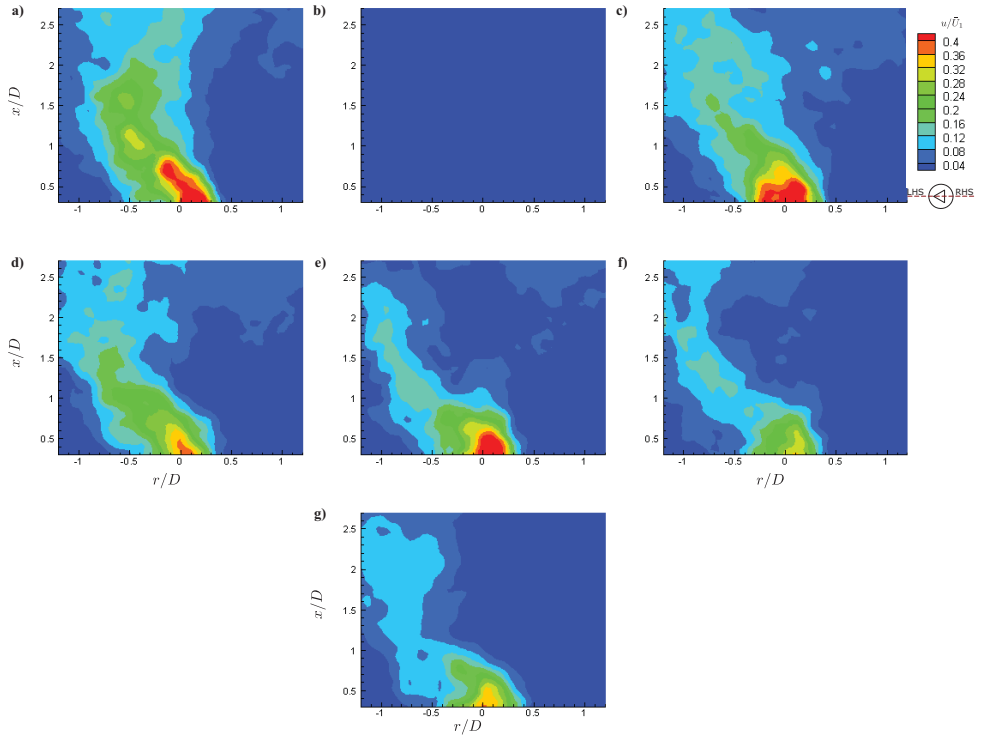

Figure A.7: Axial velocity component of the conditionally averaged flow fields, $u/\bar{U}_1$, with density ratio, ρ_j/ρ_a=1.0, for L/D= a) 2.21, b) 2.30, c) 2.40, d) 2.49, e) 2.58, f) 2.68 and g)2.77.

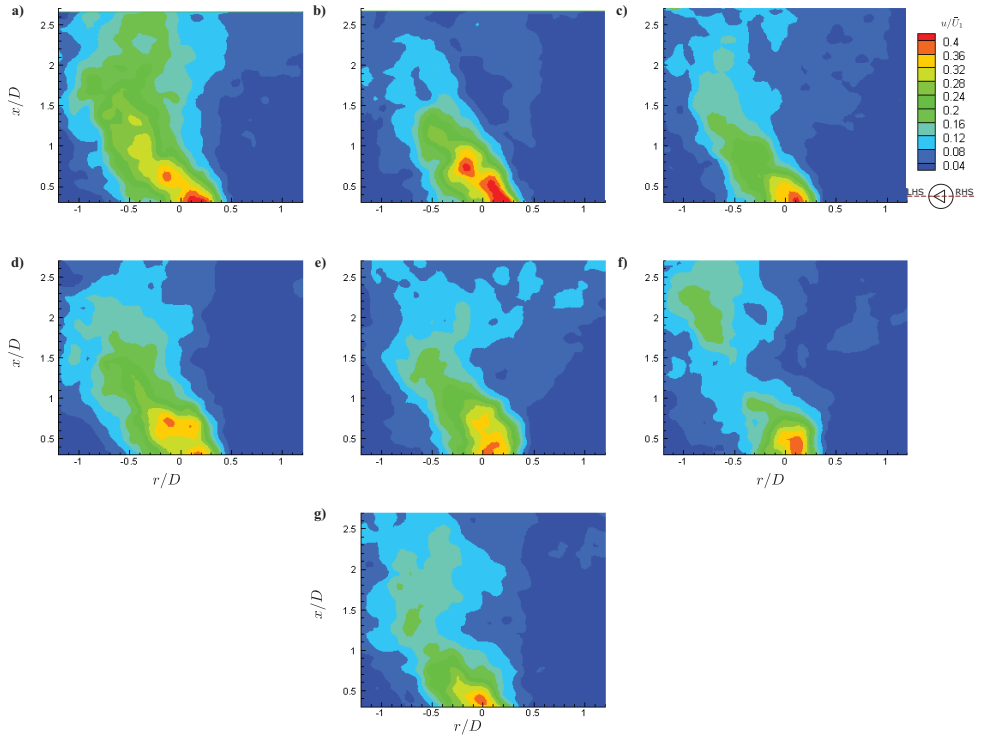

Figure A.8: Axial velocity component of the conditionally averaged flow fields, $u/\bar{U}_1$, with density ratio, ρ_j/ρ_a=2.24, for L/D= a) 2.30, b) 2.40, c) 2.49, d) 2.58, e) 2.68, f) 2.77 and g)2.87.

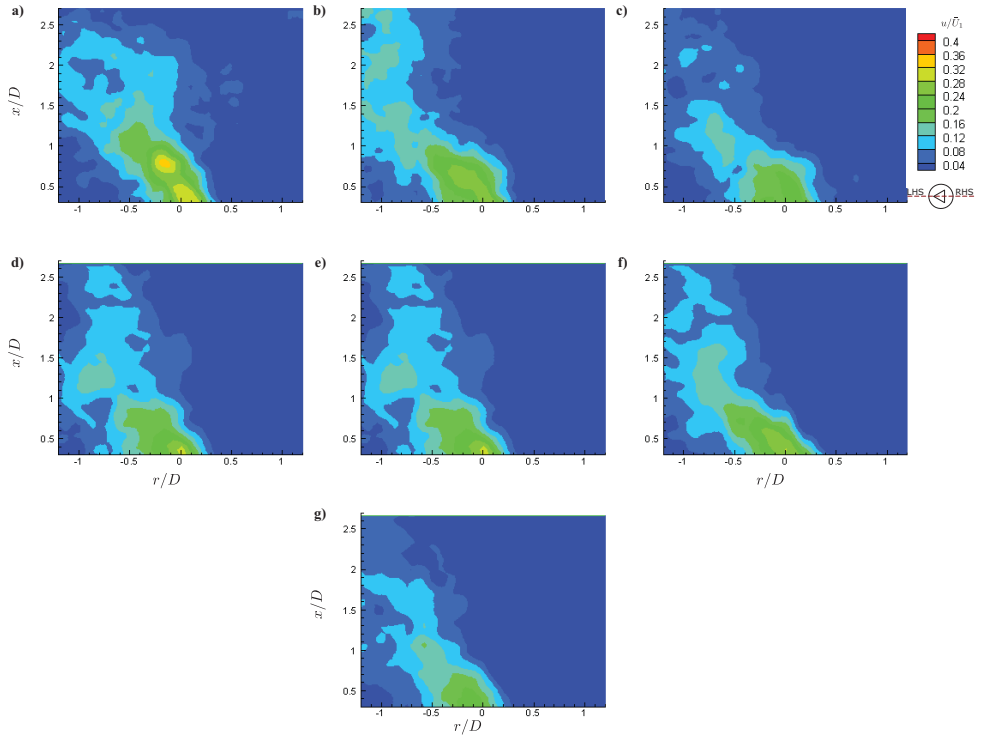

Figure A.9: Axial velocity component of the conditionally averaged flow fields, $u/\bar{U}_1$, with density ratio, ρ_j/ρ_a=5.0, for L/D= a) 2.40, b) 2.49, c) 2.58, d) 2.68, e) 2.77, f) 2.87 and g)2.96.

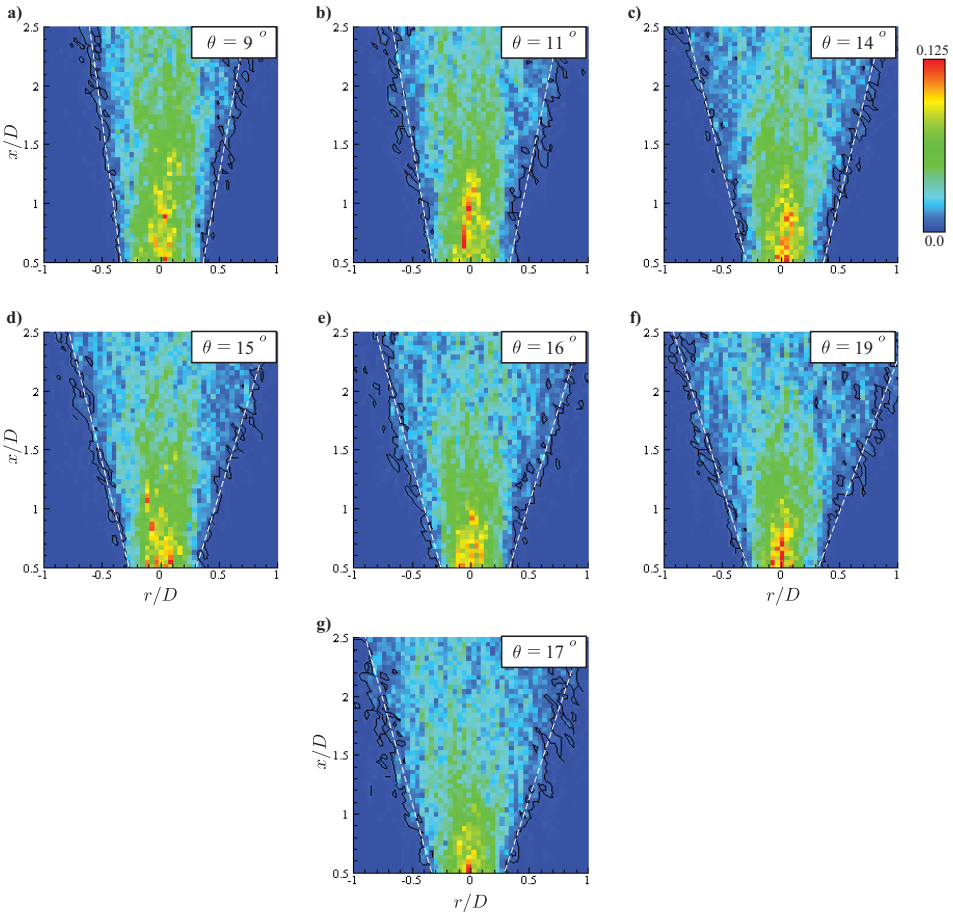

Figure A.10: Probability density of maximum velocity magnitude for $\rho_j/\rho_a = 0.45$ and $L/D =$ a) 2.11, b) 2.21, c) 2.30, d) 2.40, e) 2.49, f) 2.58 and g)2.68.

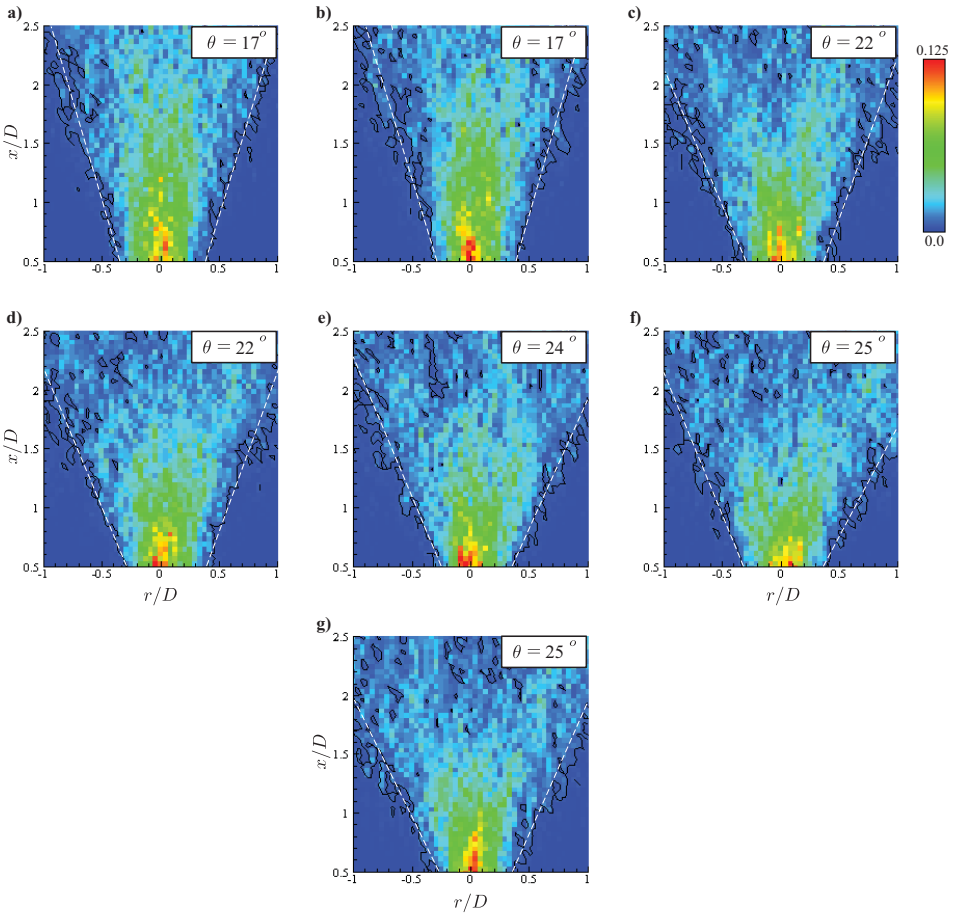

Figure A.11: Probability density of maximum velocity magnitude for $\rho_j/\rho_a = 2.24$ and $L/D =$ a) 2.30, b) 2.40, c) 2.49, d) 2.58, e) 2.68, f) 2.77 and g)2.87.

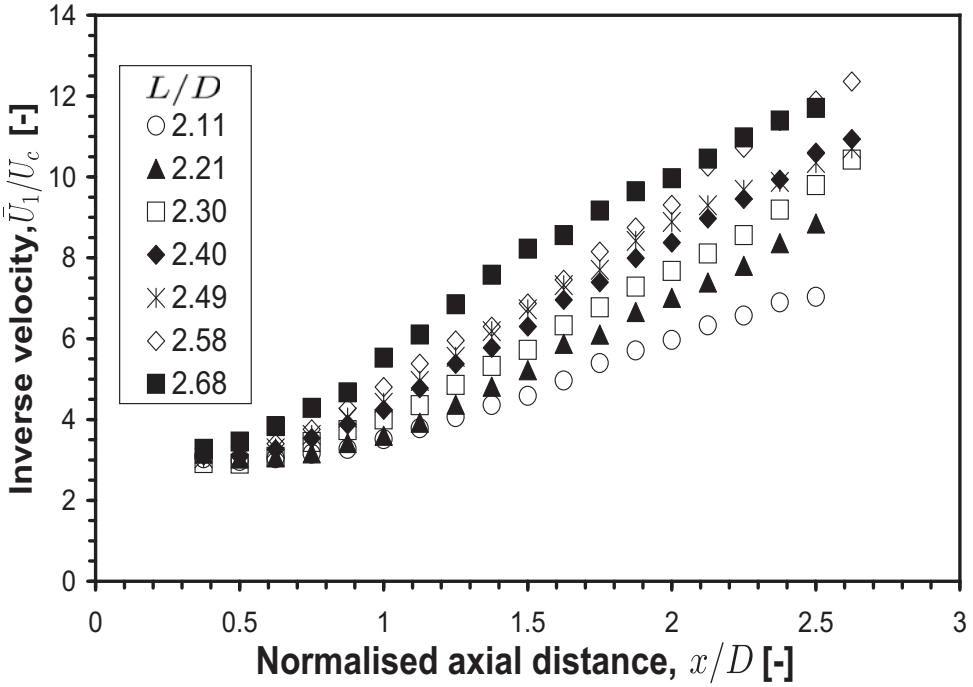

Figure A.12: Centreline inverse velocity for the TOJ nozzle at various L/D with ρ_j/ρ_a=0.45.

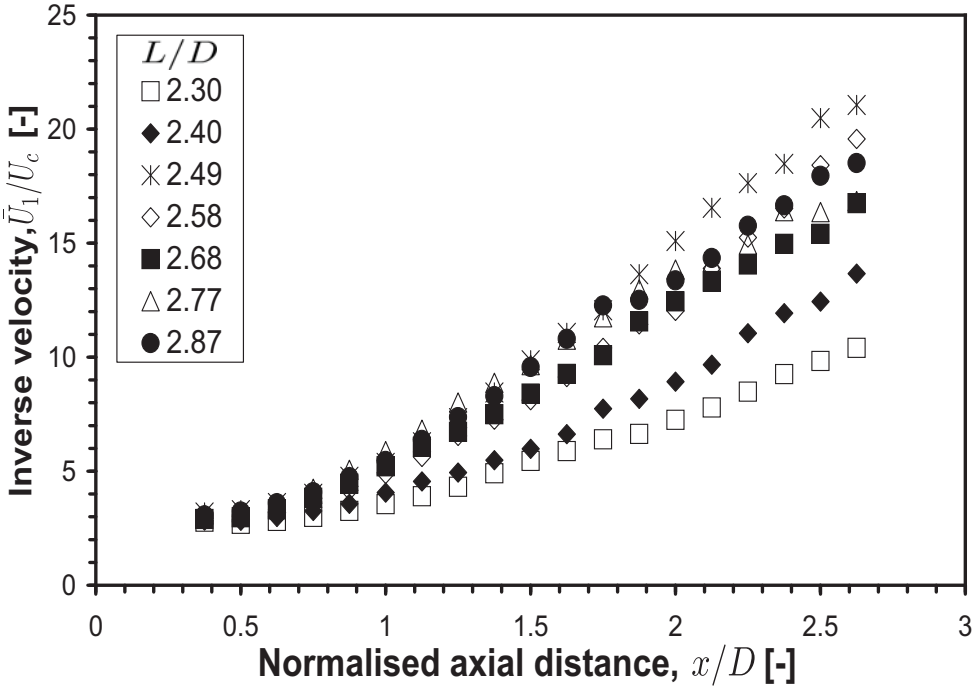

Figure A.13: Centreline inverse velocity for the TOJ nozzle at various L/D with ρ_j/ρ_a=2.24.

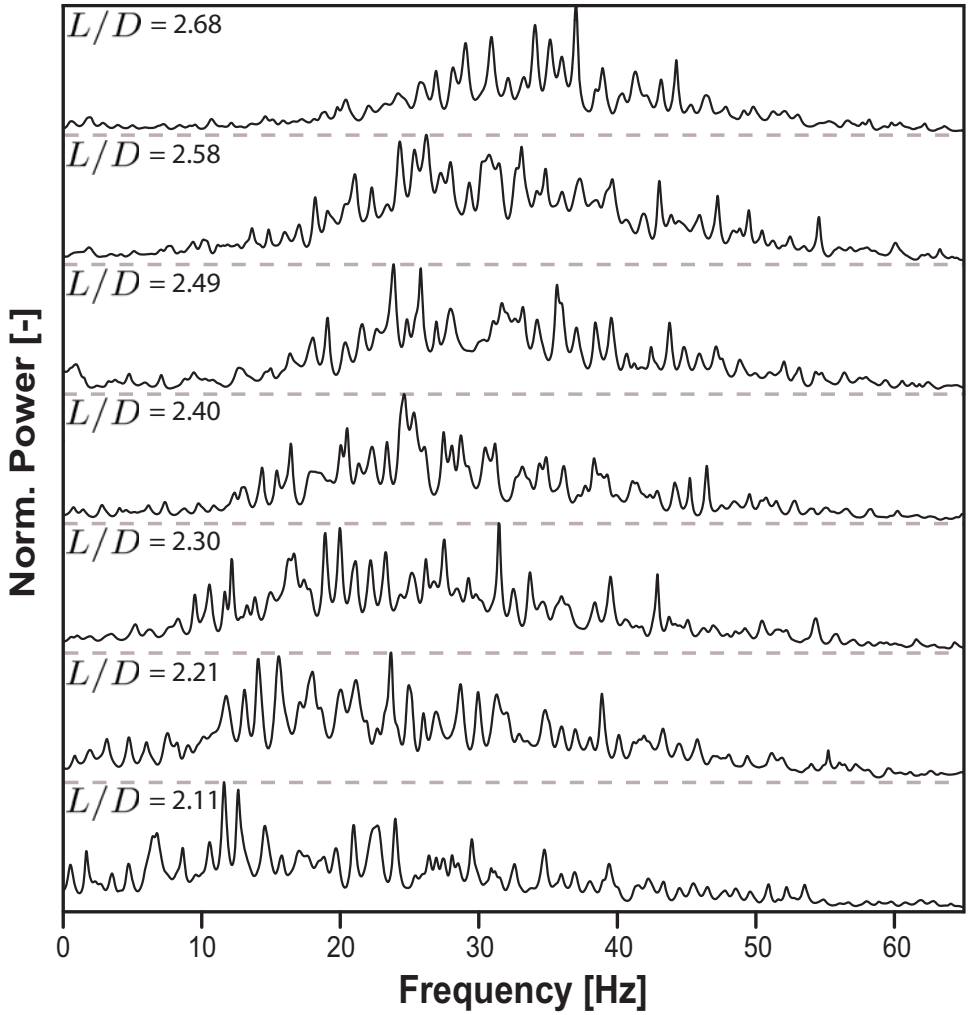

Figure A.14: Frequency power spectra for all L/D, with density ratio, ρ_j/ρ_a=0.45.

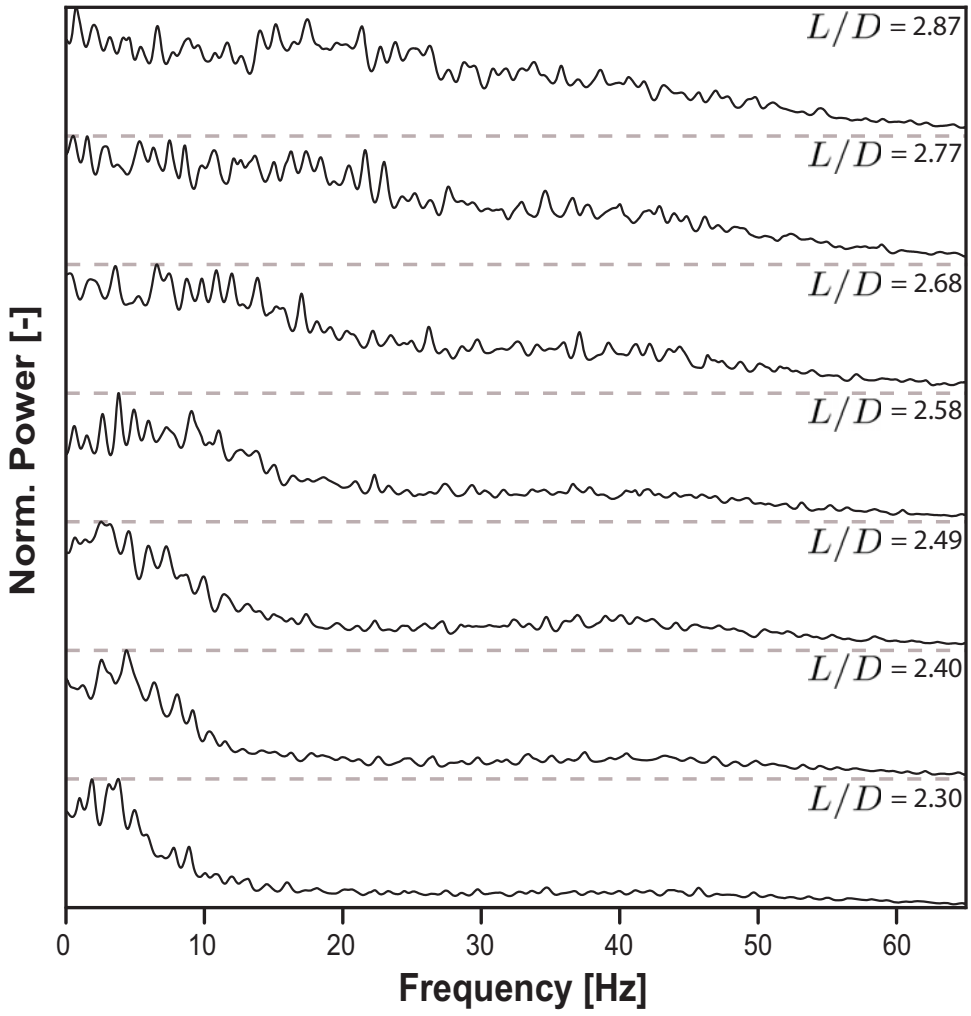

Figure A.15: Frequency power spectra for all L/D, with density ratio, ρ_j/ρ_a=2.24.

Appendix B

Variable Viscosity Data

This appendix shows data for the variable viscosity fixed density investigation on the TOJ nozzle flow.

Gas mixture	μ_j/μ_a	$\bar{U}_1$ [ms^{-1}]	Re [$\times 10^3$]
He 4.3% - CO_2 95.7%	0.82	27.23	26.6
CO_2 89.1% - Air 10.9%	0.83	27.23	26.3
SF_6 11.7% - Air 88.3%	0.98	27.23	22.3
SF_6 26.7% - He 73.3%	1.03	27.23	21.2

Table B.1: Operating conditions for variable viscosity TOJ with fixed density ratio, $\rho_j/\rho_a = 1.50$.

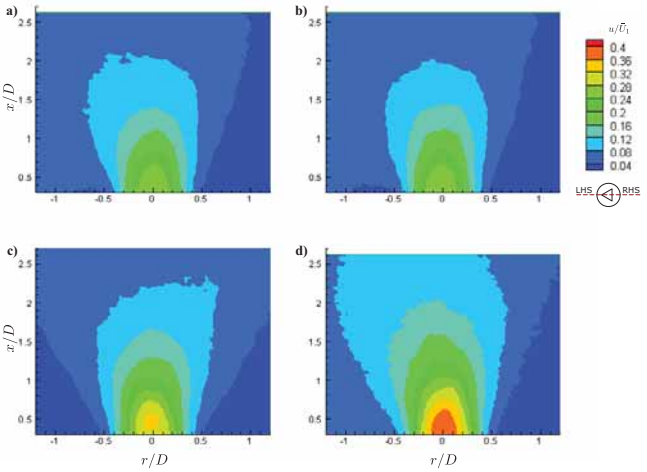

Figure B.1: Axial velocity component of the ensemble averaged flow fields, $u/\bar{U}_1$, for viscosity ratio μ_j/μ_a = a) 0.82, b) 0.83, c) 0.98 and d) 1.03.

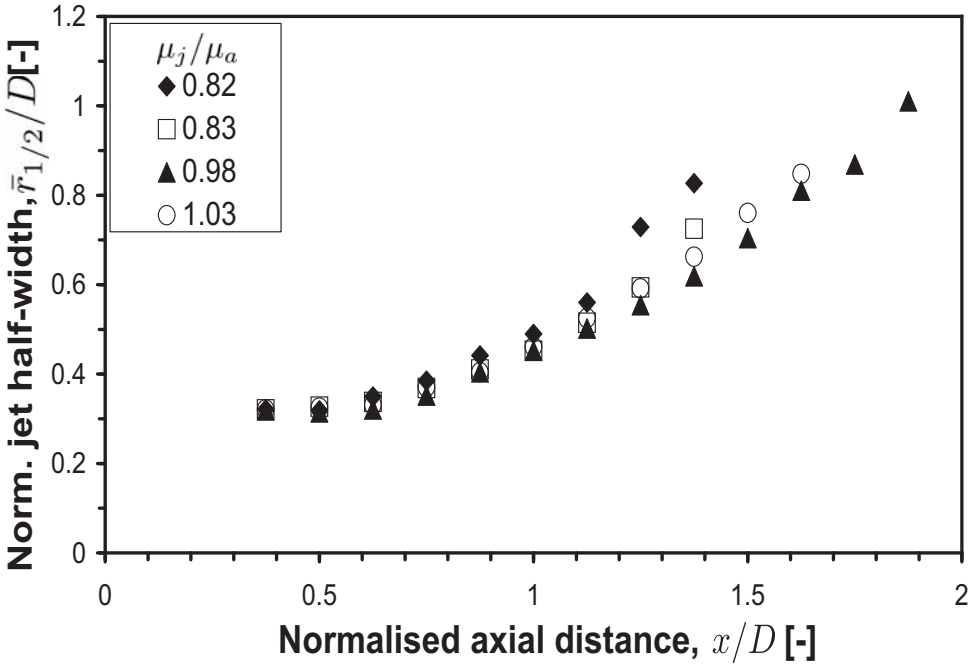

Figure B.2: Mean half widths for the TOJ nozzle at various μ_j/μ_a.

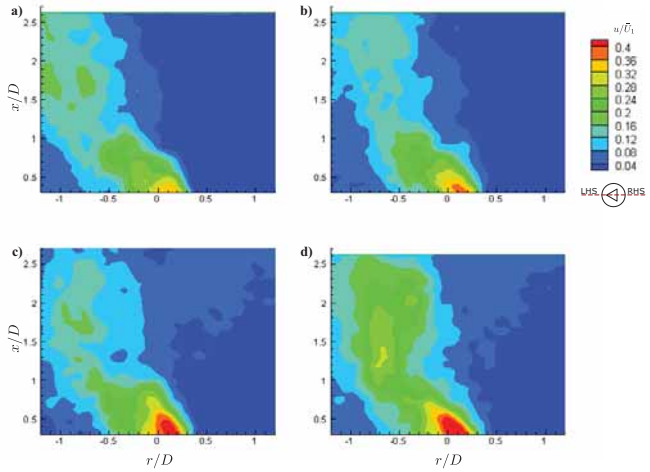

Figure B.3: Axial velocity component of the conditionally averaged flow fields, $u/\bar{U}_1$, for viscosity ratio μ_j/μ_a = a) 0.82, b) 0.83, c) 0.98 and d) 1.03.

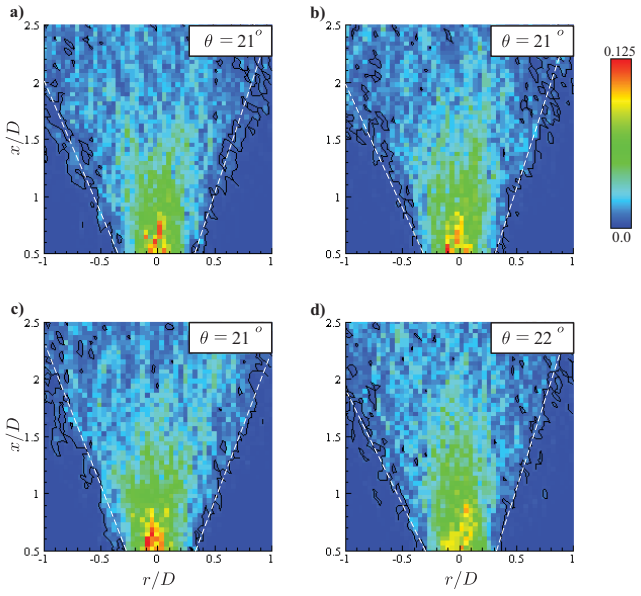

Figure B.4: Probability density of maximum velocity magnitude for viscosity ratios a) 0.82, b) 0.83, c) 0.98 and d) 1.03.

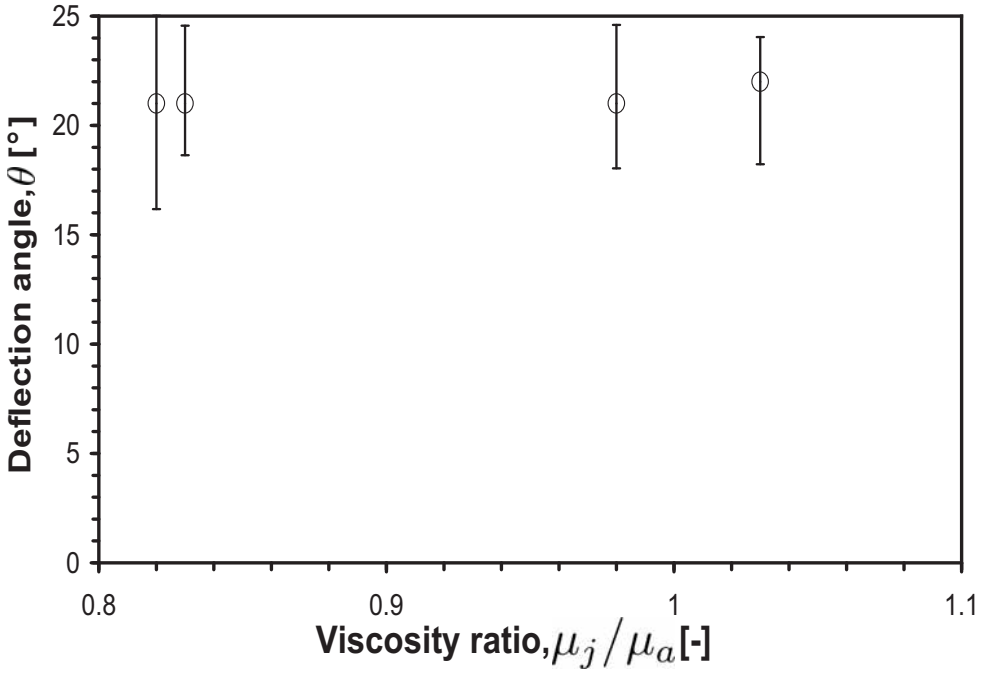

Figure B.5: Deflection angle, θ, of the instantaneous emerging jet as a function viscosity ratio, μ_j/μ_a.

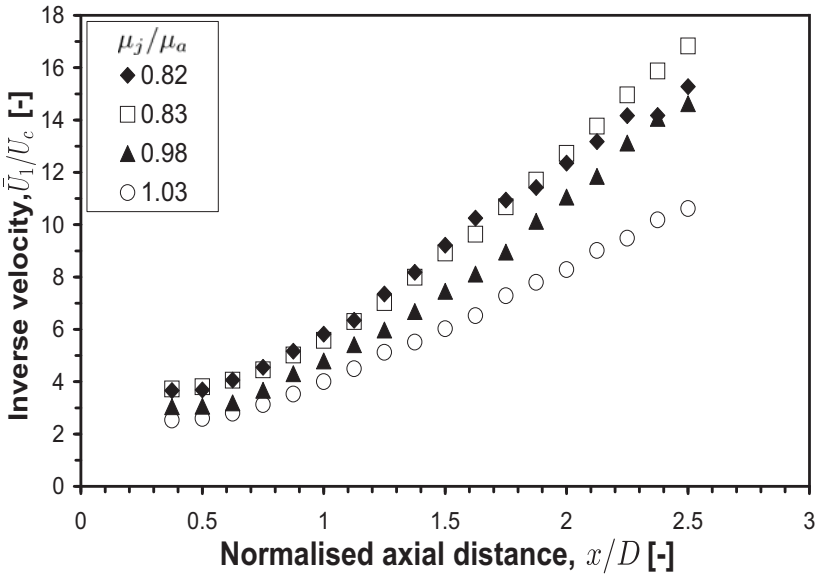

Figure B.6: a) Centreline inverse velocity,and b) centreline decay gradient at various viscosity ratios, μ_j/μ_a.

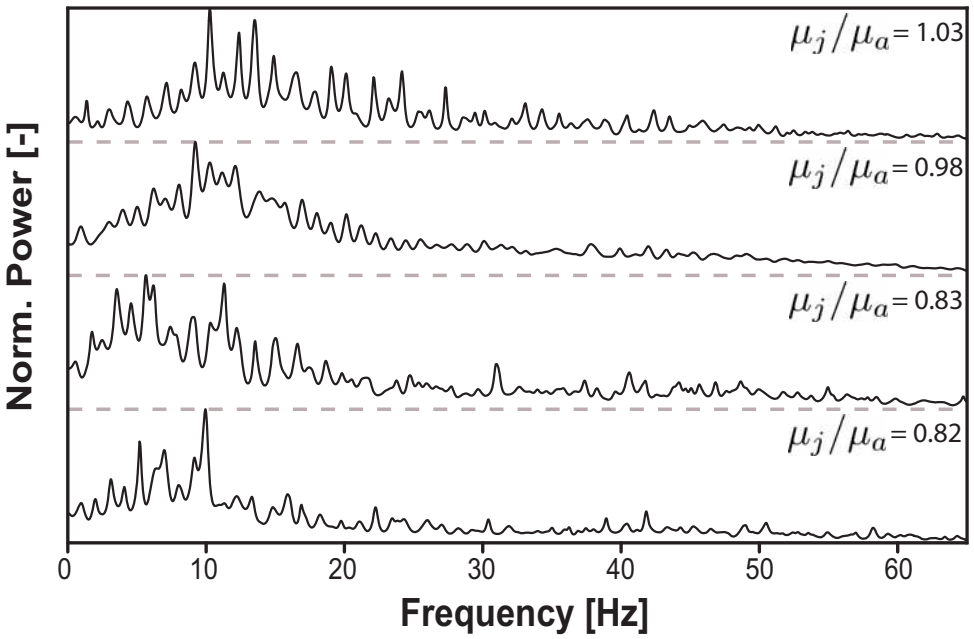

Figure B.7: Frequency power spectra for all viscosity ratios, μ_j/μ_a.

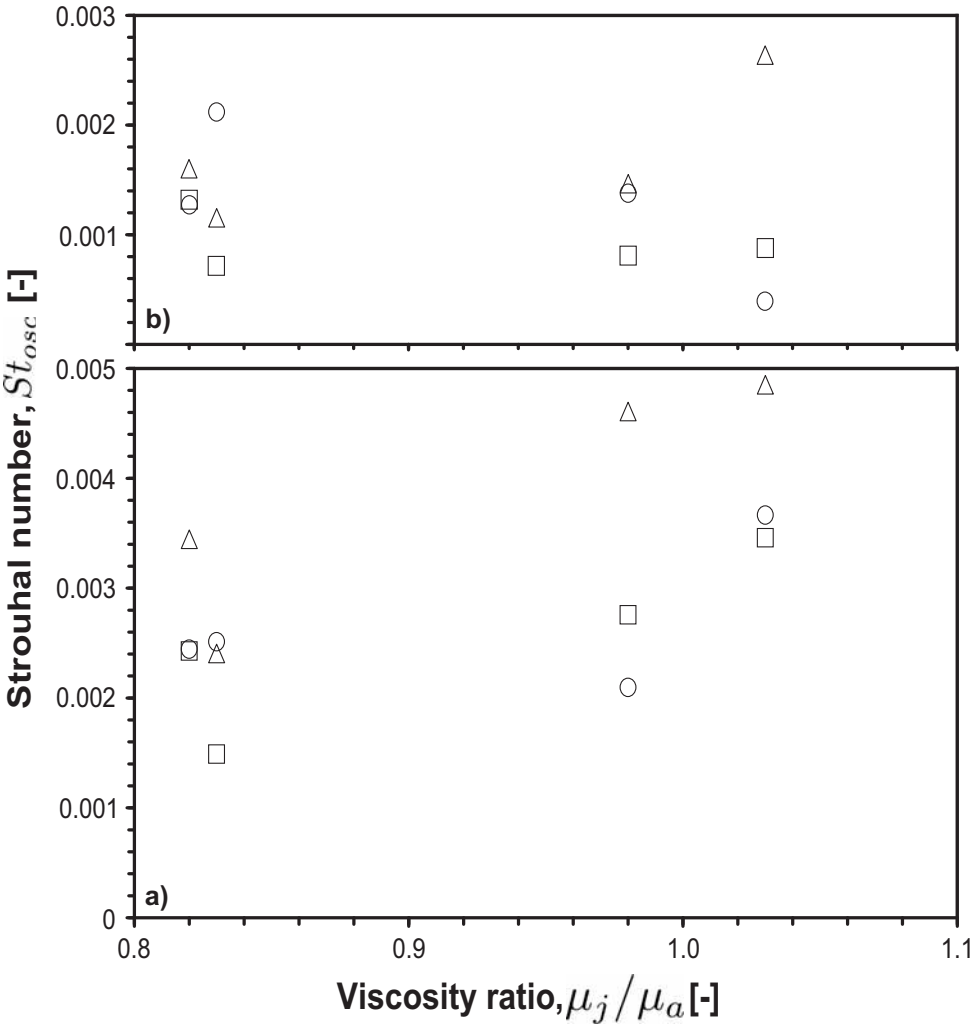

Figure B.8: a) Jet Strouhal number, St_{osc}, as a function of viscosity ratio, μ_j/μ_a, b) Measurement uncertainty. (Circles = FFT, Squares = Burg-MEM, Triangles = Peak counting)

Appendix C

Additional Combined Flow Figures

This appendix shows additional figures for the combined TOJ and co-annular nozzle flow.

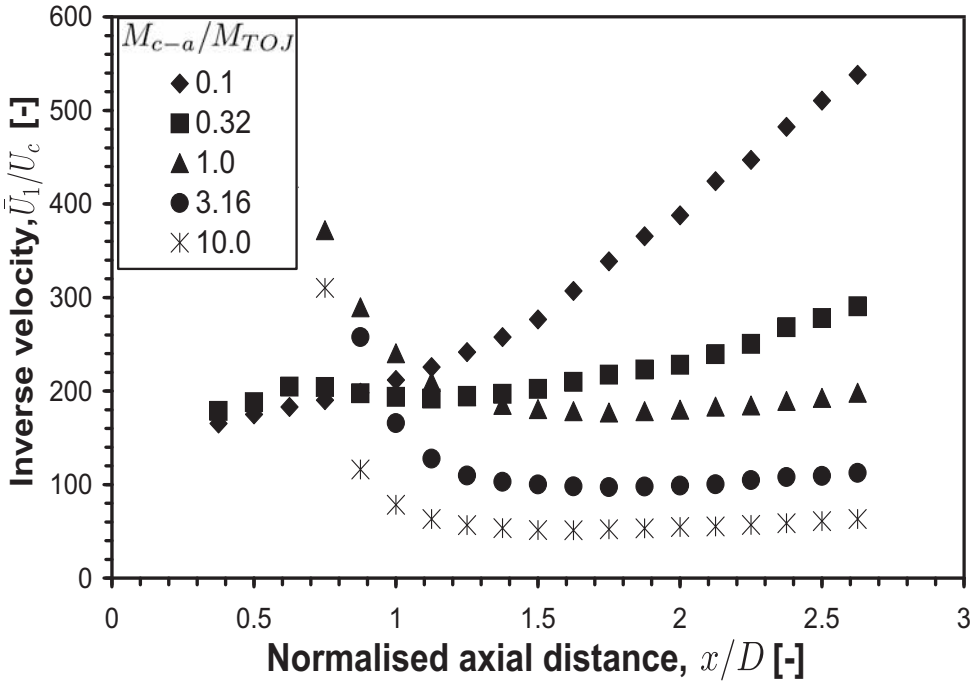

Figure C.1: Centreline inverse velocity for the combined nozzle at various momentum ratios, M_{c-a}/M_{TOJ}, and density ratio, ρ_j/ρ_a=0.45.

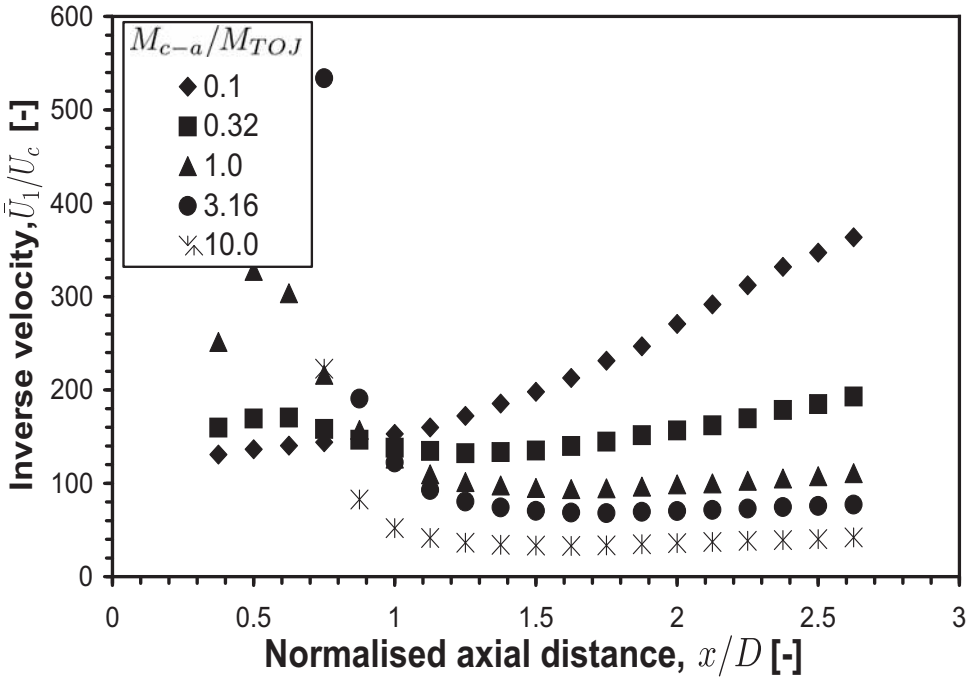

Figure C.2: Centreline inverse velocity for the combined nozzle at various momentum ratios, M_{c-a}/M_{TOJ}, and density ratio, ρ_j/ρ_a=1.0.

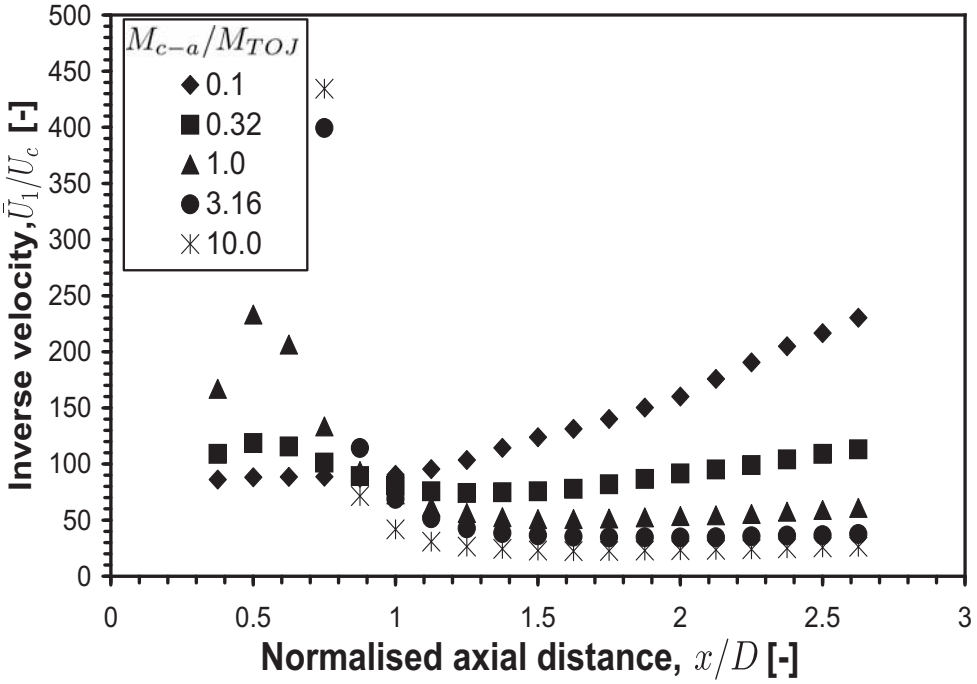

Figure C.3: Centreline inverse velocity for the combined nozzle at various momentum ratios, M_{c-a}/M_{TOJ}, and density ratio, ρ_j/ρ_a=2.24.

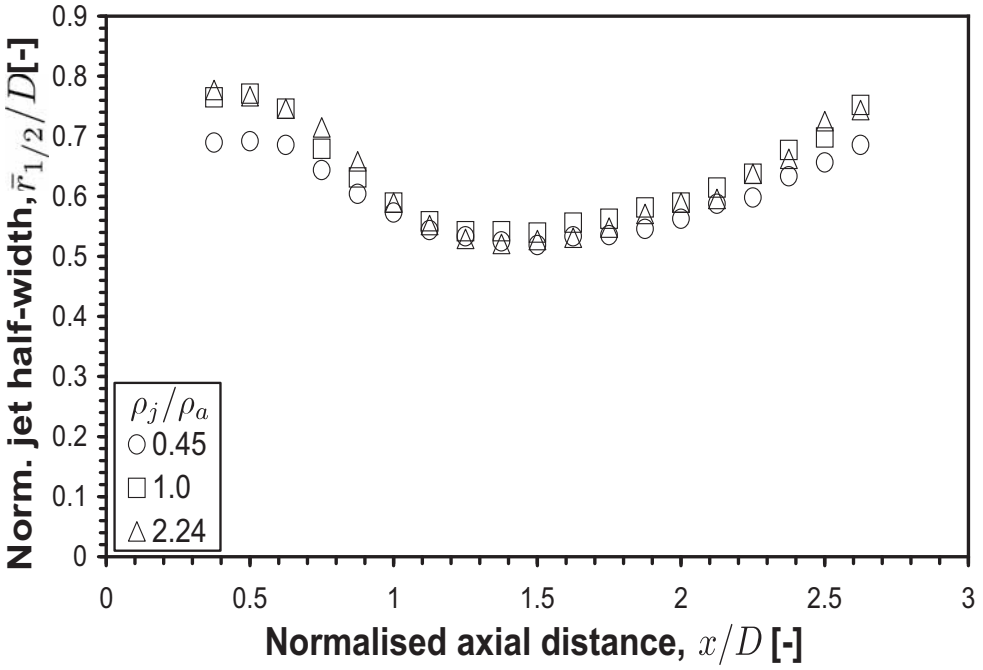

Figure C.4: Mean half widths for the combined nozzle at various density ratio, ρ_j/ρ_a, and momentum ratio, M_{c-a}/M_{TOJ}=0.32.

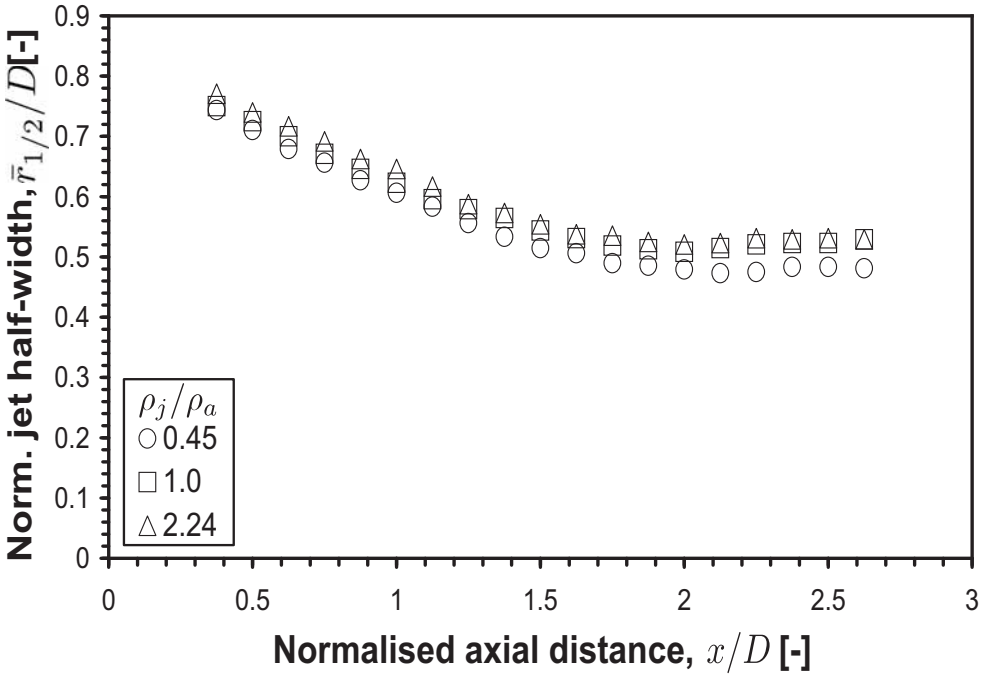

Figure C.5: Mean half widths for the combined nozzle at various density ratio, ρ_j/ρ_a, and momentum ratio, M_{c-a}/M_{TOJ}=3.16.

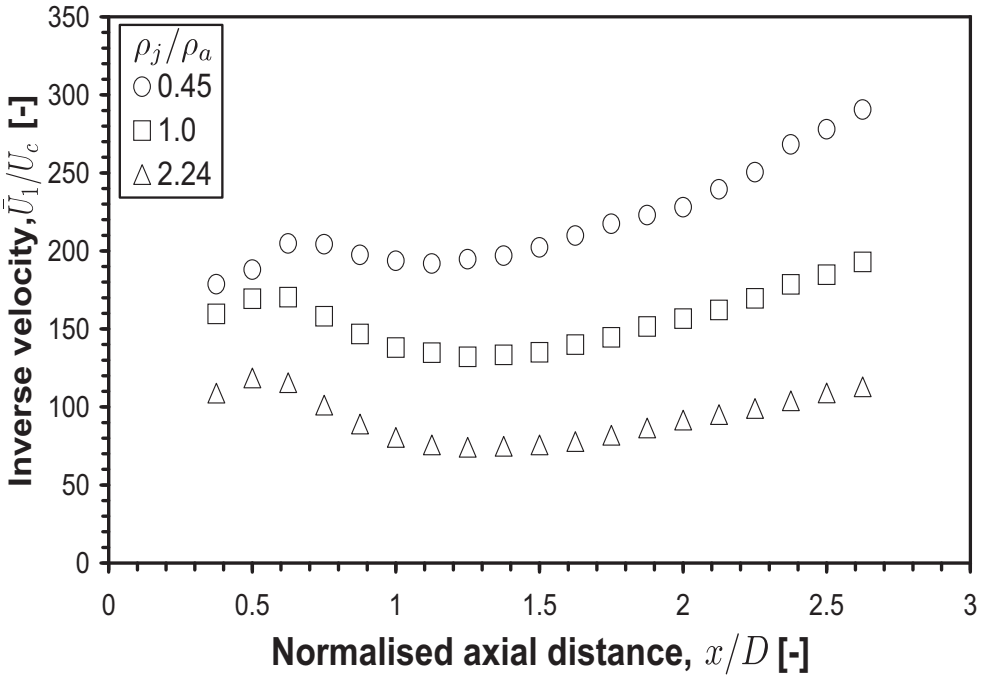

Figure C.6: Centreline inverse velocity for the combined nozzle at various density ratio, ρ_j/ρ_a, and momentum ratio, M_{c-a}/M_{TOJ}=0.32.

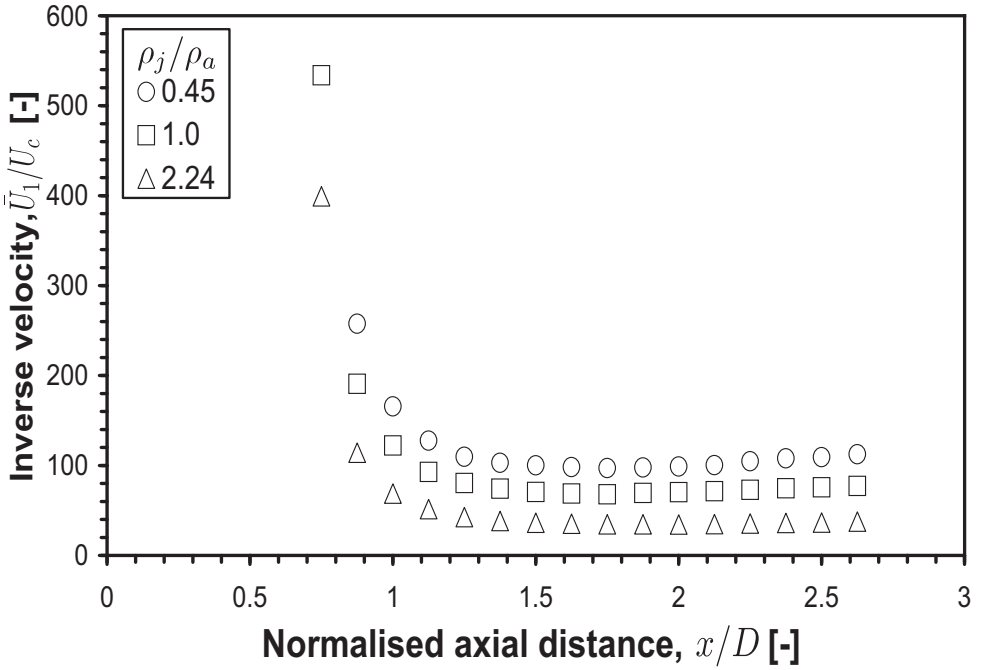

Figure C.7: Centreline inverse velocity for the combined nozzle at various density ratio, ρ_j/ρ_a, and momentum ratio, M_{c-a}/M_{TOJ}=3.16.

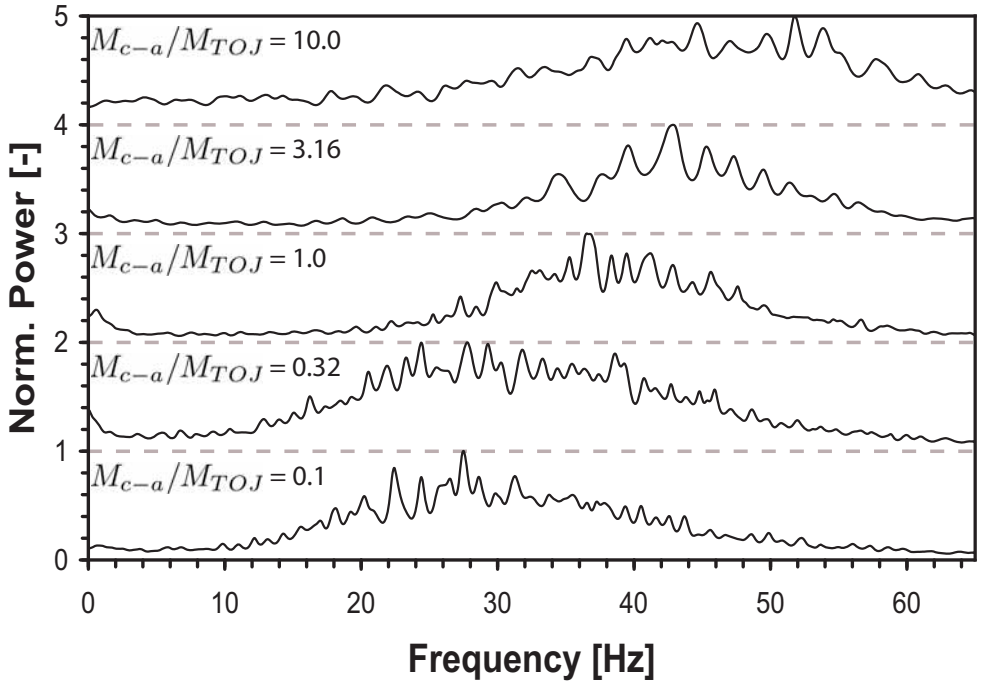

Figure C.8: Frequency power spectra for all momentum ratios, M_{c-a}/M_{TOJ}, with ρ_j/ρ_a=0.45.

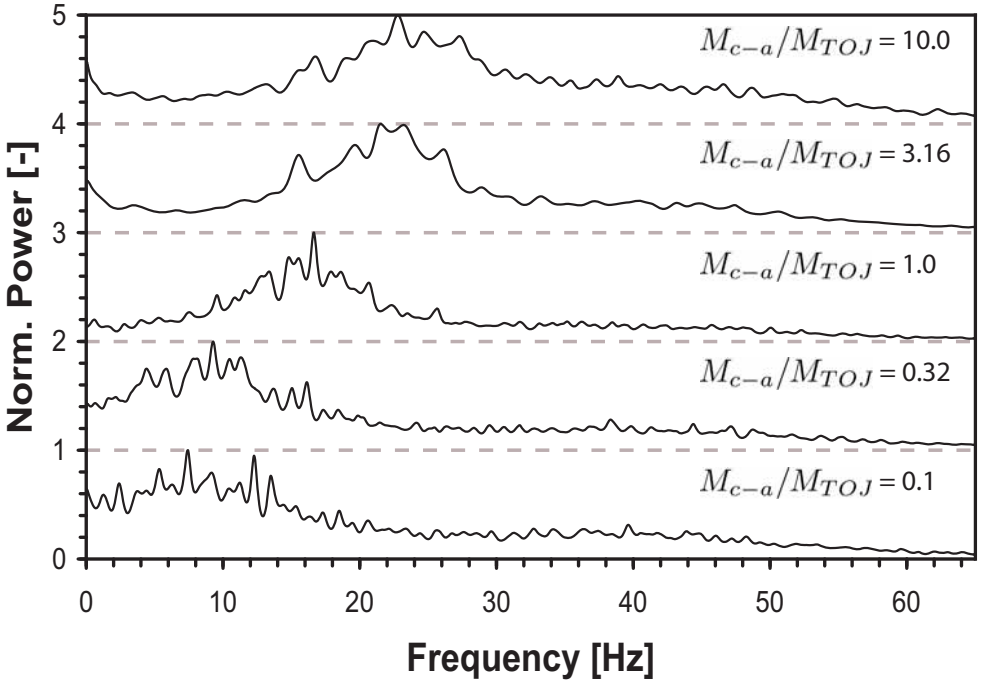

Figure C.9: Frequency power spectra for all momentum ratios, M_{c-a}/M_{TOJ}, with ρ_j/ρ_a=2.24.

Appendix D

Publications

This appendix lists publications arising from this thesis.

England, G., Kalt, P.A.M., Nathan, G.J. and Kelso, R.M. (2003), Near Field Measurements of Low Pressure Drop Oscillating Jet Burners, 'Australian Symposium on Combustion & The 8th Australian Flame Days Conference', Monash University, Australia.

England, G., Kalt, P.A.M., Nathan, G.J. and Kelso, R.M. (2004), The Effect of Density Ratio on the Mean Spread Rate of a Low Pressure Drop Oscillating Jet Nozzle, '15th Australasian Fluid Mechanics Conference', The University of Sydney, Australia.

England, G., Kalt, P.A.M., Nathan, G.J. and Kelso, R.M. (2009), The Effect of Density Ratio on the Near Field of a Naturally Occurring Oscillating Jet, *Experiments in Fluids*. Accepted 10th of June 2009.